2016

Underwater Explosion Energy Dissipation Near Waterborne Infrastructure

Paul R. Smith
University of Kentucky, paul.smith@uky.edu
Digital Object Identifier: http://dx.doi.org/10.13023/ETD.2016.023

STUDENT AGREEMENT:

I represent that my thesis or dissertation and abstract are my original work. Proper attribution has been given to all outside sources. I understand that I am solely responsible for obtaining any needed copyright permissions. I have obtained needed written permission statement(s) from the owner(s) of each third-party copyrighted matter to be included in my work, allowing electronic distribution (if such use is not permitted by the fair use doctrine) which will be submitted to UKnowledge as Additional File.

I hereby grant to The University of Kentucky and its agents the irrevocable, non-exclusive, and royalty-free license to archive and make accessible my work in whole or in part in all forms of media, now or hereafter known. I agree that the document mentioned above may be made available immediately for worldwide access unless an embargo applies.

I retain all other ownership rights to the copyright of my work. I also retain the right to use in future works (such as articles or books) all or part of my work. I understand that I am free to register the copyright to my work.

REVIEW, APPROVAL AND ACCEPTANCE

The document mentioned above has been reviewed and accepted by the student's advisor, on behalf of the advisory committee, and by the Director of Graduate Studies (DGS), on behalf of the program; we verify that this is the final, approved version of the student's thesis including all changes required by the advisory committee. The undersigned agree to abide by the statements above.

Paul R. Smith, Student

Dr. L. Sebastian Bryson, Major Professor

Dr. Yi-Tin Wang, Director of Graduate Studies

UNDERWATER EXPLOSION ENERGY DISSIPATION NEAR WATERBORNE INFRASTRUCTURE

THESIS

A thesis submitted in partial fulfillment of the
requirements for the degree of Master of Science in
Civil Engineering in the College of Engineering at the
University of Kentucky

By

Paul Raymond Smith

Lexington, Kentucky

Director: Dr. L. Sebastian Bryson, Professor of Civil Engineering

Lexington, Kentucky

2016

ABSTRACT OF THESIS

UNDERWATER EXPLOSION ENERGY DISSIPATION NEAR WATERBORNE INFRASTRUCTURE

Underwater explosions pose a significant threat to waterborne infrastructure though destructive pressure waves that can travel significant distances through the water. However, the use of bubble screens can attenuate the peak pressure and energy flux created by explosions to safe levels. This study investigates the prediction of pressure wave characteristics based on accumulated data, the damage potential of underwater explosions based on applied loads and effective material strength, and the bubble screen parameters required to prevent damage. The results were compiled to form a procedure for the design and implementation of a bubble screen the protection of waterborne infrastructure.

KEYWORDS: Bubble Screen, Shock Wave, Underwater Explosion, Attenuation, Infrastructure

Paul Raymond Smith

February 8, 2016

UNDERWATER EXPLOSION ENERGY DISSIPATION NEAR WATERBORNE INFRASTRUCTURE

By

Paul Raymond Smith

L. Sebastian Bryson, Ph.D., P.E.
Director of Thesis

Yi-Tin Wang, Ph.D.
Director of Graduate Studies

February 8, 2016

Dedication

I dedicate this thesis to my friend Jesus Christ, who freely gave me more than I could ever ask for.

ACKNOWLEDGEMENTS

First of all, I would like to thank my parents, Ray and Stephanie, for their unending support and encouragement in each of my endeavors, most recently in this work. They seemed to always know whether I needed a push, a listening ear, or moral encouragement. More specifically I would like to thank my dad for the countless hours of counsel, encouragement, and revision he gave as a father, a friend, and a professor.

I would like to thank the faculty and staff in the Civil Engineering Department at the University of Kentucky for making themselves available to answer my many questions and for encouraging an atmosphere of learning and innovation. I would like to thank Sheila Williams for all of her help in the office and for being a friend.

I would like to thank my advisor, Dr. Sebastian Bryson, for bringing me into his program and seeing me through to the end. Over the past few seasons of my life he has filled the roles of teacher, advisor, advocate, and encourager with excellence. He has endured my enthusiasm, rabbit trails, and disillusionment with grace and patience. He stands as one of the great men who has influenced my life and will always be one of my heroes. I would also like to thank the other members of my committee, Dr. Michael Kalinski and Dr. Braden Lusk, for their willingness to advise and vet my work.

TABLE OF CONTENTS

LIST OF TABLES

LIST OF FIGURES

1 Introduction

1.1 Synopsis of the Problem

A major concern with waterborne infrastructure is the devastating vulnerability to underwater explosions, which can be significantly more destructive than those caused by similar explosives out of water. Detonated explosives produce significant blast pressures which propagate outward, initially as a shockwave and then as pressure waves. Within a certain distance these pressures may be large enough to cause significant damage to the structures, and ultimately human lives. The standoff distance is the distance between the charge and the structure, though sometimes called radial standoff distance when the direction is not strictly horizontal. Increasing the radial standoff distance is one of the primary methods currently used to protect waterborne infrastructure. However, the use of bubble screens to attenuate, or reduce, potentially damaging pressures to structures, is still uncommon even though it is known to be effective.

Bubble screens are created by pumping air through a submerged manifold that has thousands of small orifices to disperse a large, roughly uniform, screen of air bubbles into the water. The introduction of air bubbles into the water creates an approximately homogenous mixture that possesses a much higher compressibility than the water. The high compressibility of the mixture attenuates the pressure wave by two mechanisms. First, the mixture has a much lower acoustic velocity, or speed of sound, than the water, this creates a different acoustic impedance that reflects a portion of the pressure wave back into the water. Second, as the remaining pressure wave enters the bubble screen, the individual bubbles absorb some of the energy and dissipate it as heat and reradiated waves into the water. The amplitude of the wave that passes through the bubble screen has been shown to be attenuated to less than 10 percent of the original amplitude. In many situations, it may not be possible or practical to increase the standoff distance to a range that adequately reduces pressure waves through natural decay. Therefore, implementing a bubble screen will serve to both reduced the required standoff distance and protect the waterborne infrastructure. However, since the use of bubble screens largely remains unadopted, there are no comprehensive design procedures to direct the implementation on a wide scale.

The purpose of this study is to develop a procedure to optimize the design of bubble screens based on underwater explosion characteristics, the response of structural materials to blast pressures, and the attenuation properties of bubble screens.

1.2 Proposed Concepts

The general concept of this research was to determine both the damage potential underwater explosions pose to waterborne structures, and also the necessary characteristics a bubble screen should possess to adequately prevent or limit damage. It was also necessary to investigate measured underwater blast data and prevailing equations that predict blast characteristics in order to develop appropriate predictions for bubble screen design.

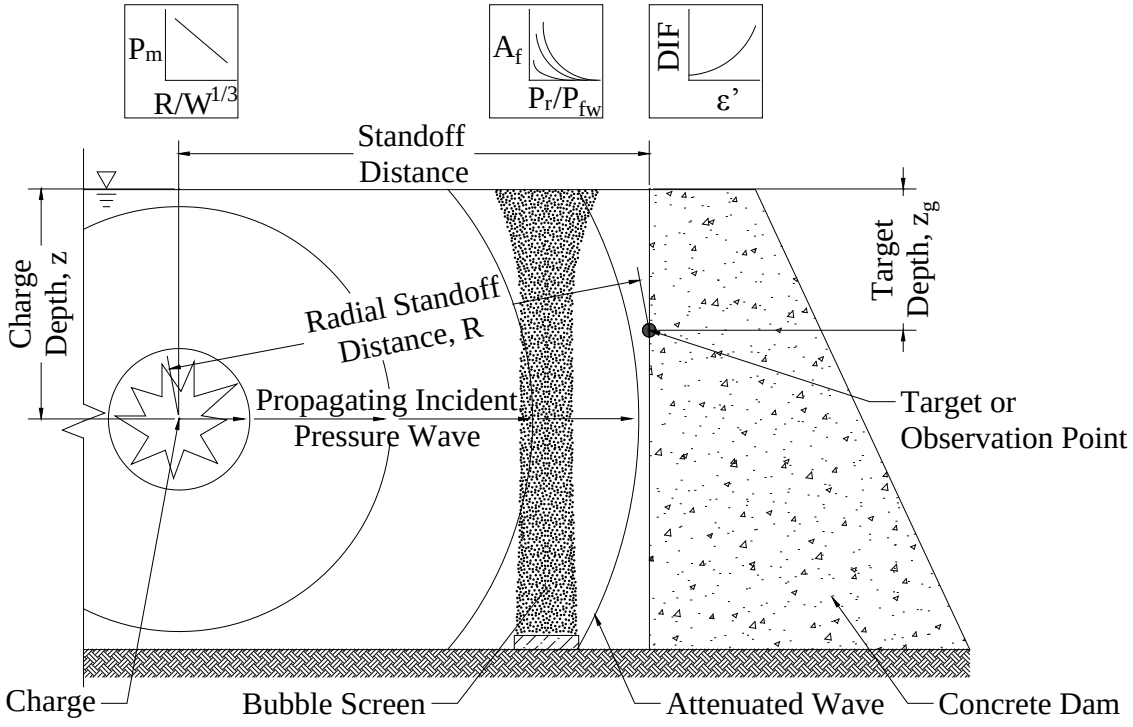

Figure 1.1 Schematic of General Scenario and Proposed Concepts

Pressure wave induced peak pressure and energy flux models were created by plotting underwater explosion pressure wave data versus the radial standoff distance from the charge, see Figure 1.1. The data acquired was measured in studies using trinitrotoluene (TNT), which produces models that can be readily modified for other high explosives. These plots were used to develop empirical equations that represented the measured data

used in this analysis. Plotting measured peak pressure versus the respective charge depth from each experiment allowed consideration of the effect of charge depth on peak pressure. This plot revealed differentiation with depth, which allowed the development of a depth coefficient to add to the peak pressure equation. Predicting damage potential occurred by setting the peak pressure equal to the dynamic strength concrete, and by applying the dynamic strength of structural steel to static loading and strain energy equations. The dynamic strengths of materials were calculated using dynamic increase factors (DIFs) presented in UFC 3-340-02 (2008). Development of additional plots determined the minimum allowable radial standoff distance to prevent damage versus charge weight. The maximum allowable peak pressure and energy flux determined from these plots established the required bubble screen attenuation. Bubble screen attenuation rates compared to airflow and depth parameters determined the necessary design of the bubble screen. Finally, these parameters led to the creation of a procedure to determine the required bubble screen characteristics necessary to reduce peak pressure and energy flux to allowable levels for a given radial standoff distance and charge weight. The intent of the study was to determine what additional attenuation from a bubble screen is required to protect the structure for a given radial standoff distance.

1.3 Objectives of the Research

The primary objective of this research was to determine the required properties of a bubble screen to attenuate underwater blast pressures to levels that will not cause damage to waterborne infrastructure. The destructive potential of underwater explosions is generally understood, however there is an absence of literature which combines the predicted loads, the structural response to pressure waves, and a design to mitigate the destructive waves. This research attempted to refine the current method of predicting peak pressure and energy flux produced by underwater pressure waves. A discussion and recommendation was made to determine the allowable peak pressure and energy flux for various material types and strengths. The operation of bubble screens was investigated to determine the parameters that most significantly impact performance and the performance required to attenuate pressure waves to safe levels. The research considered radial standoff distance and bubble

screen parameters to be the variables which may be controlled to prevent or limit damage to waterborne structures.

Individual elements of this research conducted toward the primary objective included:

- Comparing pressure versus radial standoff distance at various charge weights and depths.
- Comparing energy flux versus radial standoff distance at various charge weights and depths.
- Determining the dynamic strengths of common construction materials.
- Using peak pressure and energy flux to determine the critical radial standoff distances that potentially could cause damage to waterborne structures.
- Determining the attenuation performance of bubble screens for various parameters, specifically focusing on airflow.
- Creating a design procedure that utilized the results of the preceding research to determine the expected pressure wave characteristics, damage potential, and required bubble screen design to prevent damage.

1.4 Relevance of the Research

The protection of waterborne infrastructure is significant to modern civilization as disruption or failure of these services often affects a widespread population. This research was conducted with the potential of terrorist attacks as the primary concern, though the application of the results are more widely applicable. Bubble screens are commonly used to attenuate the acoustic pressure waves due to construction activities and military training, specifically to protect aquatic wildlife that are particularly sensitive to disturbances in the water. Bubble screens have also been used to protect waterborne structures and watercraft, though not regularly. Two of the difficulties facilitating protection of infrastructure are the multitude of potential targets, and the unpredictable timing and nature of an intentional attack. Therefore, the use of a passive mitigation technique, such as bubble screens, may be favorable over a more active approach. The specific criteria relating to damage potential

include peak pressure, energy flux, radial standoff distance, material strength, and structural response. The accurate presentation of the potential threat caused by underwater explosions to waterborne infrastructure and of the necessary parameters of a bubble screen to mitigate this threat, may increase the acceptance of such measures of protection. For example, using the material strength of a structure to determine the maximum allowable peak pressure that will not cause damage, with a prediction of the incident peak pressure, allows the design of a bubble screen to achieve adequate attenuation to reduce the incident peak pressure to the allowable level.

There is minimal unclassified research pertaining to the protection of waterborne structures by use of a bubble screen. Furthermore, there is a sufficient lack of design aids that include provisions concerning the characteristics of pressure waves, the damage potential of structures, and the attenuation of damaging pressure wave characteristics in a single document. Thus, this research investigated the use of bubble screens for structural protection, and compiled the pertinent details into a concise design procedure.

1.5 Content of the Thesis

Chapter 2 presents a technical review of underwater blast mechanics, characteristics of underwater pressure waves, the damage potential of underwater explosions on structures, and the implementation and performance of bubble screens, including case studies.

Chapter 3 provides a in depth discussion of the analysis conducted including: the optimization of similitude equations for the data acquired, the damage potential underwater pressure waves pose to structures, and the parameters governing the performance of bubble screens.

Chapter 4 includes two bubble screen design procedures. One to determine the bubble screen parameters required given a predetermined scenario, and another to determine the expected performance for an existing bubble screen manifold.

Chapter 5 summarizes the work and presents the conclusion. The results from the analysis are also presented.

2 Technical Review

The following technical review was conducted to establish the necessary background and theory required to design a bubble screen for the protection of waterborne infrastructure from underwater explosions. This review includes: 1) underwater explosion mechanisms, 2) the general characteristics of pressure waves, 3) the damage potential of pressure waves to structures, and 4) the implementation and performance of bubble screens.

2.1 Underwater Explosion Mechanics

Underwater explosions are the result of the detonation of an explosive at some distance below the surface of the water, see Figure 2.1. The water immediately surrounding the explosion is a compressible fluid that lacks sufficient tensile capacity to resist the extreme pressures created by the explosion and moves outward. Thus, the response of the system possesses similarities to out-of-water explosions, but has unique characteristics as a result of the much greater density of water compared to air.

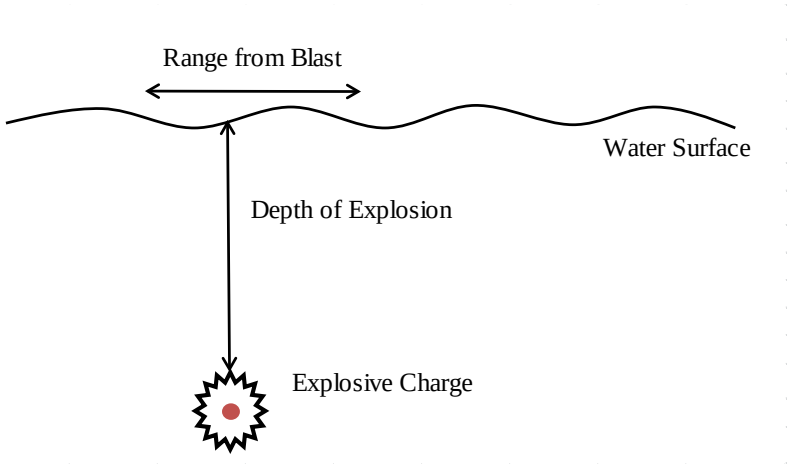

Figure 2.1 Underwater explosion characteristics

During the explosion process the initial mass of the explosive transforms into a very hot mass of gas at exceptionally high pressures. When this occurs underwater, the resulting effect to the surrounding water is determined within the field of hydrodynamics. By considering water a homogeneous fluid that is unable to support shear stresses, the water subjected to the explosion is capable of re-adjusting via flow to the imposed displacements of the water-explosive boundary (Cole 1948).

Water is a compressible fluid, and as such, any localized pressure applied to a region in the water transmits as a wave disturbance to other points in the water. The pressure wave will propagate with a large yet finite velocity, and the wave will involve local motion of the water and changes in pressure. If the local motion is one-dimensional, it will generate plane waves which travel without substantial change in shape or magnitude. However, if waves are radiated from the source in the characteristically spherical pattern, the amplitude decreases with distance from the source, and the motion of the water is affected by the pressure differences created from the spherical deviation, which is known as afterflow or surge (Cole 1948). Figure 2.2 depicts typical waves created by underwater explosions.

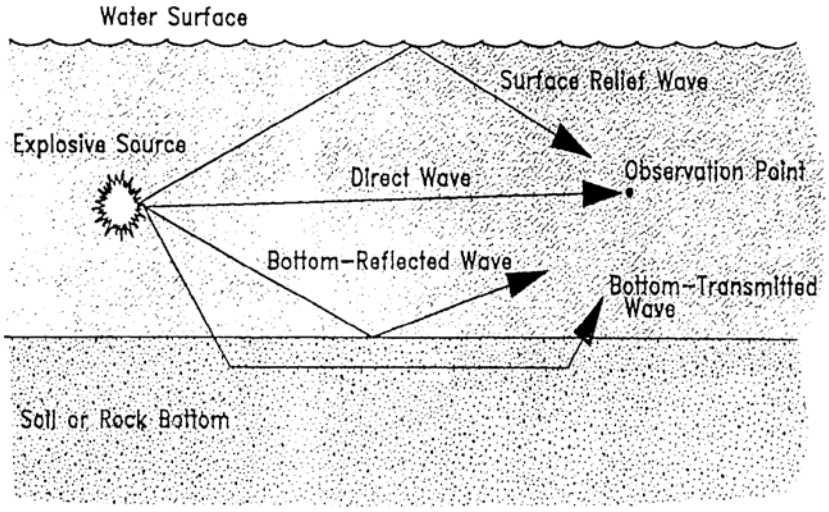

Figure 2.2 Schematic of waves created by underwater explosions (USACE 1991)

A detonation creates a shock wave by a rapid exothermic chemical reaction occurring immediately behind the shock front (Cooper 1996). This shock front is the result of the gaseous expansion that occurs as the solid explosive material transforms into a gas product. The speed at which this transformation takes place produces extremely large pressures that are transferred to the surrounding water nearly instantaneously and propagate radially, initially as a shock wave, that travels at speeds greater than the acoustic velocity of the water, and then as a compression p-wave, that travels at the acoustic velocity (Hempen 1993b). Figure 2.2 shows the four primary waves that propagate from the explosion. The Direct Wave follows the shortest path to the observation point, with only natural decay attenuating the amplitude of the wave. The Bottom Reflected Wave reflects off the bottom

boundary of the water, the reflected wave will partially attenuate depending on the density of the material. Denser materials will attenuate to a lesser degree. The Bottom Transmitted Wave is imparted by a bottom reflected wave, but travels through the substrate before returning to the water. The Surface Relief Wave is a rarefaction wave, or tension wave, that effectively eliminates the compression component of the Direct Wave or Bottom Reflected Wave when they intersect, this is known as surface cutoff. The Surface Relief Wave is due to the acoustic impedance introduced by the much more compressible air, which causes essentially all of the energy to propagate back into the water, though in tension instead of the initial compression wave. (USACE 1991).

Initially the gas bubble has a much greater pressure than the surrounding ambient hydrostatic pressure in the water, which is partially alleviated by the creation of a shock wave, and then fully by the outward flow of water (Cole 1948). Following the formation of the shockwave, the high pressures within the gas bubble cause the bubble to expand forcing the water outward, the inertial effect of the water movement causes the bubble to expand until the gas pressure is less than the hydrostatic pressure (Sulfredge et al. 2005). As a result, the water collapses on the bubble, recompressing the gas to a pressure greater than ambient, though less than the initial gas pressure. This begins a sequence of diminishing bubble oscillations in which the bubble expansion and contraction continues, decreasing in intensity with each oscillation, until the bubble reaches the water surface or are damped out by viscous fluid friction (Sulfredge et al. 2005). Figure 2.3 demonstrates the phenomenon related to the peak pressure and bubble oscillations (or pulses). The incident shock wave is shown to be much greater than the bubble pulse pressures, which diminish with each successive oscillation.

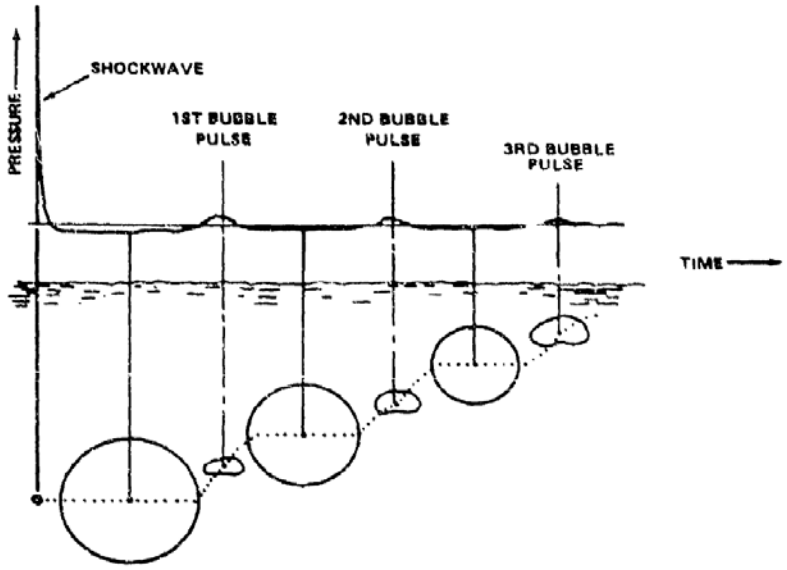

Figure 2.3 Pressure Waves and Bubble Phenomenon of Underwater Explosions (Swisdak 1978)

The bubble pulses continue to produce pressure waves in the water, but with significantly lower peak pressures than the initial explosion shock wave (Misovec 1976). The periods of the bubble pulse pressure waves are much longer than the incident pressure wave which may cause the overall impulse imparted to a structure to be comparable or even larger than that of the primary pressure wave. The pressure wave characteristics produced by the bubble pulses vary as functions of charge weight, range, and depth, just as those produced by initial shock wave (Sulfredge et al. 2005).

2.2 General Characteristics of Pressure Waves

Initially the wave propagated from an underwater explosion is a shock wave, which by definition travels at speeds greater than the acoustic velocity (speed of sound) of the water. However, the wave quickly transforms into a seismic p-wave that travels through the water at specifically the acoustic velocity (Hempen 1993a). While the common use of the term "shock wave" describes both waves, Hempen (1993a) uses "pressure wave" as a general term to describe the waves propagating from the explosion without regard to the distance from the source, or more specifically the velocity. This study uses the term "pressure wave."

Characteristic of the pressure wave is a steep-fronted compression wave that decays rapidly in an exponential fashion as it propagates through the medium (Cole 1948). Pressure waves produced underwater possess similar characteristics to those caused by in-air explosions; however the high compressibility of air rapidly attenuates the pressure wave, while the relative incompressibility of water negligibly attenuates the pressure wave. For this reason, water is considered incompressible when considering the effects of underwater pressure waves (Cole 1948).

Rude and Lee (2007) present a sample pressure wave trace from an underwater explosion that depicts the key features of a pressure wave, see Figure 2.4. The arrival of the pressure wave is characterized by a near-instantaneous rise in pressure to a sharp peak (peak pressure), which is immediately followed by an exponential decay in pressure, gradually deviating from the exponential form. The peak pressure and subsequent decay occurs over a period of a few milliseconds. Following the peak pressure wave, a secondary pressure wave peak is shown that was created by the bottom reflected wave as indicated in the figure. Immediately following is the "Surface Cutoff," or reflection of the wave from the water surface. Since the surface cutoff wave is a tension wave it effectively eliminates the bottom reflected wave and any remaining pressure from the incident pressure wave that were compression waves. Following the surface cutoff, the ambient pressure of the water is just above the vapor pressure of water, placing the water in a state of cavitation (liquid-free zones or bubbles). The water will remain in this state until the water is returns to ambient hydrostatic pressure. Rude and Lee (2007) note that the bottom reflection and surface cutoff are nearly coincident because the charge and gauge were located at mid-depth, and would otherwise be more distinguished. In settings where the explosion occurs at great enough depth to contain the gas bubble before it breaches the water surface, the pressure waves produced by the bubble pulses will also register on the pressure trace, at lower amplitudes than the peak pressure.

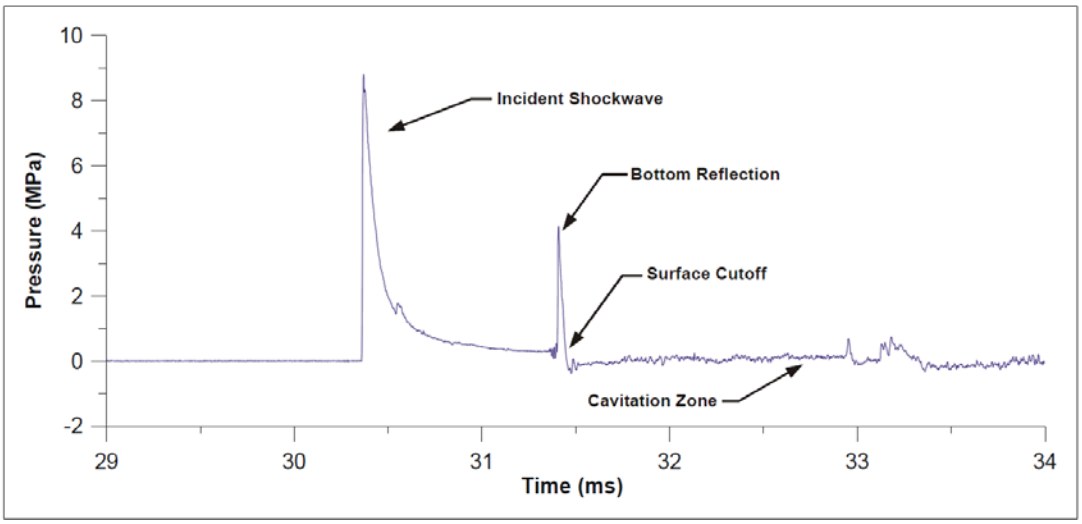

Figure 2.4 Sample Shock-wave Trace of an Underwater Explosion (Rude and Lee 2007)

2.2.1 Pressure Wave Parameters

The primary pressure wave characteristics that define the pressure wave are the peak incident pressure, P_m; the decay constant, θ; the specific impulse (commonly termed "impulse"), I; and the energy flux density, commonly represented with E, but in this study is represented by U to avoid term duplication.

The impulse of the pressure wave is, by definition, the time-integral of the peak pressure, shown in Equation 1.

$$I(t) = \int_{t_a}^{t-t_a} P(t)dt \tag{1}$$

The time increment is typically bounded by the time of arrival of the peak pressure, t_a, and the reflection of surface waves, or by some constant.

Energy flux density, is similar to impulse, but it also contains a term to include the particle velocity of the water, the result of which is considered kinetic energy. Energy flux is determined by the integral of the product of pressure, $P(t)$, and particle velocity, u,

$$U = \int_{t_a}^{t-t_a} u \cdot P(t)dt = \int_{t_a}^{t-t_a} \left(\frac{P(t)}{\rho \cdot c} \right) \cdot P(t)dt = \frac{1}{\rho \cdot c} \int_{t_a}^{t-t_a} P(t)^2 dt \tag{2}$$

where $u = P(t)/\rho c$, ρ is the density of water, c is the acoustic velocity in the water, and the time increment is the same as impulse presented in Equation 1.

The peak incident pressure, P_m, or simply peak pressure, is the measured maximum pressure imposed on the water by the pressure wave. The primary factors relating to the magnitude of peak pressure are the type of explosive, charge weight, and radial standoff distance. Discussion of these factors in greater detail takes occurs in subsequent sections of this paper. Peak pressure is the most commonly referenced pressure wave characteristic, and is easily applied to determine potential damage to structures. It is also the simplest characteristic to comprehend as it acts very similarly to a uniformly distributed load.

Figure 2.5 shows a schematic of the pressure-time history associated with an underwater explosion. P_{max} is the peak pressure. The shaded area under the pressure curve represents the impulse. The decay constant, θ, is a measure of the time it takes for the pressure wave pressure to reduce from P_m to P_m / e, which represents the location where the pressure decay deviates from exponential form. Where e is Euler's Number which is approximately equal to 2.718. The factor $1/2.718 = 0.368$, implies that θ is the time required for pressure to decrease to 36.8% of P_m (Swisdak 1978). Some studies (Chapman 1985) define θ as the phase duration, which is elapsed time between the initial pressure rise and the point where the pressure reduces below the ambient hydrostatic pressure. However, θ is generally considered a time step as shown in Figure 2.5.

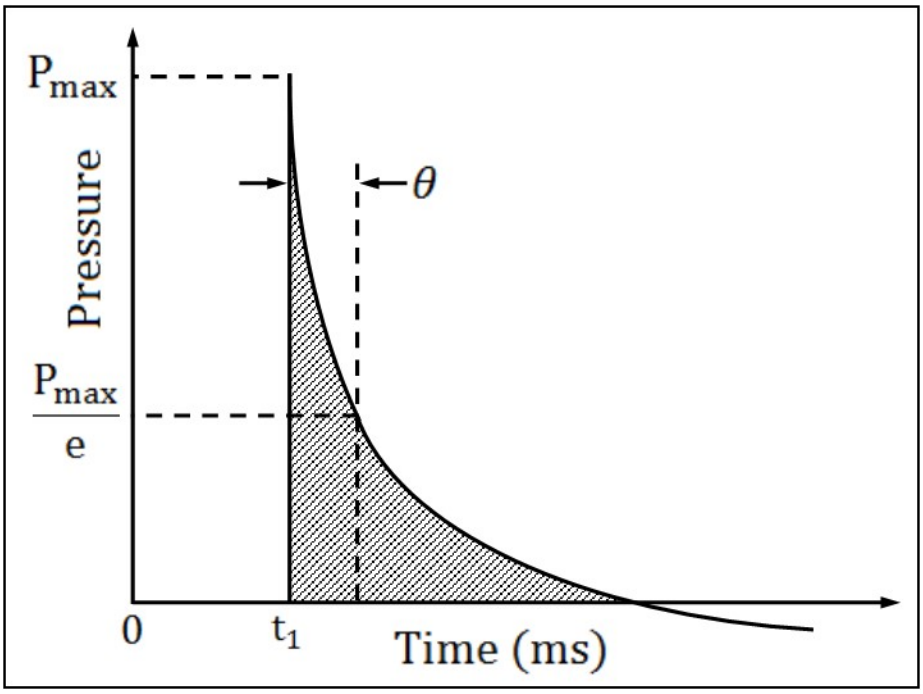

Figure 2.5 Illustration of peak pressure and decay constant (after Rude and Lee 2007)

The actual phase period, or time increment used to calculate impulse and energy flux, will vary with charge type and size, but it is typically bounded by t_a and some multiple of θ to create similitude equations. The time increment 6.7θ was used to develop the similitude equations presented in Cole (1948), and has been used extensively, though 5θ is also common.

Energy flux density is possibly the most comprehensive pressure wave characteristic to determine damage potential to underwater structures (USACE 1961). As the pressure wave passes through the water, the water molecules accelerate, gaining kinetic energy, known here as energy flux. The significance of energy flux is that it includes the effects of both the pressure wave pressure and the particle velocity within the water (Hempen 1993b). Energy flux density has units of energy per unit area (J/m^2) which represents the energy carried by the wave normal to the wave. For example, if the energy flux density of a wave is $2000J/m^2$ and it encounters an object with an area of $4m^2$ takes place, the object receives 8000J of energy. While a typical structure will deform elastically and plastically, for a simple estimation of the force imparted by energy, it can be assumed that all kinetic energy

is converted to elastic strain (elastic deformation) resulting in Equation 3 for maximum allowable force, $F_{\max}$ (Beers et al. 2009),

$$F_{\max} = \sqrt{2kU_k} \tag{3}$$

where k is the spring constant of the object and U_k is kinetic energy. Note, this is a very conservative estimate as some plastic deformation is generally acceptable, which will provide a greater allowable maximum force than determined by this equation.

2.2.2 Similitude Equations

Unique to each underwater explosion are the explosive type, charge weight, standoff distance, and depth of explosion. Each of these parameters is a factor in determining the resulting pressure wave characteristics described previously, which possess the potential to cause significant damage to waterborne infrastructure. However, development of similitude equations in previous studies took place to normalize these parameters in order to predict the pressure wave characteristics for a wide range of settings and charge properties. Development of these similitude equations rely on the basis of the principle of similarity which forms scaling laws. These laws are not physical laws, but rather have demonstrated a remarkable capacity to predict pressure wave characteristics in subsequent and successive trials (Chapman 1985). The principle of similarity suggests that if the same factor by which the charge dimensions change is applied to the scales of length and time at which the pressure wave is observed, the resulting characteristics of the wave will remain the same. Due to the numerous types of explosives, each possessing unique explosive properties, the similitude equations commonly represent the equivalent TNT characteristics, which are then applied to other explosives using an equivalency factor.

2.2.2.1 TNT Equivalences

TNT has long been the industry standard high explosive, due largely to its low sensitivity, low melting point, and substantial energy, making it effective while also relatively safe to handle. Many explosive compounds developed as improvements to TNT still contain considerable portions of TNT, such as Pentolite which commonly consists of fifty percent TNT and fifty percent PETN (Cole 1948). Since TNT has been the prevailing high

explosive for a considerable time, other explosives (including nuclear warheads) are often represented by an equivalent weight of TNT. The TNT equivalence factor is typically calculated by normalizing the energy of explosion for a unit weight of high explosive over the energy of explosion of TNT. The weight of the respective explosive is then multiplied by the TNT equivalency factor to give the equivalent weight of TNT to obtain the same effect, see Equation 4. Other methods are also used, including scaling by the heat of detonation (Cooper 1996).

$$wt(TNT_{equiv}) = \frac{wt(HE) \cdot U_{\exp}(HE)}{U_{\exp}(TNT)} \tag{4}$$

where *HE* represents the high explosive in question, $wt(x)$ is the weight of each respective explosive, and $U_{\exp}(x)$ is the energy of explosion for each explosive.

Employing these factors most commonly occurs out of water, and the accuracy varies with which pressure wave characteristics are being considered and the distance from the source. Therefore, additional consideration is recommended before relying heavily on these factors for underwater explosions. Indeed, the pressure wave data from Rude and Lee (2007), which used C-4 as the explosive, proved much different than TNT equivalency factor predicted. For the current study, it was decided to limit the test data to that measured with the use of TNT to ensure consistency. Especially given that the published TNT equivalences are not necessarily accurate for any given characteristic at any range (Locking 2011). The damage potential and resulting attenuation requirement for TNT induced pressure waves provides a general form which may be applied for pressure waves induced by other high explosives. The damage potential is simply determined by peak pressure and energy flux density, and thus is not dependent on explosive type. However, the prediction of such characteristics is dependent on the explosive material and thus caution is recommended if TNT equivalencies are used for this purpose. In the event an equation does not exist for peak pressure, or its accuracy is uncertain, the U.S. Army Corps of Engineers (1991) recommends using an upper estimate of 2.0 for the TNT equivalency factor as a conservative estimate of the actual effect of common high explosives. However, in shallow water, where the initial expansion of the gas bubble breaks the water surface, the actual peak pressure may be as much as 10 times less than the similitude equations predict. Thus

it is important, when possible, to determine the actual pressures that might be produced, especially to avoid severely overdesigning a mitigation system (USACE 1991).

Table 2.1 displays TNT equivalency factors for several common high explosives. These factors scale the weight of TNT required to obtain similar peak pressures created by the respective explosive type, but may be inaccurate for other characteristics.

Table 2.1 TNT Equivalency Factors for Selected High Explosives (USACE 1991)

Explosive	Approximate Equivalency Factors by Weight for Pressure
TNT	1
Nitromethane	1.1
Pentolite	1.04
ANFO	0.3-0.82
C-4	1.37
Ammonia Dynamite	0.7-0.9
Gelatin Dynamite	0.7-0.8
Nitroglycerin Dynamite	0.9

2.2.2.2 Similitude Equation Formation

Similitude equations were developed using measured pressure wave characteristics and known experimental variables such as charge weight, radial standoff distance, and explosion depth. Since similitude equations are experimentally determined, the validity of each equation is limited to the experimental constraints used for the development of each respective equation (Swisdak 1978). Table 2.2 lists the validity range for the equations of several pressure wave characteristics developed by Swisdak (1978). Due to the wide variety of scenarios requiring pressure wave predictions, and the relative consistency of the equations from different experiments, some exceptions beyond the published validity range may be acceptable for rough estimates. For example, if a peak pressure of 150MPa was predicted using the equation presented by Swisdak (1978) it would be reasonable to assume that the prediction was still relatively accurate.

Table 2.2 Validity range for similitude equations variables (Swisdak 1978)

Parameter	Variable	Validity Range
Peak Pressure (P_m)	P_m	3.4 – 138MPa
Peak Pressure Decay	$t-t_{peak}$	$< 2\tau$
Decay Time Constant (θ)	P_m	3.4 – 138MPa
Impulse (I)	P_m	3.4 – 138MPa
Energy Flux Density (U)	P_m	3.4 – 138MPa

τ = time constant of initial decay

Many assumptions are made when using similitude equations, some of which are presented in Table 2.3. The most critical assumptions are that there are no effects from the boundary surfaces and that the structure is beyond the maximum gas bubble radius. (Swisdak 1978).

Table 2.3 Assumptions Required for Similitude Equations

Assumption	Characteristic Affected	Impact
No boundary surface effects	Pressure wave, gas bubble, bubble pulse	No reflection of shock wave. No cavitation or free surface effects. All similitude equations based on explosions that took place significantly far away from boundary surfaces.
Radial standoff distance is greater than bubble radius	Pressure wave	Pressure wave calculations do not include pressures imposed by contact with gas bubble
Bubble pulses not significant	Pressure-Time History	Pressure pulses on structure are ignored
Spherical Propagation	Pressure wave, gas bubble	Pressure waves radiate in all directions at equivalent amplitudes
Incompressible Fluid	Pressure wave	The water does not attenuate the pressure wave with distance

To understand the formation of similitude equations, it is important to first understand the reduced, or scaled, weight term, $W^{1/3}$, that is used to scale radial standoff distance and pressure wave characteristics. Cole (1948) observed that the pressure-time histories for different charge weights detonated at the same radial standoff distance were identical when

corrected for the difference in time scale. Since the linear dimensions of a spherical charge are proportional to the cube root of the volume, and thus weight, the distances in the above experiment should be scaled by $W^{1/3}$. It was determined by subsequent experiments that pressure wave characteristics dependent on the pressure-time history, such as impulse and energy flux density, may be scaled by the same factor. By scaling experimental results by the cube root of the charge weight, similitude equations can be produced that relatively accurately predict the pressure wave behaviors for various charge weights (Cole 1948).

The scaled distance term, $R/W^{1/3}$, is used to normalize the pressure wave characteristics given any radial standoff distance and charge weight (within the experimental constraints used in the development of the equations). By normalizing these characteristics, data from experiments with varying R and W can be accurately compared, producing a more complete data set. This also allows data to be extrapolated to cases that do not have experimental data, such that analytical or numerical models can be produced with relative confidence.

The basic similitude equation for peak pressure, P_m, after Swisdak (1978), is shown in Equation 5.

$$P_m = K_1\left(\frac{R}{W^{1/3}}\right)^{A_1} \tag{5}$$

where W is the mass of the charge (kg), R is the radial standoff distance (m), and K_1 and A_1 are peak pressure coefficients for this equation. The subsequent decay of the pressure is represented as a multiple of the time constant, θ, which is given by Swisdak (1978) as,

$$\theta = K_2 W^{1/3}\left(\frac{R}{W^{1/3}}\right)^{A_2} \tag{6}$$

where W and R are the same as Equation 5, and K_2 and A_2 are coefficients for the θ similitude equations. The values determined for P_m and θ at R using these equations can then be used to approximate the pressure-time history using the following equation from Cole (1948),

$$P(t) = P_m e^{\frac{-t-t_a}{\theta}} + P_o \tag{7}$$

where P_o is the ambient hydrostatic pressure at depth, z, t_a is and the time for the pressure wave to reach the structure, or time of arrival.

The equations for impulse and energy flux density are,

$$I = K_3 W^{\frac{1}{3}} \left(\frac{R}{W^{1/3}} \right)^{A_3} \tag{8}$$

$$U = K_4 W^{\frac{1}{3}} \left(\frac{R}{W^{1/3}} \right)^{A_4} \tag{9}$$

where W and R are the same as above, K_3 and A_3 are coefficients for the impulse similitude equations, and K_4 and A_4 are coefficients for the energy flux density similitude equations.

Table 2.4 presents the coefficients K_i and A_i for several common explosives. These values are merely common examples of the coefficients, as they are frequently modified to fit the results of supplementary experiments. These were developed experimentally, not using TNT equivalencies, and thus are more reliable than using the TNT similitude equation and scaling the explosive.

Table 2.4 Similitude coefficients for various high explosives (after Swisdak 1978)

Explosive	P_m		$\theta / W^{1/3}$		$I / W^{1/3}$		$U / W^{1/3}$		Range of Validity*
	K_1	A_1	K_2	A_2	K_3	A_3	K_4	A_4	
TNT	52.4	-1.13	0.084	0.23	5.75	-0.89	84.4	-2.04	3.4 - 138
Pentolite	56.5	-1.14	0.084	0.23	5.73	-0.91	92.0	-2.04	3.4 - 138
H-6	59.2	-1.19	0.088	0.28	6.58	-0.91	115.3	-2.08	10.3 - 138
HBX-1	56.7	-1.15	0.083	0.29	6.42	-0.85	106.2	-2.00	3.4 - 60
HBX-3	50.3	-1.14	0.091	0.22	6.33	-0.90	90.9	-2.02	3.4 - 60

P_m = Peak Pressure (MPa); $\theta/W^{1/3}$ = Reduced Time Constant (ms/kg$^{1/3}$); $I/W^{1/3}$ = Reduced Impulse (kPa-s/kg$^{1/3}$); $U/W^{1/3}$ = Reduced Energy Flux Density (m-kPa-s/kg$^{1/3}$); W = Charge Weight (kg); R = Radial Distance (m); I and E are integrated to a time of 5θ.

Note: All equations are of the form: $Parameter = K(R/W^{1/3})^A$

* Validity range of the pressure (in MPa) over which the equations apply

2.3 Damage Potential from Underwater Explosions

The load-structure interaction from explosion induced dynamic loading, on a structure is very complicated when considered in its entirety, and is unique for each situation. Therefore, conservative approximations and simplifications are commonly implemented to convert the effect of dynamic loading to an equivalent static loading. Biggs (1964) presented the process and equations, along with tabulated data, to develop equivalent systems. However, many of the parameters required to produce an equivalent system are dependent on the characteristics of the structure, including but not limited to, material strength, stiffness, mass, and natural frequency. Therefore, the development of an equivalent system will be discussed, but only the simplest application was applied in the analysis.

In general, the response of a structure will depend on its natural period and the time-pressure relationship of the pressure wave. In cases where the pressure wave period (duration) is much longer than the natural period, the load acts as a quasi-static force and damage can be determined using static analysis. In such cases, the deformation is a function of the peak pressure and the stiffness of the structure (Cormie et al. 2009). Figure 2.6 shows the time-pressure relationship of the wave and the time-displacement relationship of the structure. In this case the structure reaches its maximum displacement before the pressure wave faces significant decay.

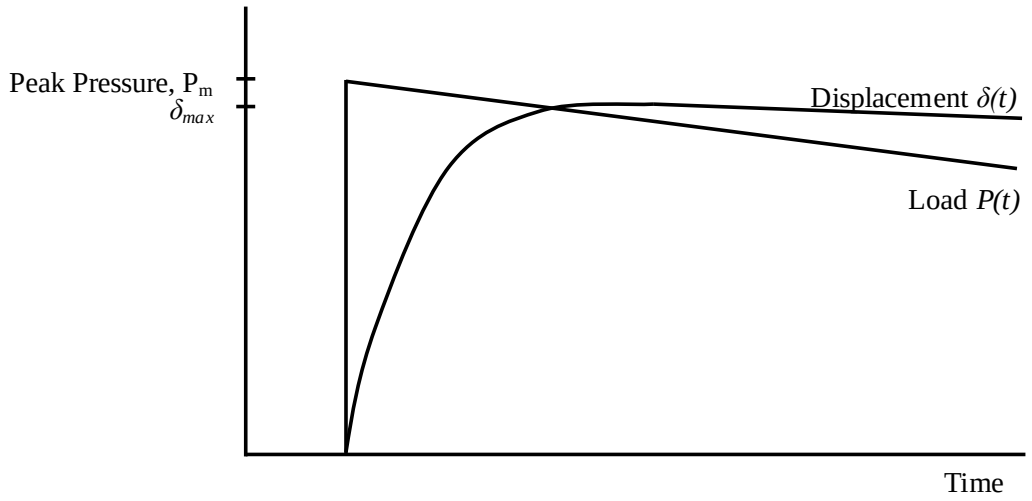

Figure 2.6 Quasi-Static Loading (Cormie et al. 2009)

In cases where duration of the pressure wave is much shorter than the natural period of the structure, the pressure is applied and decays before significant displacement of the structure occurs, as seen in Figure 2.7. In these cases the load is impulsive, and pressure wave impulse has been shown to control the damage propagation (Cormie et al. 2009).

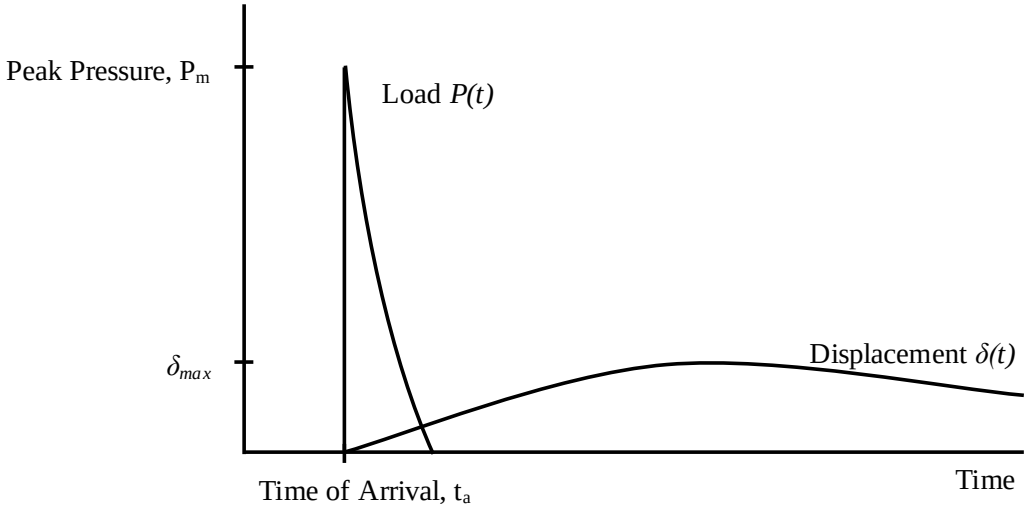

Figure 2.7 Impulsive Loading (Cormie et al. 2009)

The final case, in which the duration of the wave and structure natural period are approximately equal, the response is generally quite complex and may require a complete assessment of the anticipated motion of the structure, see Figure 2.8.

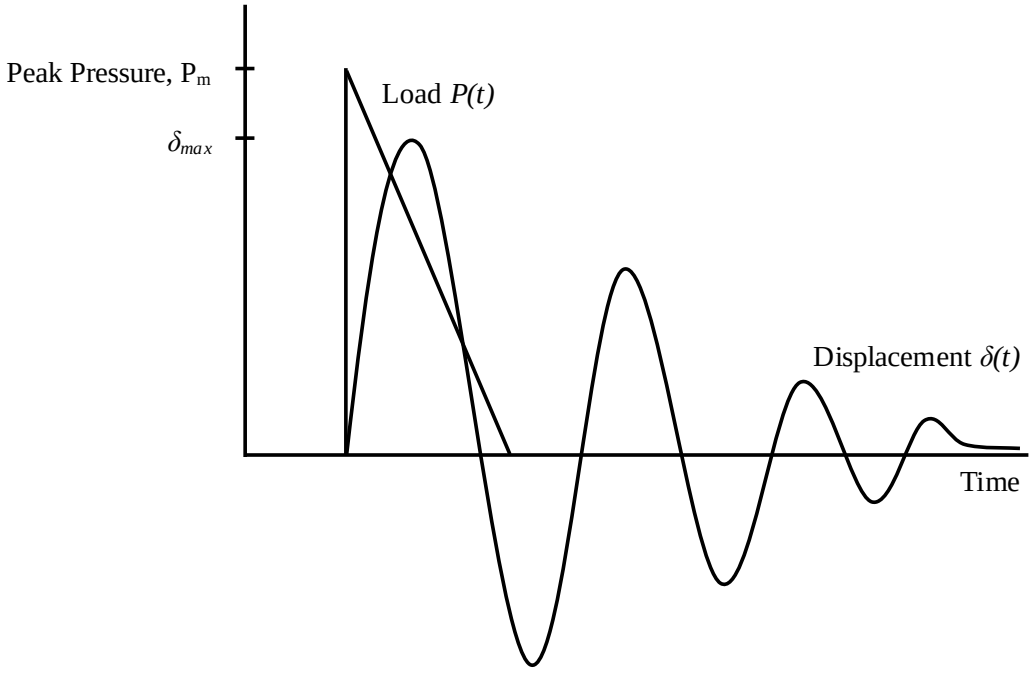

Figure 2.8 Dynamic Loading (Cormie et al. 2009)

2.3.1 Equivalent Systems

The use of an equivalent system converts the response of a structure to a dynamic load to an equivalent static load. To facilitate the application of an equivalent system it is advantageous to model a system as having a single-degree-of-freedom (SDOF). This allows the same equivalent system to be applied to a variety of structural systems. The equivalent system is usually determined by establishing the deflection that would be caused by applying the dynamic load statically. In order to do this, transformation factors were developed for mass, load distribution, and resistance that convert the real system into the equivalent system (Biggs 1964). These transformation factors are used, with the physical properties of the member, to determine a dynamic load factor (DLF) from design figures presented by Biggs (1964). The DLF effectively converts the dynamic load applied to the structure to the static load that would produce the same response.

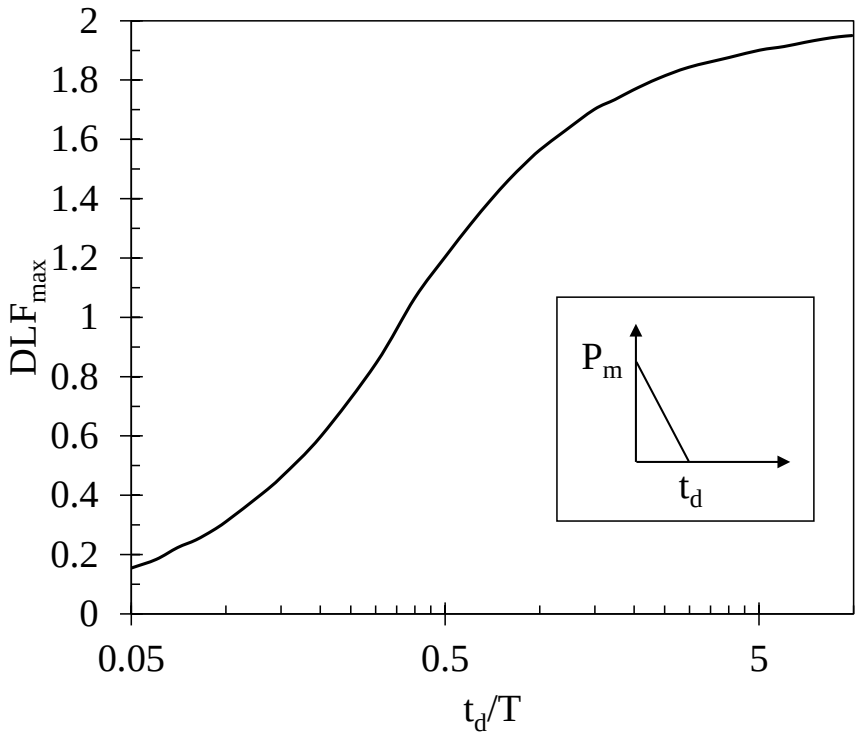

Figure 2.9 Maximum Response of SDOF Systems Subjected to a Triangular Load Pulse Having Zero Rise Time (after Biggs 1964).

Figure 2.9 depicts the DLF values for a system subjected to a triangular load pulse, similar to the loading due to explosive pressure waves. From this figure, it was observed that for impulsive loading ($t_d << T$) the DLF is beneficial to the structure (DLF < 1), and for quasi-static loading ($t_d >> T$) the DLF is detrimental to the structure (DLF > 1).

2.3.2 Dynamic Increase Factors

The dynamic strength of concrete and steel is known to increase proportionally as the load-rate increases. When concrete and steel are subjected to rapid loading, characterized by a high strain-rate, there is an immediate strengthening of the material, which can be accounted for in design, see Figure 2.10 for the behavior of concrete.

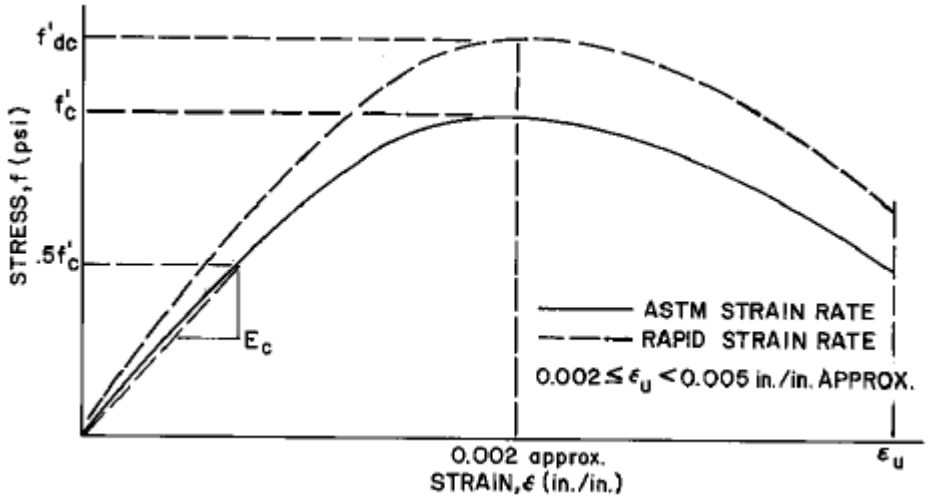

Figure 2.10 Stress-Strain Behavior of Concrete under Rapid Loading (UFC 3-340-02 2008)

To quantify this increase, a dynamic increase factor (DIF) is determined using the strain rate and nominal material strength, and then applied to the nominal design strength to increase it accordingly. Since this behavior is predictable, DIFs have been developed to more accurately model the yield and ultimate strengths of these materials in design. UFC 3-340-02 (2008) contains figures and tables, as well as equations, to determine the appropriate DIF for various material strengths and loading characteristics. Figure 2.11 for concrete and Figure 2.12 for structural steel were used in this study, see below. These factors are determined as a function of the strain rate, ε', which in turn is a function of the pressure wave characteristics, the structural response, and the material properties. UFC 3-340-02 (2008) simplifies this criteria by assigning strain rates, $\varepsilon' = 0.3 mm/mm/\sec$ for

the near design range (small radial distance from charge) and $\varepsilon' = 0.1 mm/mm/\sec$ for the far design range. Additionally, the report states that these strain rates are conservative and thus safe for design. For the purpose of this study, $\varepsilon' = 0.3 mm/mm/\sec$ for a near design range will be used for all loading and material types, except for tension and compression in steel discussed later.

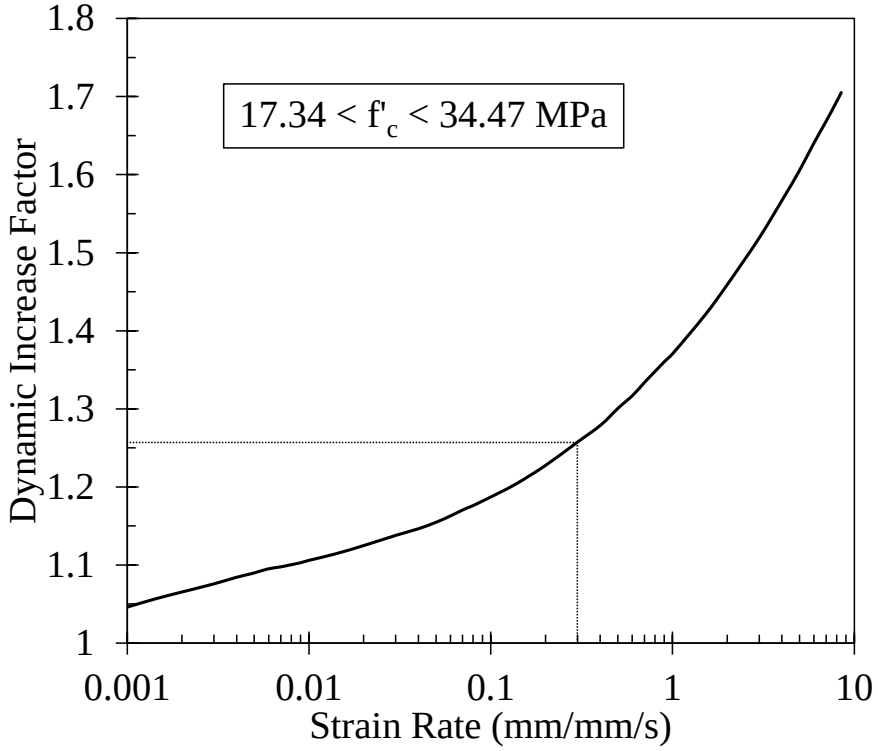

Figure 2.11 Design curve for DIF for ultimate compressive strength of concrete with 17.24 < f'_c < 34.47 MPa, (after UFC 3-340-02 2008)

Figure 2.11 shows an exponentially increasing curve for the DIF values, for concrete with compressive strength between 17.34 and 34.47MPa. Using the strain rate of $\varepsilon' = 0.3 mm/mm/\sec$, indicates a DIF of approximately 1.25. While DIF values are presented for concrete alone, when considering the structural response of a reinforced concrete structure, the DIF values for the reinforcing steel must be considered as well. Additional design curves as equations are presented for higher strength concrete in UFC 3-340-02 (2008).

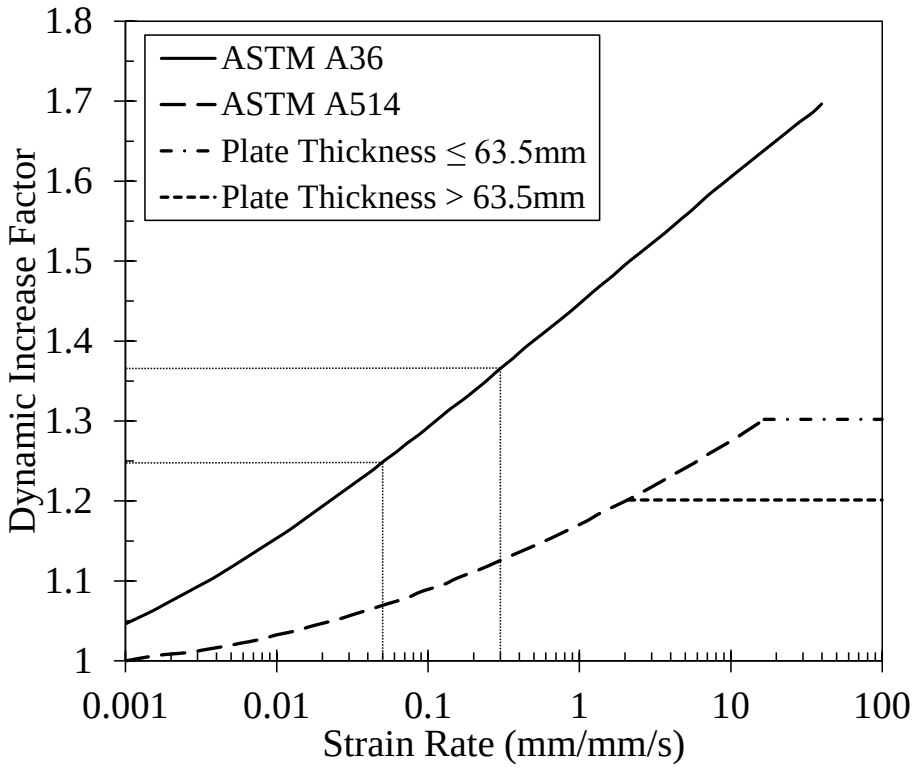

Figure 2.12 DIFs for yield stresses of ASTM A36 and A514 steels (After UFC 3-340-02 2008)

Figure 2.12 presents the DIF values for ASTM A36 and ASTM A514 steels which have different yield strengths. While both curves increase exponentially, it is clear that the DIF values for A36 steel are significantly higher.

2.3.3 Damage Potential of Peak Pressure

When structures are exposed to explosion-induced pressure waves, they undergo rapidly applied dynamic loading. The analysis of members under dynamic loading is similar to static loading though additional considerations must be made to account for material behavior under rapid loading, and the response to kinetic energy imparted from the water.

In general terms, static equilibrium and conservation of energy must be satisfied. Static equilibrium is satisfied using basic static design principles. Kinetic energy imparted by the water must equal the strain energy developed within the system. The kinetic energy is essentially translated into strain energy within the system, first as elastic strain, and then as plastic strain if the kinetic energy is greater than the elastic strain energy. The ductility of a member is its ability to deform in the plastic range without rupture. Therefore, with

the exception of sufficiently stiff members capable of remaining in elastic strain, higher ductility will result in lower required ultimate resistance of the material (UFC 3-340-02 2008).

An example of the relationship between peak pressure and radial standoff distance is shown in Figure 2.13.

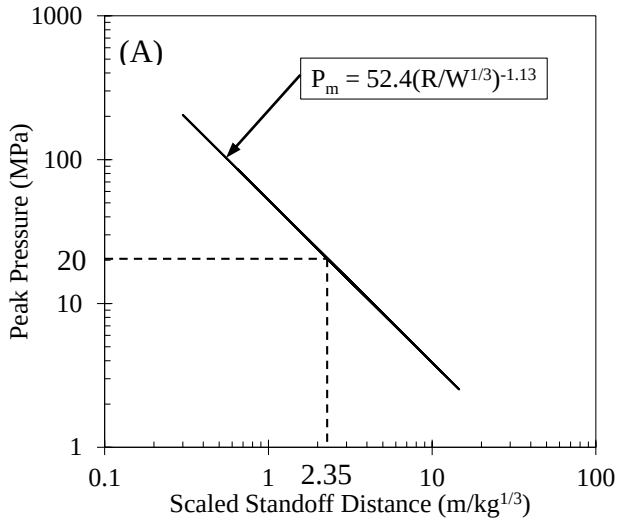

$$P_m = f_c^{'} = 20MPa \qquad \text{(B)}$$

$$20MPa = 52.4\left(\frac{R}{W^{1/3}}\right)^{-1.13}$$

$$\frac{R}{W^{1/3}} = 2.35\frac{m}{kg^{1/3}}$$

$$1)\ R = (250kg)^{1/3} \cdot 2.35\frac{m}{kg^{1/3}} = 14.8m$$

$$2)\ W = \left(\frac{8m}{2.35\frac{m}{kg^{1/3}}}\right)^3 = 39.5kg$$

Figure 2.13 Example Calculations based on Allowable Peak Pressure and Scaled Radial Standoff Distance.

In Figure 2.13 the allowable peak pressure was set as the compressive strength of concrete, 20MPa. Referencing allowable peak pressure in Figure 2.13(A) or using Equation 5, the scaled radial standoff distance was calculated. Then by solving for each parameter, 1) the minimum radial standoff distance for a 250kg charge was determined to be 14.8m, and 2) the maximum charge weight for an 8m radial standoff distance was determined to be 39.5kg. This is a useful method to determine the required radial standoff distance, or to limit the charge weight. However, the concrete compressive strength could be increased using a DIF, the similitude equation presented by Swisdak (1978) does not consider the effect of depth, and the only method to limit the peak pressure at contact is by increasing the standoff distance or by decreasing the charge weight.

Sulfredge et al. (2005) presented a study that predicted the damage potential of an underwater explosion inside a hydroelectric (or water treatment) intake structure. This study determined that in a relatively small and enclosed space such as an intake structure, the effects of even a relatively small explosive would likely be significant. Part of the analysis investigated the gas bubble produced by the explosive. Within the radius of this bubble, the blast pressures exceed 34,000MPa for a 25kg TNT charge. It was predicted that within the gas bubble, pipes would be irreparably crushed or bent, and that little of the affected infrastructure would remain undamaged. Further from the gas bubble, the pressure attenuates quickly and thus the damage is less severe. However, in an enclosed space the reflections off water-solid interfaces compounds and the bubble-pulse does not propagate to the surface and thus provides more damage potential than in a free-water setting. Additionally, it was predicted that damage to concrete would also occur, but the debilitating damage in this scenario would be to the metal pipes and mechanical hardware (Sulfredge et al. 2005).

2.3.4 Damage Potential of Impulse

The damage potential of impulse is closely related to the natural frequency of the structure. If the period of the pressure wave, 6.7θ as presented by Cole (1948), is much shorter than the natural frequency of the structure, impulse will likely be the primary influence on damage. This situation is most common in massive rigid structures such as dams. Impulse imparted to a structure causes the structure to vibrate at its natural frequency, if the deflection due to these vibrations is excessive, damage is sustained (Langefors and Kihlstrom 1978). As mentioned previously, impulse is the integral of pressure over time, or the sum of pressures over time (Sulfredge et al. 2005). Thus, the impulse for an explosion with a large peak pressure but short time constant could be lower than the impulse corresponding to a smaller peak pressure with a long time constant. This being the case, mitigation techniques that reduce peak pressure by distributing it over a longer period of time may not be effective in reducing impulse.

2.3.5 Damage Potential of Energy Flux

The damage potential of energy flux is determined by the strain energy available in the structure. Since conservation of energy must be satisfied, the amount of energy imparted

to the structure must be accounted for in strain energy (Beers et al. 2009). For very resilient structures or minimal energy flux, this will be contained within elastic strain energy, in which the energy imparted to the structure only causes elastic deformation. In most cases involving explosions, due to the large quantities of energy imparted to the structure, plastic deformation (plastic strain energy) will occur, in which some irreversible damage is sustained. Many structures that are designed with explosive forces in mind will provide weak, non-critical elements to absorb a significant portion of the imparted energy in plastic strain, allowing the rest of the structure to remain in elastic strain (AISC 2011). This prevents total failure of the structure, and reduces the loss of property and/or life. The sacrificial members can be replaced following the damaging event. In many cases, the cost of repairs due to some plastic deformation will be less than the cost to limit deformation to the elastic range, whether through robust design or mitigation practices. For existing structures, the level of plastic deformation permitted should be determined prior to determining the allowable energy flux that can be imparted to the structure. For extreme events, the available plastic strain energy may not be great enough, leading to rupture and/or projectile motion to satisfy energy conservation. Thus, the damage potential of energy flux is characterized by what level of deformation is considered acceptable, and by the stiffness of the structure which determines the available strain energy.

Energy flux density is the pressure wave characteristic that best relates the damage causing potential of a pressure wave, because it combines peak pressure and shock wave induced kinetic energy of the water. Figure 2.14 shows the relationship of scaled energy flux density versus the scaled radial standoff distance. Since energy flux is determined in part by the integral of pressure with respect to time (Equation 2), it can be scaled by charge weight similar to the scaling of standoff distance (Cole 1948). The rate at which the energy flux decays in Figure 2.14 is much greater that of peak pressure as seen in Figure 2.13. Equation 2 demonstrates that energy flux is a function of pressure squared, which explains this behavior, but also indicates that the damage potential of energy flux will also be a function of pressure squared (Rude and Lee 2007).

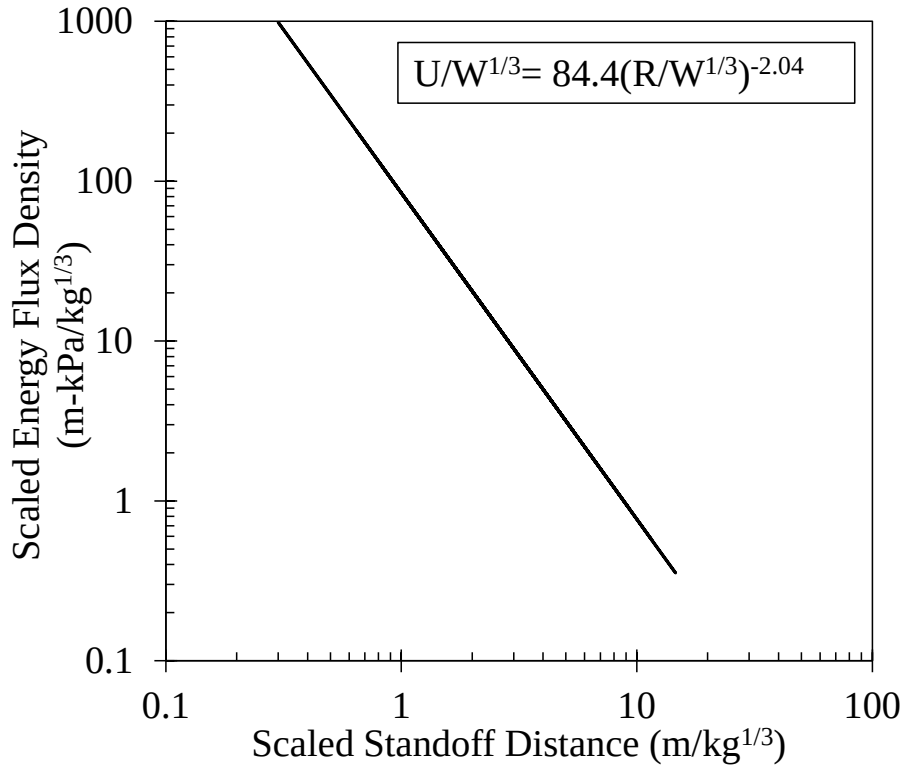

Figure 2.14 Scaled energy flux density versus scaled radial standoff distance (Swisdak 1978)

Using the previously presented similitude equation and parameters for energy flux density, the relationship between radial standoff distance and charge weight can be established for a specified maximum energy flux. By rearranging the terms in Equation 9, the minimum required standoff distance for a given charge weight and specified maximum energy flux can be determined, see Equation 10.

$$R = \frac{W^{1/3}}{\left(\frac{U}{K_4 W^{1/3}}\right)^{1/A_4}} \tag{10}$$

2.4 Bubble Screens

The study of bubble screens to attenuate pressure waves characteristics began in the early 20th century. Possibly the first practical application of a bubble screen was presented by Fessenden (1920) to block generation and reception of sound waves on naval ships. Extensive testing commenced during World War II and continued in the immediate

postwar years, primarily for the use of protecting ships and divers from underwater explosions. The first commercial application to protect a waterborne structure occurred in 1954 by the Electric Power Commission of Ontario during the construction of a hydroelectric facility. Following several scaled tests to confirm pressure wave attenuation, a bubble screen was implemented during the blasting of a rock mass near the facility, see Figure 2.15. Typically this would have required ceasing hydroelectric operations and draining the water before blasting, however, by implementing the bubble screen, operations continued saving a large sum of money (Domenico 1982a).

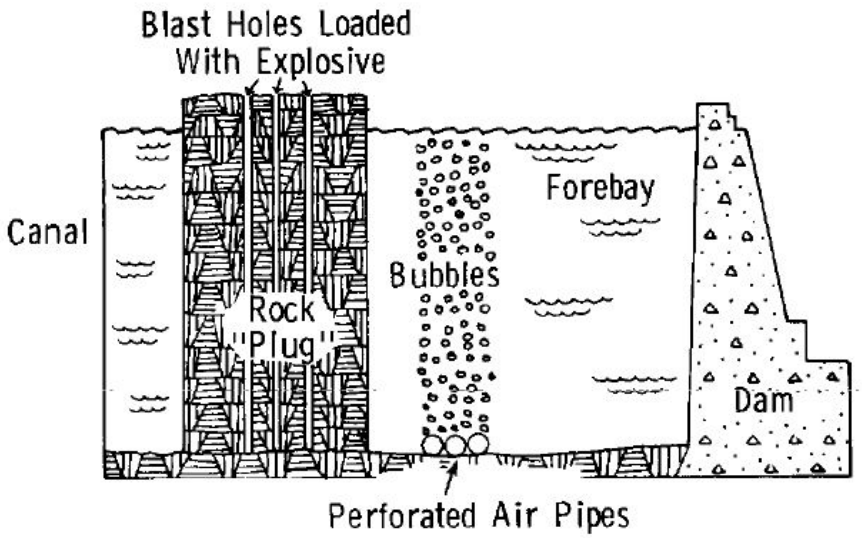

Figure 2.15 shows the use a bubble screen to reduce the blast induced pressures while removing the rock plug separating the canal from the forebay by the Electric Power Commission of Ontario (Domenico, 1982a).

In recent years, a common, and sometimes required, application of bubble screens is for the protection of aquatic wildlife during underwater demolition and pile driving operations (Keevin and Hempen 1997). The high amplitude sound pressures produced by explosions and the heavy hammering of piles adversely affects animals residing in the surrounding water. Historic observations witnessed high levels of fish mortality and permanent hearing loss in marine mammals near such operations. Traditional techniques to protect wildlife largely relied on the use of small preliminary charges or other acoustic sources to scare the wildlife from the vicinity of the commencing operation. However, by adapting bubble screens to surround these underwater activities, the attenuation of the resulting sound

pressures proved to limit or eliminate any observable damage to the aquatic wildlife (Grogan 2005). The theory and the application of bubble screens for protection of aquatic wildlife from acoustic pressures is essentially the same as the application of them for structural protection, and thus research for both purposes is interchangeable.

2.4.1 Principles of Operation

A bubble screen consists of a screen (wall or curtain) of air bubbles that rise through the water. It is created by sending compressed air through an underwater manifold of pipes that have many small holes or orifices. As the air exits the manifold through these orifices, small bubbles form that then rise to the surface. The bubble screen is designed to separate a pressure wave creating source (e.g. explosive) from a potential target (e.g. a structure or animal). This has been accomplished by either surrounding the source or barricading the target. Thus, the bubble screen effectively creates a protective barrier within the water. In free-water (i.e. no boundaries or air), a pressure wave travels at the speed of sound until reaching a barrier which will partially reflect and partially attenuate the pressure wave, allowing a fraction of the original amplitude pass through.

2.4.2 Attenuation Mechanisms of Bubble Screens

The primary pressure wave reducing mechanisms of bubble screens are reflection and attenuation. The term “attenuation” commonly refers to the total reduction of amplitude beyond the bubble screen, which is attributable to both mechanisms, however a distinction will be made in this section to differentiate the two. The bubble screen has a reduced density and increased compressibility compared to the surrounding water, which creates a different acoustic impedance than the water. This difference in impedance causes a portion of the pressure wave to reflect back into the free-water, similar to the rarefaction wave reflected from the water-air interface (Hempen 1993b). The remaining energy of the pressure wave attenuates though adiabatic compression of the bubbles and reradiation as it enters the bubble screen (Domenico 1982a).

2.4.2.1 Reflection

Reflection of the pressure wave is due largely to the difference in acoustic impedance encountered at the interface of the water and bubble screen. The equation for acoustic impedance was given in Cole (1948) as,

$$Z = \rho \cdot c \tag{11}$$

where Z is the acoustic impedance, ρ is the density of the medium, and c is the acoustic velocity in the medium.

For known densities of the water and air, the density of the bubble screen, considered a homogenous medium, can be determined using the fractional air content present in the bubble screen. An equation for the density of air as it relates to the ambient hydrostatic pressure, P_o, was presented in Domenico (1982a).

$$\rho_a = 0.01183 \cdot P_o^{1.0086} \tag{12}$$

where P_o is in kPa and is the ambient hydrostatic pressure determined by the following equation:

$$P_o = P_{atm} + \rho_w g z \tag{13}$$

where P_{atm} is the atmospheric pressure at the surface, assumed to equal $1.013 \times 10^5 Pa$ ($1 atm$), ρ_w is the mass density of water (the effect of depth is considered negligible), g is the gravitational constant (9.81m/s^2), and z is the depth of interest in meters.

Equation 14 is used to determine the mass density of the mixture, ρ_m, for a known fractional air content f_a,

$$\rho_m = f_a \rho_a + (1 - f_a)\rho_w \tag{14}$$

The acoustic velocity of the mixture, c_m, is determined using the following equation presented in Domenico (1982a) for $z \leq 50\ m$,

$$c_m = \sqrt{\frac{1}{\beta_m \rho_m}} \tag{15}$$

where β_m is the compressibility of the mixture and ρ_m was previously calculated. β_m is determined by scaling the compressibility of air and water by the fractional air content, f_a, similar to ρ_m. The compressibility of air, β_a, is pressure dependent and differs for

adiabatic and isothermal conditions. The ratio of specific heats of air, *k* (1.4 for the adiabatic condition and 1.0 for the isothermal) is included Equation 16 from Gibson (1970) to account for the different conditions.

$$\beta_a = \frac{1}{k \cdot P_o} \tag{16}$$

The compressibility of water, β_w, is subject to change with variations in pressure and temperature, however, the effect of these variations are small. The compressibility of water from Domenico (1982a) is given as,

$$\beta_w = 4.382 \cdot 10^{-10} \frac{m^2}{N}$$

The equation to calculate the compressibility of the mixture is shown below,

$$\beta_m = f_a \beta_a + (1 - f_a)\beta_w \tag{17}$$

While it is apparent from the previous equations that the acoustic impedance is dependent on the fractional air content, the study by Domenico (1982a) demonstrated that it is also dependent on the radius of the air bubbles. The acoustic velocity, and thus impedance, is very sensitive to the bubble resonant frequency as it approaches and exceeds the frequency of the pressure wave. Equation 18 gives the resonant frequency of the bubble, f_r.

$$f_r = \frac{1}{2\pi r}\left(\frac{3\mu\tau P_o}{\rho_m}\right)^{1/2} \tag{18}$$

where r is the bubble radius in meters, the Polytropic factor $\mu \approx 1/(1+\beta_m)$ for $1/\tau \le \mu \le 1$, the adiabatic exponent $\tau = 1.4$, P_o is in pascals, and ρ_m is in units of kg/m^3. From Equation 18, it is apparent that f_r is inversely proportional to the bubble radius, or the smaller the bubble radius the higher f_r.

Figure 2.16 demonstrates the effect of f_r on both acoustic velocity and attenuation. The plot showing the relationship between acoustic velocity and pressure wave frequency shows the velocity as approximately constant, corresponding to Equation 15, until it nears

f_r. As f_r is approached, the velocity decreases rapidly, before nearly instantaneously increasing past the acoustic velocity of water, c_w. Beyond f_r, the velocity reaches a maximum before falling to the level of c_w. The acoustic velocity maintains the same shape regardless of the bubble radius, but the frequency where f_r is reached increases with decreasing bubble radius.

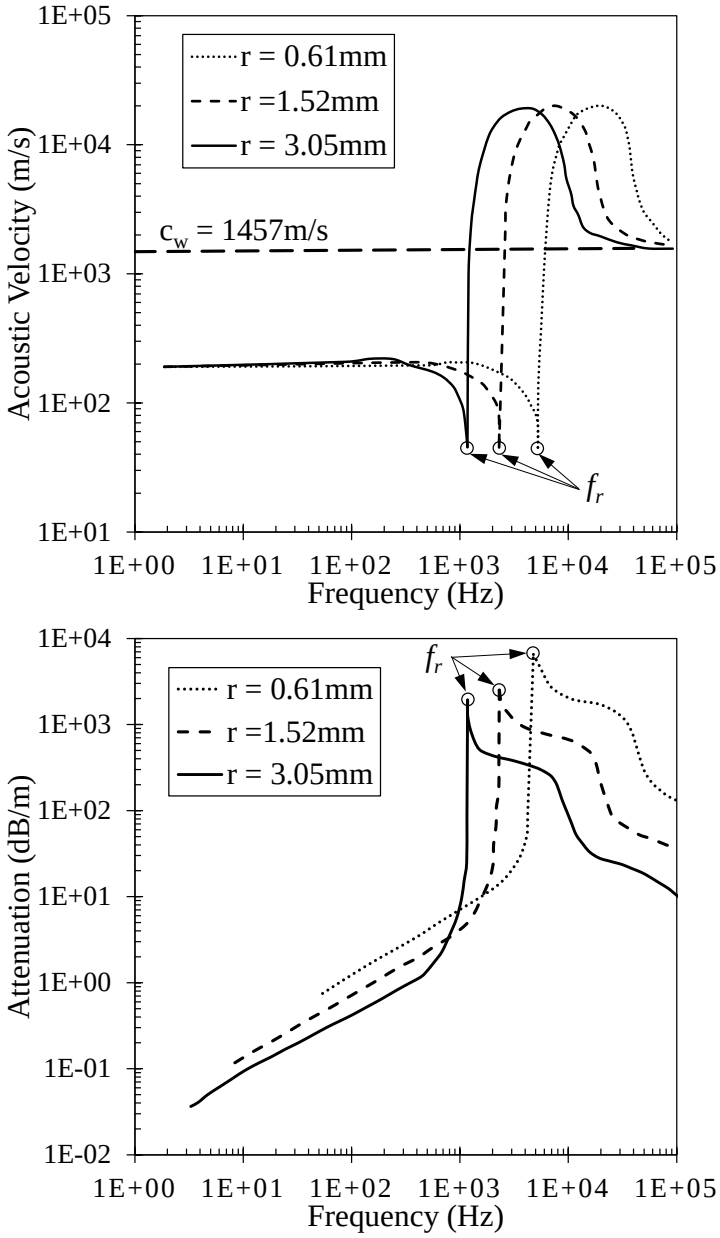

Figure 2.16 Acoustic Velocity and Attenuation versus Pressure Wave Frequency for Different Bubble Radii for $f_a = 0.006$ and $z = 3.66m$ (after Domenico 1982a).

The Knott equations presented in Grant and West (1965) are used to determine the transmission of wave energy across the bubble screen. Combining these with the reflection coefficient given by Kinsler and Frey (1950) for the acoustic impedances of the mixture and water, yields the transmission coefficient, $\left|A_2 / A_1\right|$, see Figure 2.17. The pressure wave amplitude is A_1, the reflected pressure wave amplitude is D_1, and the pressure wave amplitude which transmits through the bubble screen is A_2.

Transmission of Wave Energy:	$A_1 = A_2 + D_1$
Attenuation Ratio:	$\left\|\frac{A_2}{A_1}\right\| = 1 - \left\|\frac{D_1}{A_1}\right\|$
Acoustic Impedance:	$Z_i = \rho_i \cdot c_i$
Reflection Coefficient:	$\frac{D_1}{A_1} = \frac{Z_m - Z_w}{Z_m + Z_w}$
Substituting for the Transmission Coefficient:	$\left\|\frac{A_2}{A_1}\right\| = 1 + \left\|\frac{Z_m - Z_w}{Z_m + Z_w}\right\|$
Transmitted Amplitude:	$A_2 = A_1 - A_1\left\|\frac{Z_m - Z_w}{Z_m + Z_w}\right\|$

Figure 2.17: Derivation of Transmission Coefficient

Figure 2.18 is a sketch of the expected transmission coefficient versus frequency based on the velocities presented in Figure 2.16. As f_r is approached, the behavior of the transmission coefficient becomes difficult to predict, except when $f >> f_r$ in which case it is approximately unity. Therefore, to ensure the reflection potential of the bubble screen may be utilized, it is necessary to produce bubbles that have sufficiently small radii, such that f_r is much greater than the frequency of the pressure wave. Explosives

used for construction and demolition typically have frequencies less that 500Hz (Dowding 1985). For a pressure wave frequency of 500Hz, Figure 2.16 indicates that a bubble radius of 3mm is roughly the largest that should be used when modeling reflection. Since a bubble radius of 3mm should be easily attainable, reflection should be considered a major component of the total predicted attenuation.

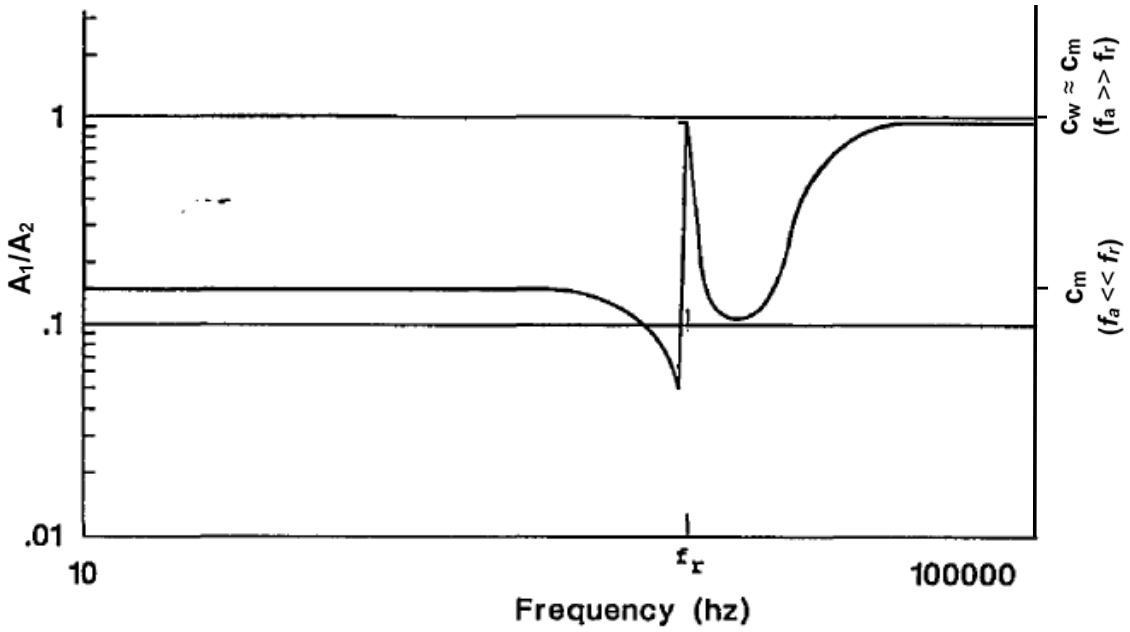

Figure 2.18 Sketch of the Transmission Coefficient for Reflection versus Frequency (after Hempen 1993b)

2.4.2.2 Attenuation

As a pressure wave passes through a bubble screen, it causes the bubbles to oscillate in cycles of compression and expansion, similar to the explosion gas bubble. As the bubbles oscillate, some energy is transformed to heat, which in turn dissipates to the water. Additional energy is reradiated back into the water as compression waves. This action of effectively absorbing the amplitude of the pressure and energy that passes through the bubble screen is called attenuation.

In the study presented by Domenico (1982a), the theory relating to bubble screen attenuation was investigated and empirical equations were presented. Figure 2.16 is the result of the study, and the bottom plot depicts attenuation versus pressure wave frequency.

As noted previously, the frequency created by common demolition explosions is typically less than 500Hz. Therefore from Figure 2.16, the expected attenuation is relatively small compared to the reflection coefficient for this frequency.

The frequency for a bubble radius of 1.52mm at 500Hz is approximately 2.3dB/m according to Figure 2.16. The decibel unit (dB) is the logarithmic amplitude ratio that produces convenient numbers for amplitude ratios, it is given as,

$$dB = 20\log_{10}\left(\frac{A_{fw}}{A_r}\right) \tag{19}$$

Therefore an attenuation equivalent to 2.3dB/m would be:

$$10^{\left(\frac{2.3dB}{20}\right)} = \frac{A_{fw}}{A_r} = 1.3$$

Or using the typical format in this study,

$$\frac{A_r}{A_{fw}} = 0.77$$

Whereas Hempen (1993b) presented a transmission coefficient less than 0.2 for the same pressure wave frequency. As seen in Figure 2.16, near the frequency of the pressure wave, the attenuation mechanism of the bubble screen dramatically increases before falling to intermediate levels. Thus, for pressure wave frequencies significantly below f_r, reflection will be the primary attenuating mechanism, while near f_r and beyond, adiabatic compression of the bubble and reradiation will be the primary attenuation mechanisms. Figure 2.16 also demonstrates the increased attenuation due to smaller bubble radius that is due to the higher f_r.

2.4.3 Required Performance Parameters of a Bubble Screen

By considering the maximum expected peak pressure and energy flux density for a given structure, and the minimum dynamic and impact strengths of the structure material, minimum required attenuation factor of the bubble screen can be determined, which in turn will dictate the specific design parameters of the manifold. It has long been known that the

effectiveness of a bubble screen is due in large part to bubble radius, screen thickness, and the fractional air content of the screen. By determining the required attenuation factor, and utilizing the role of each of these attenuation mechanisms, the appropriate bubble screen system can be designed and implemented.

As a note, the pressure wave characteristics for this analysis are assumed to be for explosions in free-water, not considering the effects of boundary conditions or the explosion gas-bubble, which has significantly higher pressures over a short radius.

2.4.4 Bubble Screen Case Studies

There is an appreciable lack of unclassified data available regarding the attenuation performance of bubble screens on underwater explosions. There is however, a substantial quantity regarding the theory of underwater acoustic attenuation and the attenuation of pile driving induced pressure waves. The *Shock-Wave Attenuation Properties of a Bubble Screen* (USACE 1961) was the primary study referenced for attenuation data, due to the comprehensiveness of the data collected. Other studies, including Rude and Lee (2007) and Hempen (1993b), offer excellent discussion but used explosives other than TNT and provided too few data measurements to adequately correlate to TNT for analysis. Table 2.5, contains peak pressure and energy flux attenuation ratios from three different studies. While all three studies indicate significant attenuation can be attained with sufficient airflow, significant variability between the studies is also evident. The three highest airflows, representing each study, seem to indicate that lower airflow provides greater attenuation, while the three airflows tested by USACE (1961) clearly indicate the opposite, which confirms theoretical predictions presented by Domenico (1982a). Therefore, the likely cause of variation is a combination of different bubble screen characteristics, environmental factors (test location, depth, etc.), instrumentation, and other experimental differences. Also, the first two studies only provide two data points each, which is not sufficient to make accurate correlations, though it does demonstrate the effectiveness of bubble screens in pressure wave attenuation.

Table 2.5 Attenuation Ratios from Different Studies

Source	Airflow $\left(m^3/s/m\right)$	Peak Pressure Attenuation $\left(P_{m,r}/P_{m,fw}\right)$	Energy Flux Attenuation $\left(U_r/U_{fw}\right)$
Rude and Lee (2007)[1]	0.0167	0.41	0.59
Hempen (1993b)[2]	0.0136[4]	0.31	-
USACE (1961)[3]	0.00974	0.26	0.18
	0.00122	0.81	0.66
	0.000389	0.92	0.86

[1] 10kg C-4 charge, water depth = 12.8m, charge and gauge depth = 11.8m.

[2] 1.81kg TOVEX 700 charge, water and charge depth = 1.52m, gauge depth ≈ 1m.

[3] 3.63kg TNT charge, water depth = 5.49m, charge and gauge depth = 2.74m. Attenuations taken from line of best-fit of plotted data.

[4] Estimated based on compressor capacity

Additionally, theoretical approximations presented by Domenico (1982a) were investigated, but the results corresponded inadequately to the measured data to make conclusions regarding the measured versus theoretical performance.

2.4.4.1 Shockwave Attenuation Properties of a Bubble Screen (USACE 1961)

The USACE (1961) study primarily investigated the effects of air content and bubble screen thickness on the rate of attenuation. The tests were performed in a blast pond with the following dimensions: 39.6m long, 30.5m wide, and 6.71m deep. The bubble screen manifold was submerged to 5.49m deep and produced a bubble screen approximately 6m long. TNT charges weighing 3.63kg (8lbs) were detonated at mid-depth between the surface and the manifold. Gauges were placed at mid-depth (2.74m), quarter-depth (1.37m), and just below the surface (0.076m). The gauges extended linearly away from the charge location at regular intervals of 0.223m, beginning 0.610m from the front of the bubble screen to 1.91m behind the screen, see Figure 2.19. The screen thicknesses were varied between 0.152m, 0.457m, and 0.914m.

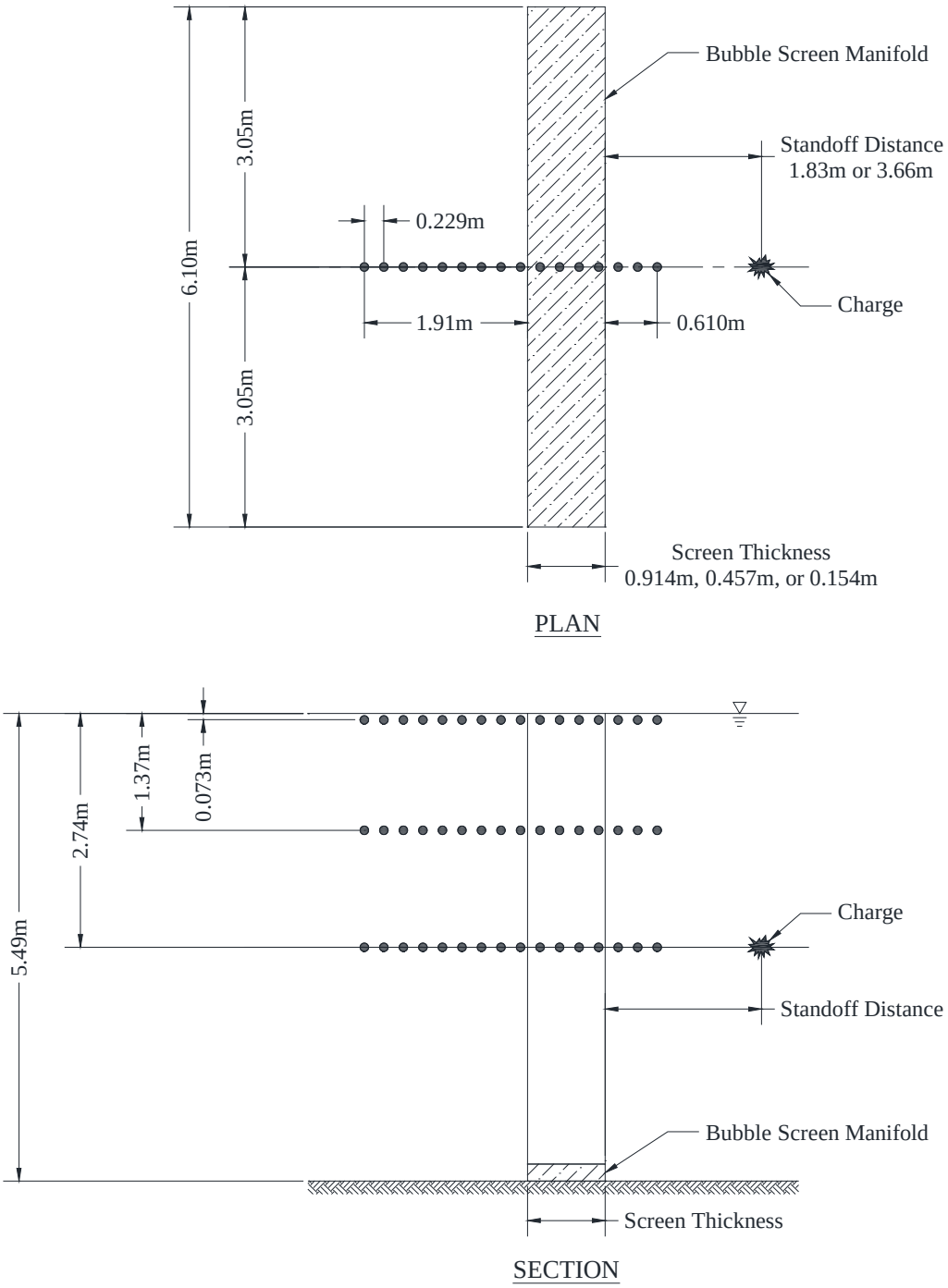

Figure 2.19 USACE (1961) experimental setup including gauge array

The air-content was varied for each screen thickness to yield similar airflows, as shown in Table 2.6. The charge was placed either 1.83m or 3.66m from the front of the bubble screen to determine any discrepancies caused by radial distance to the screen. A control was

established by also performing the detonation and measurements in the free-water condition (without airflow) to provide accurate attenuation data (USACE 1961).

Table 2.6 Bubble Screen Thickness, Air Content, and Air Flow (USACE 1961)

Screen Thickness (m)	Air Content ($m^3/s/m^2$)	Air Flow ($m^3/s/m$)
0.91	0.000427	0.000389
	0.00134	0.00122
	0.0107	0.00974
0.46	0.000853	0.000392
	0.00134	0.000616
	0.0107	0.00492
	0.021	0.00966
0.153	0.00253	0.000386
	0.01067	0.00163
	0.02134	0.00325
	0.04267	0.00650

The results of this study showed strong correlation between attenuation and airflow. The following equations were developed based on the experimental parameters and results, and were converted to metric units.

$$\frac{P_{m,r}}{P_{m,fw}} = 1 - \frac{A_c T_s \lambda}{\nu \cdot 10^5}\left(\frac{1}{\frac{A_c T_s \lambda}{\nu \cdot 10^5} + 0.0556}\right) \tag{20}$$

$$\frac{U_r}{U_{fw}} = 1 - \frac{A_c T_s \lambda}{\nu \cdot 10^5}\left(\frac{1}{\frac{A_c T_s \lambda}{\nu \cdot 10^5} + 0.0278}\right) \tag{21}$$

Where A_c is the air content ($m^3/s/m^2$), T_s is the screen thickness, λ is the scaled radial standoff distance ($m/kg^{1/3}$), and ν is the kinematic viscosity of water ($1.004 m^2/s$ @ 20ºC). In subsequent calculations airflow, $A_f = A_c \cdot T_s$ is typically used. Equation 20 and Equation 21 are valid for the following conditions: $R/W^{1/3} > 3$, $0 < L_s/T_s < 12$, and $0.01 < A_c T_s \lambda / \nu \cdot 10^5 < 1.0$, where L_s is the screen length.

2.4.4.2 San Francisco-Oakland Bay Bridge (CALTRAN 2009)

During the construction of the San Francisco-Oakland Bay Bridge, bubble screens were used to attenuate the acoustic levels caused by the pile driving operation. The results were compiled into a report titled, *Technical Guidance for Assessment and Mitigation of the Hydroacoustic Effects of Pile Driving on Fish* (CALTRAN 2009). In this operation, several different bubble screen configurations were implemented. The results indicated that single stage bubble manifolds were virtually ineffective where currents existed, providing 0-5dB of attenuation, but provided 5-15dB of attenuation with no current. Thus, multiple-stage and confined bubble screen systems were used in high-current situations. For one configuration, a nine-stage manifold was constructed (see Figure 2.20), with each tier having a "bubble ring," or manifold system; but typically only five stages were implemented. This system provided 15-30dB of attenuation, even in high current settings. Thus, even in strong currents there was a sufficiently high air content to effectively attenuate the acoustic noise pressure.

Figure 2.20 Multiple-stage unconfined bubble screen system (CALTRAN 2009)

In other cases, confinement was added to the bubble screen system by use of either a steel pipe or a flexible material, which confined the bubbles to structure vicinity. These systems provided 5-25dB of attenuation. It was noted for the confined system, that the confining material (rigid or flexible) added negligible effect to the attenuation. It was also suggested that it is difficult to predict sound attenuation greater than 10dB (CALTRAN 2009). For

these pile driving examples, the most effective systems placed the bubble screens closely around the piles and ensured the air content of the bubble screen remained at desired levels, either through multiple-stages or confinement.

In the case of pile driving, the source is effectively surrounded by the bubble screen, whereas in structural protection the location of the explosive source may be unknown, therefore structure is essentially barricaded by the bubble screen. This is a difference that needs to be acknowledged before expecting the same results in underwater blast protection. The near proximity available in the CALTRAN (2009) study, and the adaptations made to a single-stage bubble screen may be difficult to implement when protecting structures, however they provide examples of practical modifications that can be made to improve the performance of a bubble screen.

2.4.4.3 Performance Evaluation of the Roach Cove Bubble Screen Apparatus (Rude and Lee 2007)

In 2007, a study was conducted by Defense Research and Development Canada in Bedford Basin, Nova Scotia, Canada, to determine the attenuation properties of a customized bubble screen apparatus. The study was birthed from restrictions placed on the Canadian Navy to protect aquatic wildlife, which limited the permitted charge size and seasons for underwater explosives training. The purpose of the study was to develop a bubble screen apparatus and demonstrate its effectiveness at attenuating pressure wave characteristics, in order to solicit less stringent requirements when the bubble screen is implemented. Fisheries and Oceans Canada (formerly Canadian Department of Fisheries and Oceans) states that acceptable overpressures are less than or equal to 100kPa (~1atm) (Wright and Hopky 1998). For a 10kg C-4 charge, the distance at which natural decay reduces the pressure to this is level can exceed 800m. The resulting tests determined that obtaining this level of reduction near the charge using a bubble screen was not possible, but the distance at which this reduction was attained could be dramatically reduced. The results of the study indicated that this bubble screen apparatus, reduced peak pressures up to 60%, energy flux up to 40%, and the distance to attain pressure levels of 100kPa levels to 195m or 75%, which corresponded to a 94% reduction in the area affected (Rude and Lee 2007).

The bubble screen apparatus implemented by Rude and Lee (2007) was circular, intending to surround an explosive charge, see Figure 2.21. The main distribution pipe was a 3in diameter stainless steel pipe rolled into an 8m circle. Distribution ports were added around the perimeter at 75mm spacing, which supplied air to 500mm long diffusers. The diffusers were constructed of Ethylene Propylene Diene Monomer (EPDM) which were perforated with thousands of slits approximately 1mm in length. These slits would remain closed when air was not flowing, preventing particulates in the water from entering the manifold. As air was supplied to manifold, the EPDM expanded causing the slits to open and air to pass through forming bubbles, see Figure 2.22 (Rude and Lee 2007). While this bubble screen manifold was more elaborate than many other designs, it benefitted by remaining cleaner when not used and by producing a dense screen of small bubbles, which can be difficult to attain from pipes with drilled holes.

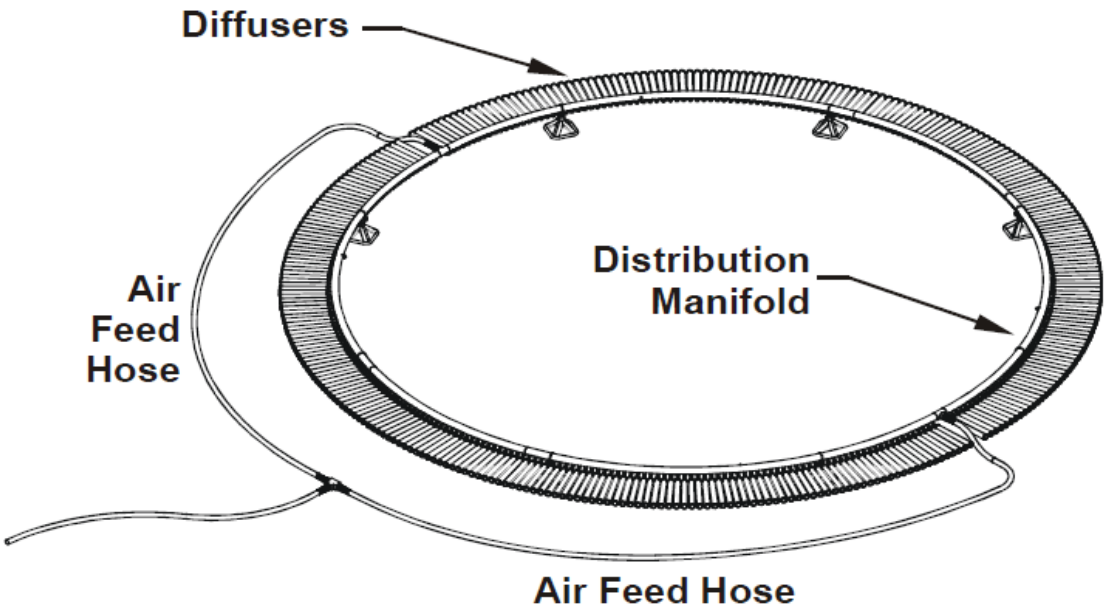

Figure 2.21 Diagram of Bubble Screen Manifold (Rude and Lee 2007)

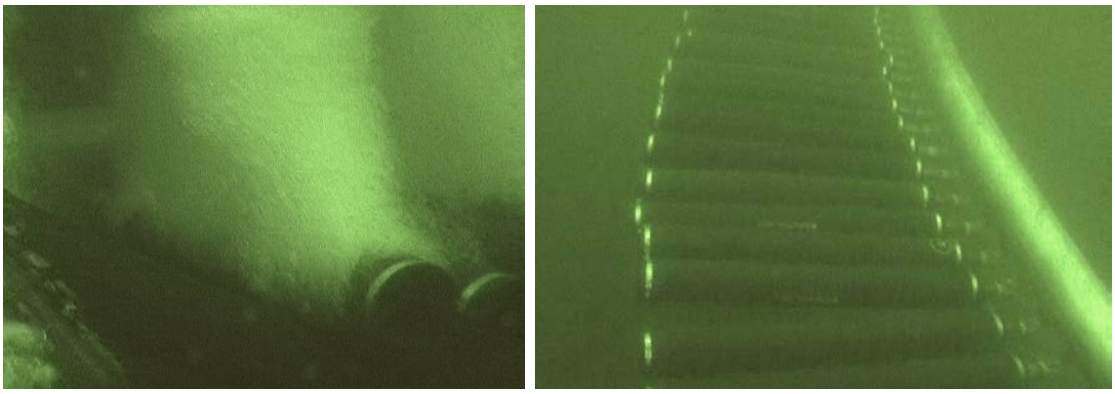

Figure 2.22 Picture of Bubble Screen Manifold with and without Airflow (Rude and Lee 2007)

2.4.4.4 Other Common Uses of Bubble Screens

The remaining common uses of bubble screens, which have more to do with the turbulent effect on the water than the attenuation properties, include creating a pneumatic barrier to contain substances such as oil, to aerate bodies of water to prevent stratification, and deicing operations around structures such as dams (Ditmars and Cederwall 1974).The implementation of a bubble screen to passively protect structures from underwater explosions will inherently incorporate one or more of these additional benefits. For example, if a bubble screen manifold is placed at the bottom of relatively deep reservoir to protect an intake structure, it will effectively reduce stratification in the reservoir, prevent ice buildup on the structure, and reduce acoustic sounds generated by the intake equipment, while passively protecting the structure from underwater explosions.

Several companies have developed proprietary bubble screen systems to fulfill a variety of applications. HydroTechnik Lübeck from Lübeck, Germany is one that has developed several such systems including one that acts as a pneumatic barrier, or weir, to contain surface contaminants such as oil, see Figure 2.23. As seen in the figure, the bubble screen not only causes a vertical rise in the water, it also converts the vertical current created by the rising bubble into a horizontal current which limits the movement of the contaminant. (HydroTechnik Lübeck 2005).

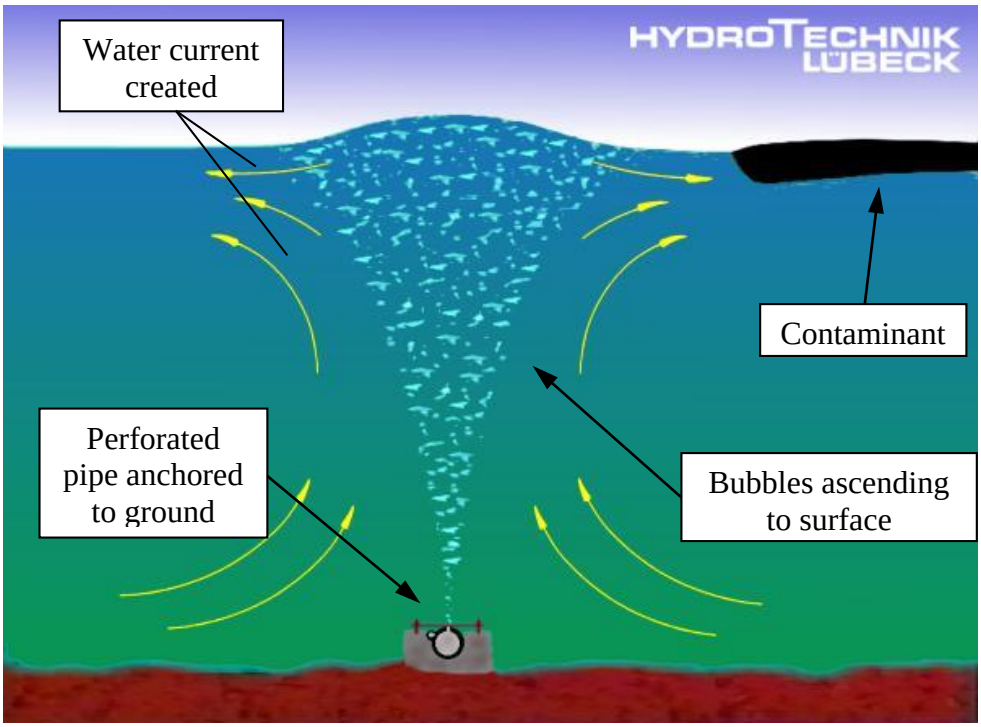

Figure 2.23 Bubble Curtain as a Pneumatic Barrier Diagram (Hydrotechnik Lübeck 2005).

3 Analysis

This analysis was three fold with the intent to use the results to form a step-by-step procedure to design a bubble screen system for the protection of waterborne infrastructure. The prediction of underwater blast characteristics was the first aspect analyzed. This was followed by the damage potential of the pressure wave and structure interaction. The final aspect, which relied on the results of the first two, was the attenuation performance of bubble screens.

3.1 Comparison of Underwater Blast Characteristics

The similitude equations for underwater blast characteristics presented in Swisdak (1978) and Cole (1948) form a fairly robust foundation on which to base underwater explosion predictions. Therefore, the equations presented in those studies were used as a comparison following the development of unique similitude equations for the specific data acquired for this analysis. Furthermore, the effect of charge depth was considered, and subsequently included, as an improvement over basic form presented by Swisdak (1978).

3.1.1 Measured Data versus Empirical Equations

While the coefficients for the similitude equations presented by Swisdak (1978) in Table 2.4 are generally accepted values, measured data from four other sources were compiled for this study, and analyzed to assess the validity of these coefficients. These studies were conducted at four different depths which presented an opportunity to determine how depth affects the magnitude of pressure wave characteristics. This analysis was limited to studies that used TNT charges, all of which used different weights, radial standoff distances from the charge, and depths. The charge type in the analysis was limited to TNT to avoid potential errors within the equivalency factors for other explosives. Table 3.1 is a summary of the test parameters for the data used in this analysis.

Table 3.1 Summary of Data Sources

Source	Charge Weight (kg)	Depth (m)	Radial Distance from Charge Range (m)
Coles 1946	34.50	12.19	1.52 – 30.48
	21.79	12.19	1.52 – 30.48
USACE 1961	3.63	2.743	1.22 – 6.48
Richmond 1973[1]	0.454	3.048	14.63 – 25.60
	0.227	3.048	30.48
Heathcote 1981	3.18	10.67	1.52 – 4.11

[1] It was determined near the completion of this study that the data obtained from Richmond (1973) was produced using Pentolite charges, not TNT. The error introduced by this mistake appears minimal, as general agreement with TNT data was already observed. The TNT equivalency factor for Pentolite is 1.04 as presented in Table 2.1, confirming similarity to TNT.

The data from these studies was tabulated and converted to metric units, and are included in Appendix B. The pressure wave characteristics measured in these tests were plotted against the scaled radial standoff distances to compare the trend of the data to the similitude coefficients published by Swisdak (1978). Figure 3.1 presents the plots for the peak pressure data. A linear regression of the data was performed that produced a power function representing the data, and yielded new similitude coefficients. To compare the accuracy of the equations presented by Swisdak (1978) to the equations developed from the data, the R^2 values for the equations versus the data were calculated.

The peak pressure data in Figure 3.1, demonstrated a consistent relationship between the peak pressure and scaled radial distance from the charge similar to Figure 2.13. The negative slope of the data trend indicated that peak pressure reduces as distance increases, and confirmed the general relationship presented in previous studies.

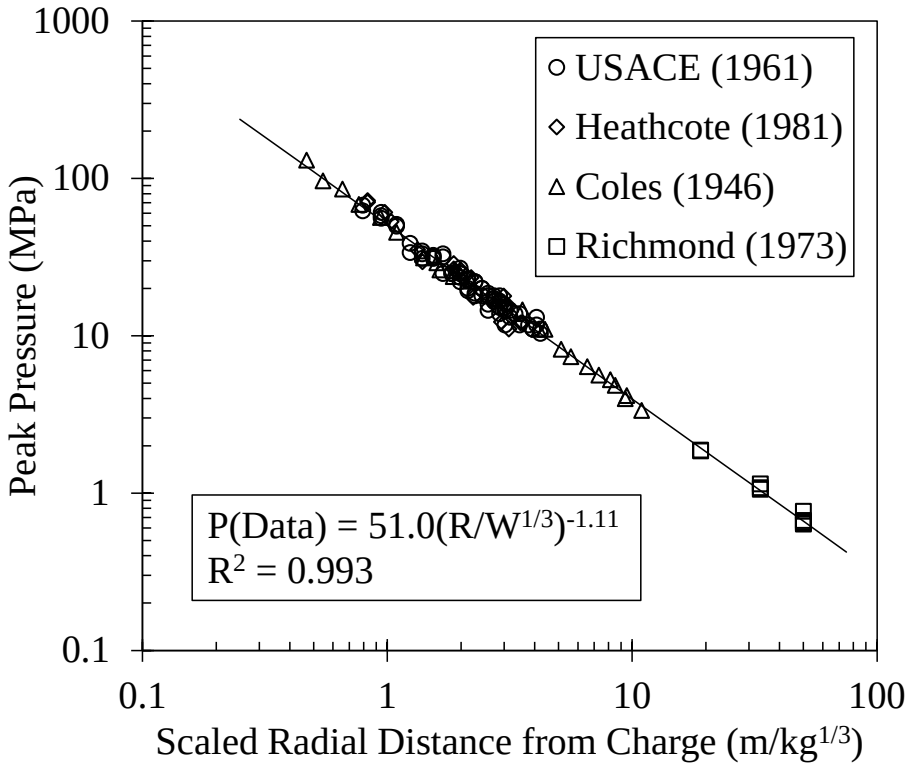

Figure 3.1 Measured Peak Pressure Data with Curve-Fitting Equation

The equation developed for the tabulated study data and the equation presented by Swisdak (1978), shown below, contains similar coefficients and high R^2 values. The slightly higher R^2 value for the new equation indicated that it provided an improved representation of this data over the previously published equation. However, this comparison also confirmed the relative accuracy of the equation presented by Swisdak (1978), even over a wide selection of data.

$$P_m(\text{Data}) = 51.0\left(\frac{R}{W^{1/3}}\right)^{-1.11} \qquad R^2 = 0.993 \tag{22}$$

$$P_m(\text{Swisdak 1978}) = 52.4\left(\frac{R}{W^{1/3}}\right)^{-1.13} \qquad R^2 = 0.986 \tag{23}$$

The scaled energy flux density data was plotted similarly to peak pressure, as seen in Figure 3.2. It also followed a negative slope but the rate of reduction was greater. As seen in Equation 2 in the previous section, energy flux is a function of pressure squared, which likely explains the higher rate of decay. The energy flux data maintained a relatively

consistent trend, but was visibly less grouped than the peak pressure data. Additionally, all the energy flux data presented by Richmond (1973) was clearly inconsistent with the other data. Richmond (1973) stated that the energy flux was calculated using a computer program, but failed to describe the time constant or other parameters used for the calculation, some variation or error was likely introduced in that process. Due to poor grouping and disagreement with other data, the data points from Richmond (1973) were excluded from the linear regression analysis and resulting equation.

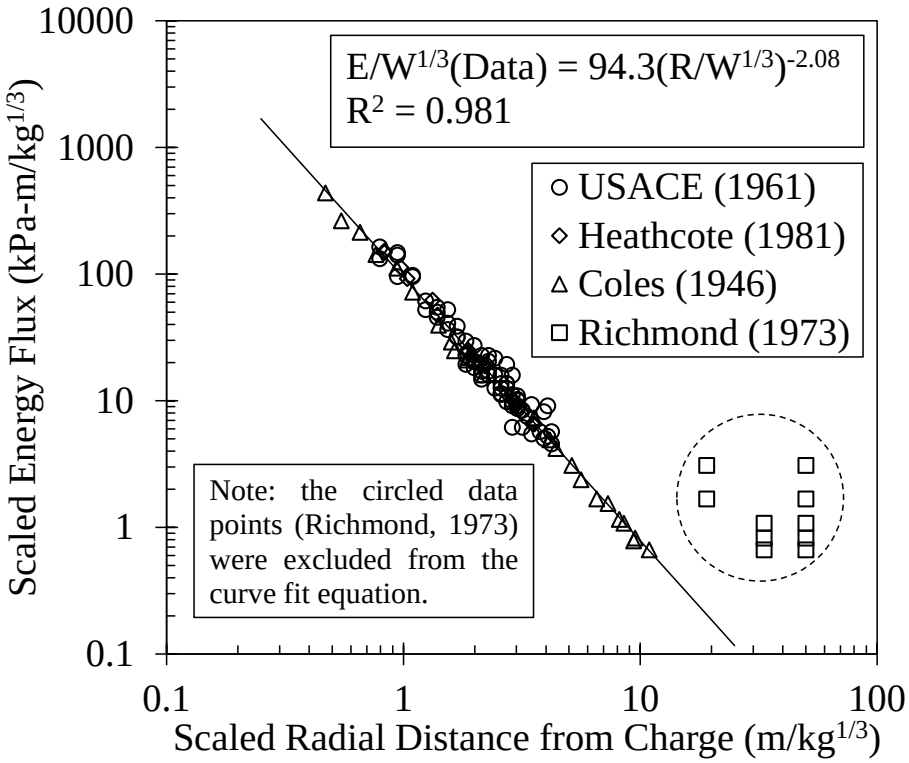

Figure 3.2 Measured Energy Flux Density with Curve-Fitting Equation

The equation developed for the tabulated study data, and the equation presented by Swisdak (1978), shown below, exhibited similar coefficients, particularly for the slope. The R^2 values for the equations demonstrated that the equations represent the data well, though the R^2 value for the new equation was notably higher, and was thus more representative. The fact the R^2 values for energy flux were lower than the respective values for the peak pressure equations, confirmed the larger spread observed in the data.

$$\frac{U}{W^{1/3}}(\text{Data}) = 94.3\left(\frac{R}{W^{1/3}}\right)^{-2.08} \qquad R^2 = 0.981 \qquad (24)$$

$$\frac{U}{W^{1/3}}(\text{Swisdak 1978}) = 84.4\left(\frac{R}{W^{1/3}}\right)^{-2.04} \qquad R^2 = 0.967 \qquad (25)$$

The empirical equations developed for the data were used for the remainder of the analysis, since they provide a better representation of the data than those presented by Swisdak (1978).

The impulse data corresponding to the presented peak pressure and energy flux density data was analyzed and a new equation was developed. However, because the effect of impulse is not being discussed in this report, the plot and equations are presented in Appendix A for reference.

3.1.2 Effect of Depth on Peak Pressure and Energy Flux

While the equations presented by Swisdak (1978) are used in other studies, they do not account for the effect of depth on pressure wave characteristics, however depth has been shown to influence peak pressures, thus this study accounted for depth. The measured peak pressure data was normalized by dividing it by the hydrostatic pressure, P_z, at the charge depth. This made the representation of peak pressure both dimensionless, and a function of depth, since $P_z = \gamma_w \cdot z$, where γ_w is the unit weight of water (9810 N/m^3), and z is the depth of the charge. The normalized peak pressure was then plotted against the scaled radial standoff distance, see Figure 3.3.

Figure 3.3 showed that the peak pressure data was delineated as a function of depth. This implied that the depth of explosion was significant to the peak pressures propagated through the water. The behavior of the normalized peak pressures was similar to the unaltered data in Figure 3.1, however the spread of the data was slightly increased as evidenced by generally lower R^2 values; the R^2 value for the data at 2.74m was 0.968, at 3.048m it was 0.979, at 10.67m it was 0.958, and at 12.19m it was 0.996.The data set with the greatest spread was for explosions at 10.67m, which was the only data set with varying depth of gauges, likely explaining this phenomenon.

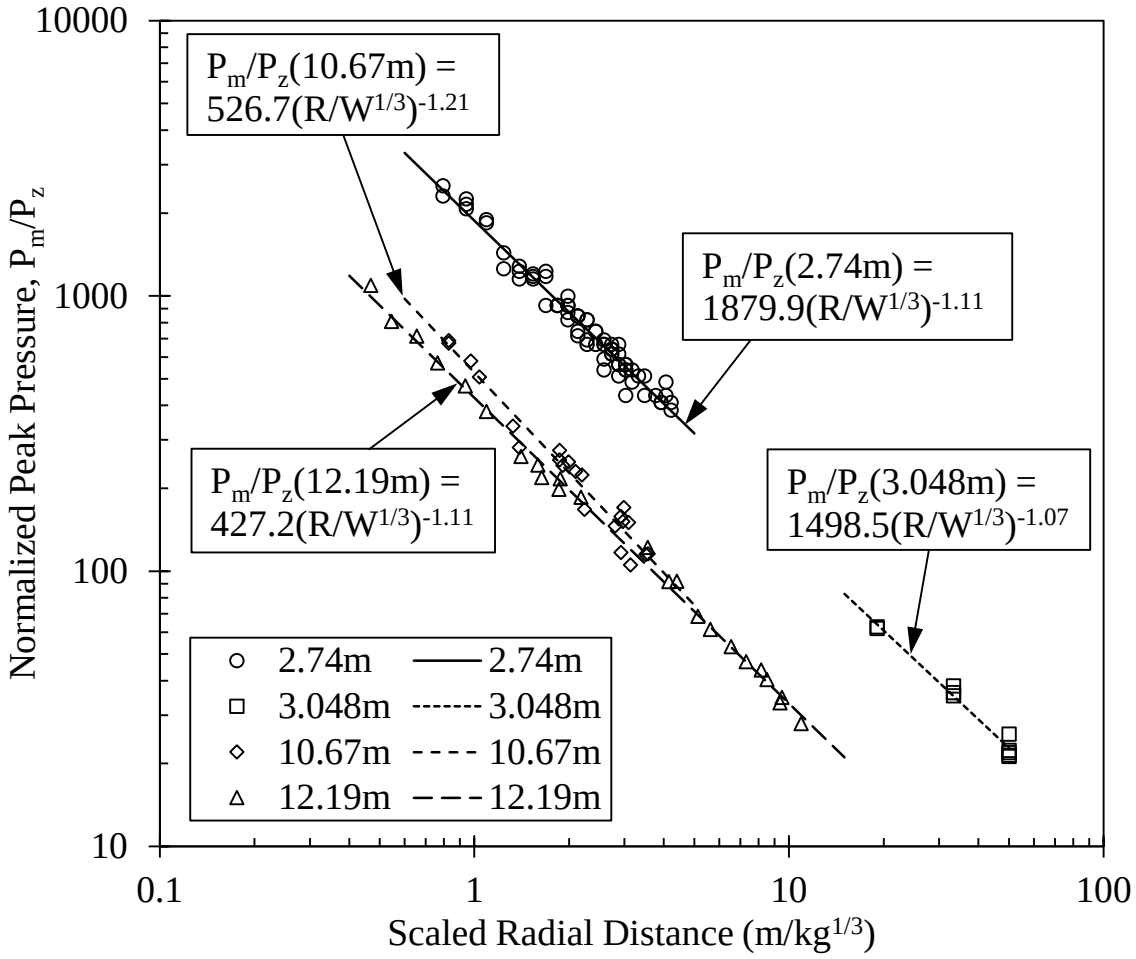

Figure 3.3 Effect of charge depth on peak pressure

Regression analyses performed for each of the data sets produced power functions of the following form,

$$\frac{P_m}{P_z} = A\left(\frac{R}{W^{1/3}}\right)^B \tag{26}$$

where coefficient A equals P_m / P_z when the scaled radial distance is unity, and B is the rate of pressure reduction; both were determined from the data plotted in Figure 3.3. The functions possess varying values for coefficient A, but approximately equal values for coefficient B. This indicated that A was heavily dependent on depth, because the similar powers do not explain the discrepancy of the data sets from depth. Subsequently, to develop an empirical equation for A, the values of A from each equation were plotted against the

respective charge depth, and a power function was fitted to the four data points, see Figure 3.4. The coefficient *B* represents the rate of decay, or slope, of the data. Pressure waves experience natural decay with time, and since *B* does not vary with depth, it was concluded that depth is not a significant factor of the rate of natural decay. Since the coefficient *B* showed little variation between data sets, it was approximated as -1.1. The resulting coefficients for Equation 26 are:

$$A = 4510.1(z)^{-0.927} \tag{27}$$

$$B = -1.1 \tag{28}$$

where *z* is the depth of the charge in meters.

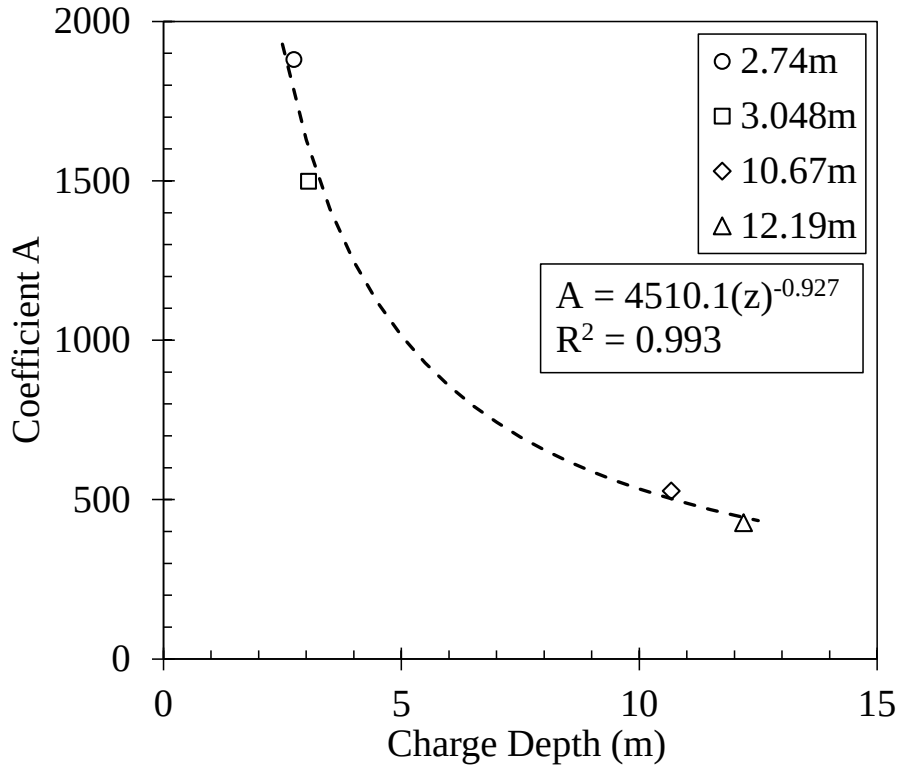

Figure 3.4 Equation for coefficient *A*

Due to the lack appropriate data to validate this modification, a fidelity assessment was performed to compare the measured data with the prediction determined by Equation 26, see Figure 3.5. A fidelity assessment indicates whether the equation developed for data

actually represents the data well. From this plot, it appeared that the approximation slightly over-estimated most of the actual measurements, but was generally a good fit.

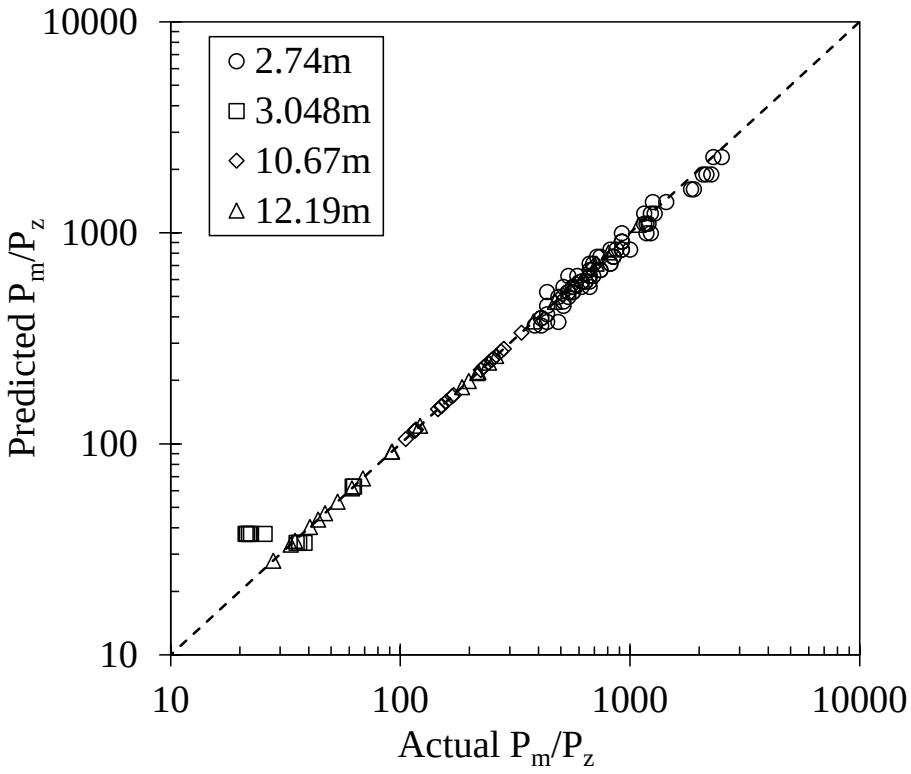

Figure 3.5 Fidelity assessment for predicted normalized peak pressure

A similar procedure was attempted for energy flux density, but the data did not correlate well with depth and thus was abandoned. This is likely due to the methods used by the different studies to calculate energy flux. For example, Coles et al. (1946) and USACE (1961) used a period of 6.7θ, while Heathcote (1981) used 1.0ms, and Richmond (1973) didn't specify and likely had additional errors mentioned previously. Therefore, for the data available for underwater TNT explosions, depth should not be considered in the level of energy flux density from the pressure wave without further study.

All the data used for this portion of the analysis was measured by gauges placed in the water at the same depth as the explosive charge, with the exception of the data with charge depth of 10.67m which used gauges at various depths (Heathcote 1981), so radial distance was used for the equations. The *B* coefficient for the 10.67m data was greater than the other, indicating a greater rate of natural decay. This may be due to the decreasing hydrostatic pressure and density of the water. Also, the charges were placed at

approximately the mid-depth of the water, with the exception of the charges placed at 3.048m which were in a total depth of 9.14m. This was considered acceptable since only the first and direct (unreflected), pressure wave was considered.

3.2 Damage Potential

The damage potential of underwater explosions presented in this analysis was determined based on several assumptions and simplifications regarding the nature of the loading, the strength of the materials, and the response of the structure. It is generally accepted, and often preferred, to simplify the response of dynamic systems, due in part to the intricate nature of a rigorous analysis, and in part to the sufficiently high level of accuracy typically attained. The development of an equivalent system is an approximate method commonly used to model a dynamic system as static with reasonable accuracy (Biggs 1964). The peak pressure was assumed to act as a quasi-static load applied normal to the structure, because the natural period of structural elements is typically less than the period of the pressure wave, which indicates quasi-static loading, and the pressure applied normally will have the greatest effect on the structure. The energy flux was conservatively assumed to be fully absorbed by the structure. Both load types were assumed to act dynamically for the purpose of DIFs, due to the rapid application and decay of the loads. The strength of materials and member response were analyzed without load factors but the use of DIFs was assumed to be applicable, as the DIFs model the increase in strength, rather than acting as a factor of safety. The structures, or elements of the structures, were assumed to act elastically, as single degree of freedom systems, with the exception of concrete in compression which was considered at ultimate strength. This permitted the demonstration of the general concepts of damage potential and required attenuation without becoming overly specific, as would be the case with plastic deformations and multiple degree of freedom elements.

3.2.1 Equivalent Systems

The equivalent systems presented by Biggs (1964) were briefly investigated in this study. Due to the necessary knowledge of a structures physical properties and the general nature of the design procedure developed herein, a DLF of 1.0 was used for simplicity. Values for

specific structures may be determined using Figure 2.9 and the procedure described by Biggs (1964).

3.2.2 Dynamic Increase Factor

The dynamic increase factors applied to the materials used in analysis were determined using the associated figures and equations presented in UFC 3-340-02 (2008). The original figures and equations were modified appropriately to convert from U.S. customary system units to metric unit system. Other national codes present different DIFs but were not referenced for this analysis (Cormie et al. 2009).

3.2.2.1 Dynamic Increase Factors for Reinforced Concrete

The DIFs for reinforced concrete pertain to the material strengths of concrete and reinforcing steel separately. The DIF for reinforcing steel were determined in this analysis, but the damage potential to concrete only considered the compressive strength of concrete.

A study by the U.S. Bureau of Reclamation was conducted to compare the static compressive strengths and dynamic compressive strengths of concrete in existing dams to determine the expected response to earthquakes (Mohorovic et al. 1999). Static and dynamic compressive and splitting tensile tests were conducted on concrete cores taken from ten dams. The dams tested included: Hoover, Elephant Butte, Folsom, Warm Springs, Roosevelt, and five others. This study considered strain rates of 10^{-6}-10^{-4}mm/mm/s to imply static loading, and 10^{-3}-10^{-2}mm/mm/s to imply dynamic loading representing earthquakes, but also stated strain rates of 10^{2}-10^{3} mm/mm/s for blast loading. It was determined that the lowest concrete compressive strength of the structures tested was only 14MPa, though some were more than twice that figure. A static compressive strength, f_c', of 20MPa was modeled in this analysis to represent the lower range of compressive strengths on these existing dams. While the strain rates representing dynamic loading in this study were much lower than those representing blast loading, the dynamic compression tests produced a dynamic to static strength ratio of 1.07, and the dynamic splitting tensile tests produced a ratio of 1.44, indicating a potential significant increase in dynamic strength over static strength. Based on the Figure 3.6, the higher strain rates for blast loading should produce even larger increases in dynamic strength of concrete. The strain rates for blast

loading presented in Mohorovic et al. (1999) are three to four orders of magnitude larger than those recommended in UFC 3-340-02 (2008), implying the recommended strain rates are significantly conservative.

Figure 3.6 shows the design curve for the DIF for the ultimate compressive strength of concrete. Based on strain rate, $\varepsilon' = 0.3mm/mm/\sec$, the DIF for concrete compressive strength is approximately 1.25. This factor is applied using the following equation, where f'_{dc} is the concrete dynamic compressive strength.

$$f'_{dc} = DIF \cdot f'_c \tag{29}$$

Using $f'_c = 20MPa$ and the DIF previously determined, the dynamic concrete compressive strength is:

$$f'_{dc} = 1.25 \cdot 20MPa = 25MPa$$

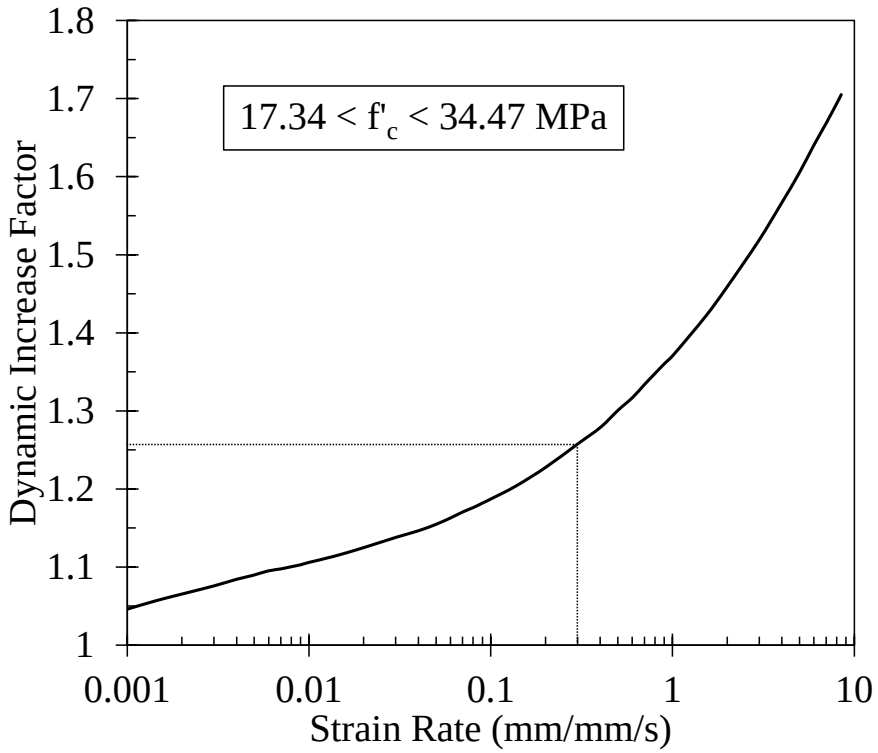

Figure 3.6 Design curve for DIF for ultimate compressive strength of concrete with 17.24 < f'_c < 34.47 MPa, (after UFC 3-340-02 2008)

The tensile and compressive strength of reinforcing steel is increased in dynamic loading according to Figure 3.7, which shows the DIF design curve for reinforcing steel. For Grade 60 reinforcement ($f_y = 60ksi = 414MPa$) and $\varepsilon' = 0.3mm/mm/\sec$, $DIF \approx 1.25$. Thus the dynamic yield strength can be determined given the following equation,

$$f_{dy} = DIF \cdot f_y \tag{30}$$

$$f_{dy} = 1.25 \cdot 414MPa = 518MPa$$

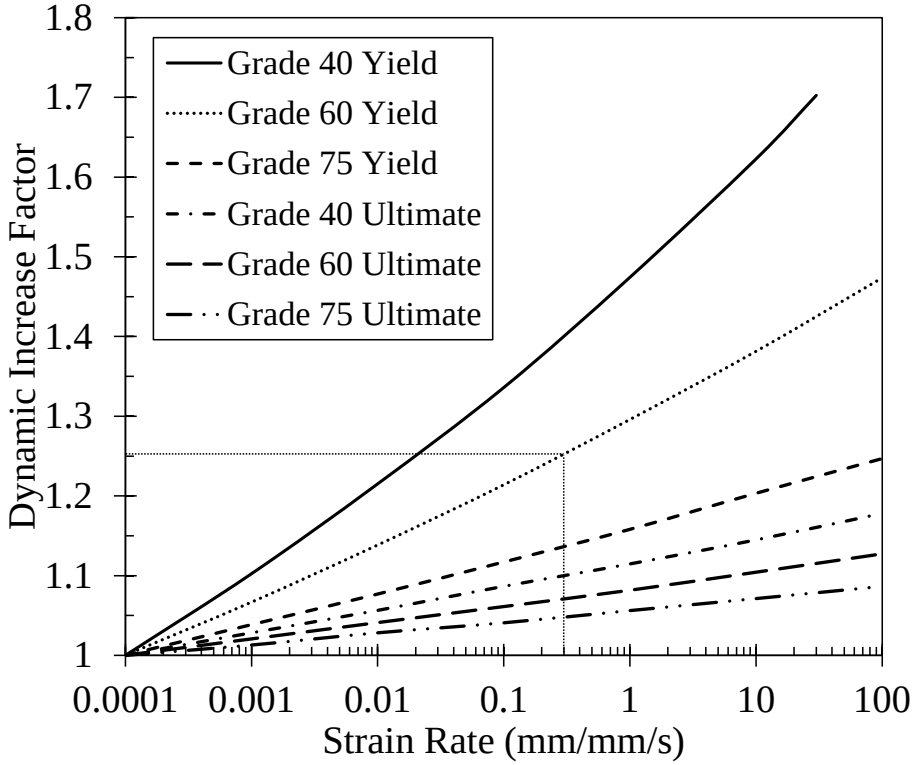

Figure 3.7 Design curves for DIFs for yield and ultimate stresses of ASTM A615 Grade 40, Grade 60, and Grade 75 reinforcing steel (After UFC 3-340-02 2008)

3.2.2.2 Dynamic Increase Factor for Structural Steel

The DIF design curves for ASTM A36 and ASTM A514 structural steels are shown in Figure 3.8. The strain rates used by UFC 3-340-02 (2008) for near design range is $\varepsilon' = 0.3mm/mm/\sec$ for bending, but is reduced to $\varepsilon' = 0.05mm/mm/\sec$ for tension and compression members. The equation for the dynamic yield stress of structural steel is slightly different than that used for reinforced concrete, as it also accounts for the higher

than specified yield stress generally found in steels with a specified minimum yield stress of *345MPa (50ksi*) or less (AISC 2010). The following equation is for the dynamic yield stress of structural steel in the elastic range.

$$f_{dy} = DIF \cdot a \cdot f_y \tag{31}$$

where DIF is determined from Figure 3.8, a is the average strength increase factor ($a = 1.1$ for $f_y \le 345MPa$, otherwise $a = 1.0$), and f_y is the static yield stress (after UFC 3-340-02 2008). Note: for A36 Steel, $f_y = 248MPa$, and for A514 Steel, $f_y = 621MPa$.

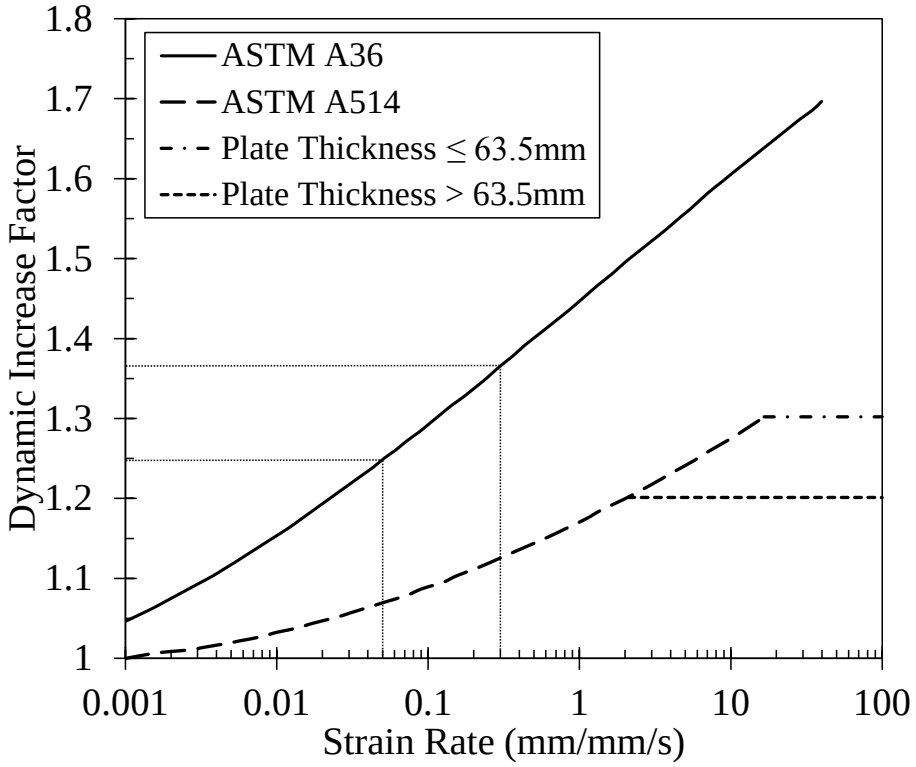

Figure 3.8 DIFs for yield stresses of ASTM A36 and A514 steels (After UFC 3-340-02 2008)

Using $\varepsilon' = 0.3mm/mm/\sec$ for bending, and ASTM A36 steel, the $DIF \approx 1.37$ and $a = 1.1$ (since $f_y = 248MPa \le 345MPa$). The resulting dynamic yield strength is $f_{dy,b} = 1.37 \cdot 1.1 \cdot 248MPa = 374MPa$.

For ASTM A36 steel tension and compression members with $\varepsilon' = 0.05mm/mm/\sec$, $DIF \approx 1.25$, and the dynamic strength is $f_{dy,tc} = 1.25 \cdot 1.1 \cdot 248MPa = 341MPa$.

Table 3.2 contains a summary of the DIFs and dynamic strengths the materials used in this analysis. The approximately equal DIF values for concrete, reinforcing steel, and structural steel in tension and compression is merely a coincidence based on the nominal design strengths selected.

Table 3.2 Summary of Dynamic Compressive and Yield Stresses for Analysis

Reinforced Concrete		
$f'_c = 20MPa$	$DIF \approx 1.25$	$f'_{dc} = 25MPa$
$f_y = 414MPa$	$DIF \approx 1.25$	$f_{dy} = 518MPa$
ASTM A36 Steel		
$f_y = 248MPa$	$DIF \approx 1.37,\ a = 1.1$	$f_{dy,b} = 374MPa$
	$DIF \approx 1.25,\ a = 1.1$	$f_{dy,tc} = 341MPa$

3.2.3 Damage Modes

3.2.3.1 Peak Pressure

In this analysis, using the simplified quasi-static loading scenario, it was assumed that the maximum allowable peak pressure was equal to either the dynamic compressive strength of concrete determined in Section 3.2.1.1, or to the maximum load permitted by the following equations for structural steel. The maximum allowable peak pressure was considered the highest pressure that will not cause damage.

Since the charge weight and the material strength are properties that cannot be controlled, the minimum radial distance was determined for concrete and structural steel in order to provide values that can aid in the protection of structures. For peak pressure, Equation 32 provides the minimum radial distance by setting P_m equal to f'_{dc} for concrete, and P_m as a function of $f_{dy,b}$ via Equation 33 for steel.

$$R = \left(\frac{P_m}{P_z A} \right)^{1/B} W^{1/3} (m) \tag{32}$$

For concrete the minimum radial distance was calculated for various charge weights and depths. The results were plotted in Figure 3.9 to graphically demonstrate the effect of weight and depth on the minimum radial distance. The maximum depth of explosion of the

data used to produce Equation 26 was 12.19m, however liberty was taken to increase the maximum depth used in Figure 3.9 to 30m to better show the potential effect of depth on peak pressures. For Figure 3.9 (A), the unscaled charge weight was used to give an easily understood representation. Figure 3.9 (B) was provided for scaled charge weight which is more convenient for data acquisition. The plots indicate that there was minimal increase in minimum radial distance with depth for small charges, with increasing disparity as charge weight increased. However with the range of depths given in the figure, the total difference in minimum radial distance for a 1000kg charge was approximately 3m, or a factor of 1.167, which seems minimal for the size of blast produced by that charge.

Also, it was apparent that the proportion with which the minimum radial distance increased due to increasing depth was inversely related, and thus the effect of increasing charge depth becomes negligible at some depth. However, as previously stated, Equation 26 was developed for data at a maximum depth of approximately 12m, and further study should be completed for depths beyond this range.

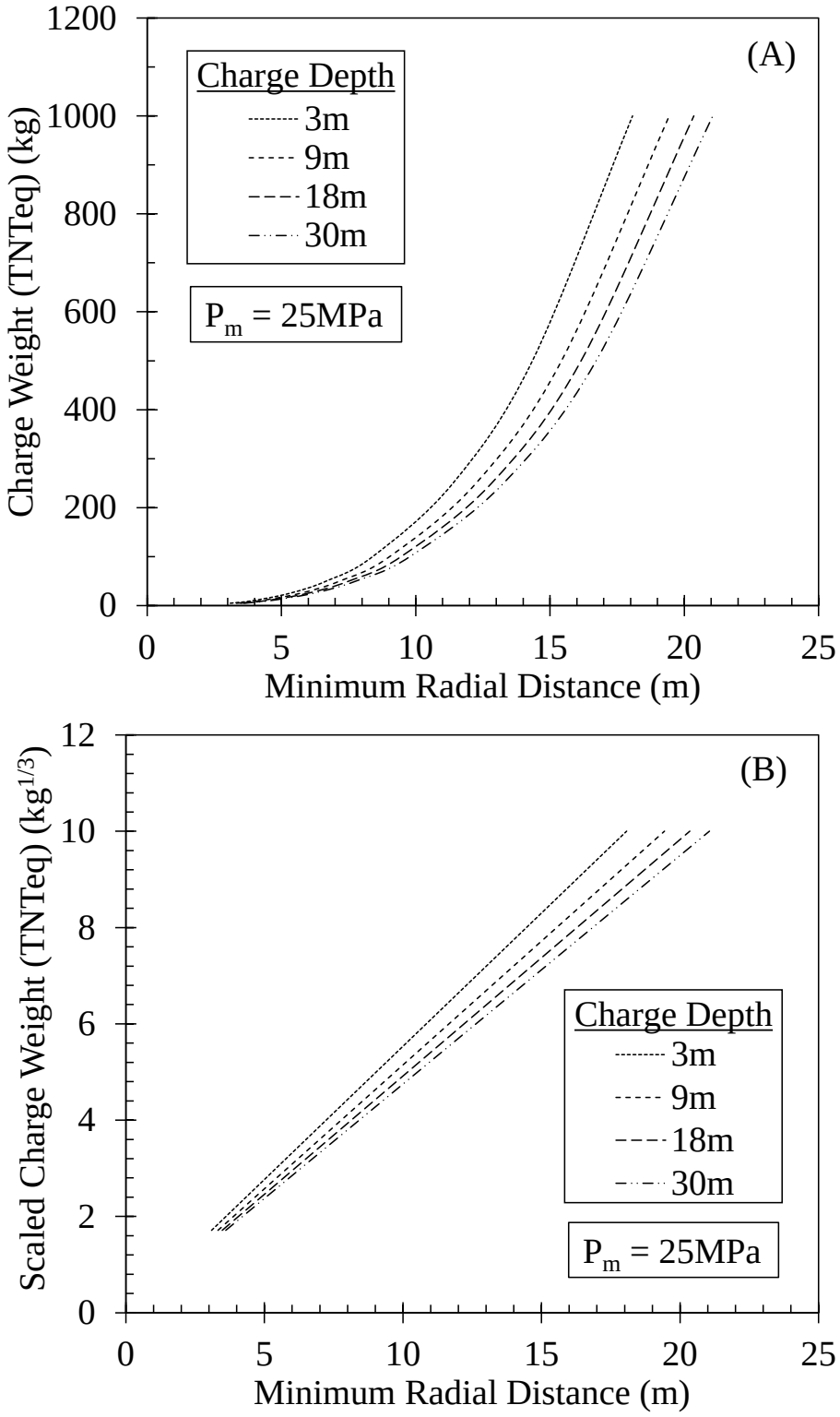

Figure 3.9 (A) Minimum Radial standoff Distance versus Charge Weight for Various Depths, (B) Minimum Scaled Radial Distance versus Charge Weight for Various Depths. Based on P_m.

For structural steel, Equation 33 was developed based on a fixed-fixed rectangular member using elastic theory to determine the effect of peak pressure in bending,

$$P_{m,all} = \frac{2 f_{dy,b} h^2}{l^2} \tag{33}$$

where, $f_{dy,b}$ is the dynamic yield stress in bending, h is the member depth, and l is the length of the member. Equation 33 assumes the member or structure acts as a single degree of freedom system and only considers the allowable pressure for bending. The derivation of Equation 33 is shown in Appendix A. Various charge weights and aspect ratios (h^2/l^2) were used with Equation 33 to calculate respective allowable peak pressures. The resulting peak pressures were then used in Equation 32 to determine the minimum radial distances, which were subsequently plotted as seen in Figure 3.10. Figure 3.10 (A) depicts the minimum radial distance versus unscaled charge weight for easier comprehension, while scaled charge weights were used in Figure 3.10 (B) to aid data acquisition. From Figure 3.10, it is evident that the thinner and longer a member is, the greater the radial distance must be to prevent damage. An increase of charge weight, and thus peak pressure, shows a more dramatic increase of the minimum radial distance for smaller aspect ratios. For example, with a 200kg charge, the minimum radial distance for a member with $h^2/l^2 = 0.05$ is approximately 10m, however for a member with $h^2/l^2 = 0.003$ the minimum radial distance is about 170m. However, for the former member, the total range of minimum radial distances is about 2-15m. This indicates that member stiffness, which is a function of the aspect ratio, versus peak pressure, has greater influence on the potential to sustain damage.

Figure 3.11 depicts the results of a sensitivity analysis for Equation 33. In (A) the aspect ratio was held constant as $h^2/l^2 = 0.000225$, and in (B) the dynamic yield strength was held constant as $f_{dy,b} = 374MPa$. The purpose of this analysis was to compare the sensitivity of Equation 31 to each variable, considering h^2/l^2 as a single variable. From the figure it is apparent that $P_{m,all}$ is more sensitive to h^2/l^2 as the rate of change is more significant in Figure 3.11(B). Furthmore, the range of $f_{dy,b}$ for ASTM A36 steel is roughly

250-400MPa so to increase $P_{m,all}$ without changing the aspect ratio would require choosing a higher strength steel, for less impact than increasing the aspect ratio.

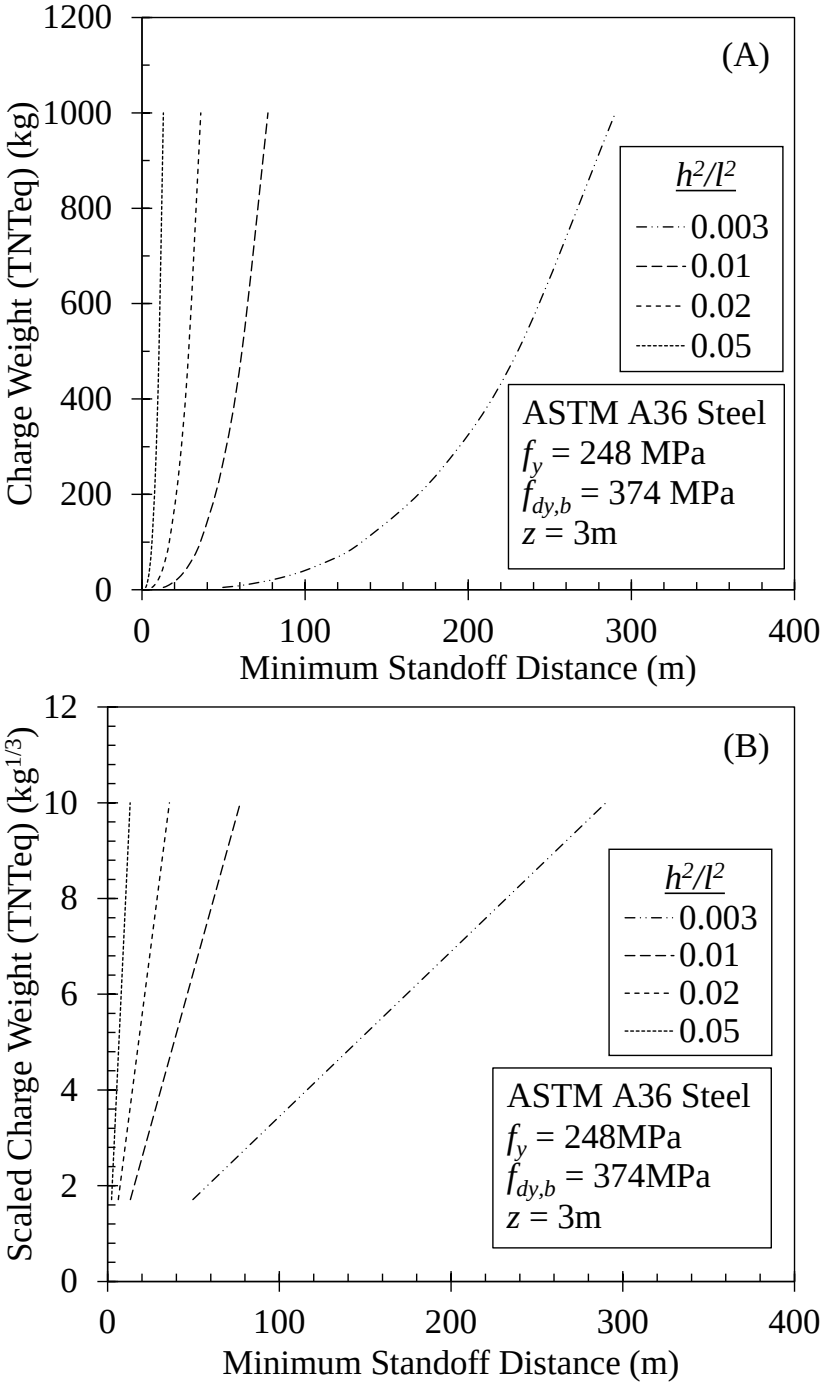

Figure 3.10 (A) Minimum Radial standoff Distances versus Charge Weight for Various Values of h^2/l^2, (B) Minimum Radial standoff Distances versus Scaled Charge Weight for Various Values of h^2/l^2.

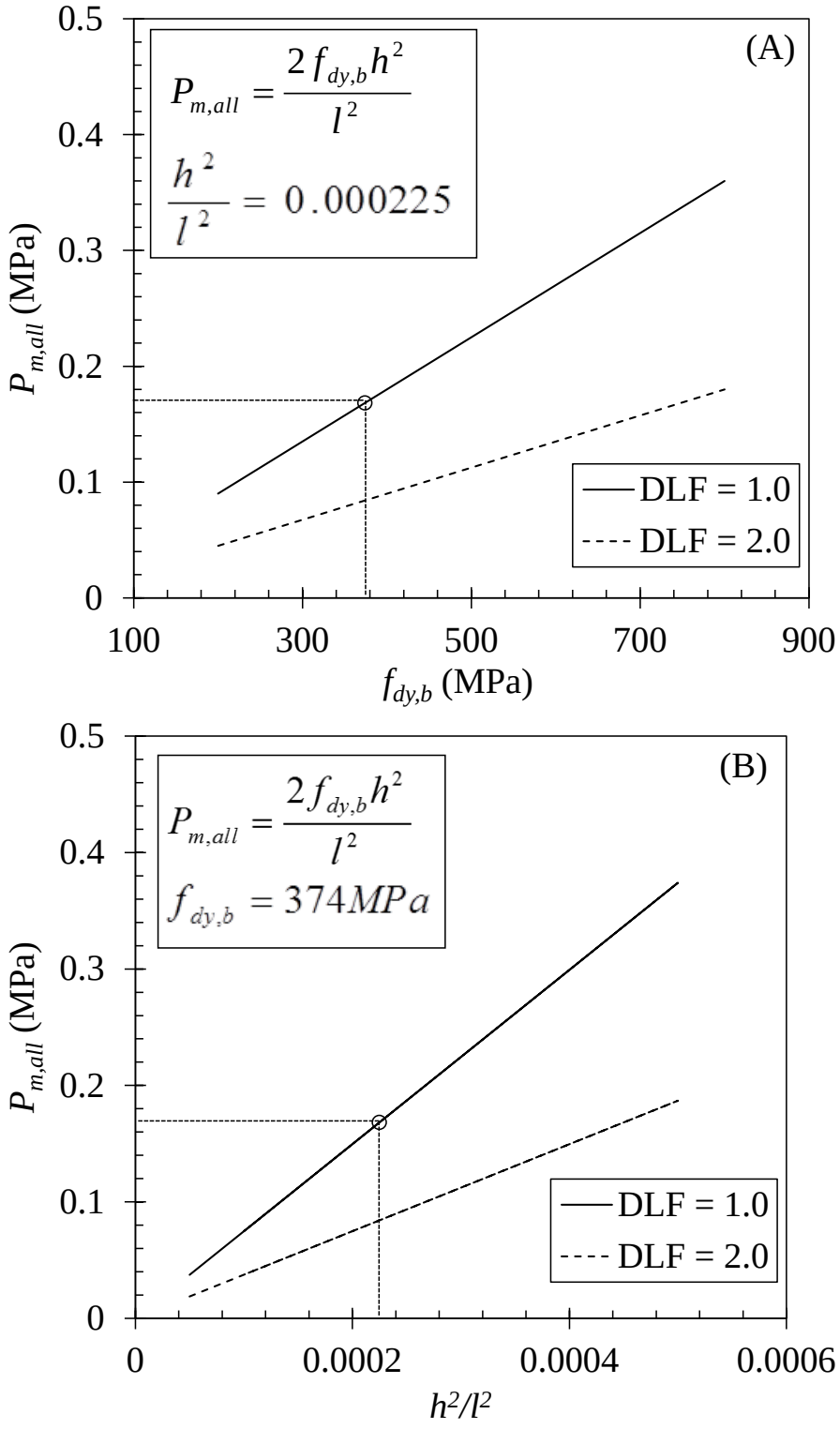

Figure 3.11 Sensitivity Analysis for Equation 33. (A) h^2/l^2 made constant; (B) $f_{dy,b}$ made constant.

Figure 3.11 also demonstrates the effect of the DLF on the allowable peak pressure. A DLF value of 1.0 was used for this study, but the use of DLF = 2.0 would dramatically reduce the allowable peak pressure. This would be the case for structures with short natural periods.

3.2.3.2 Energy Flux

In order to demonstrate the damage potential of energy flux in this analysis, the analysis considers only elastic deformation acceptable. The following equation was derived for an element with a rectangular cross-section, fixed-fixed end conditions, a single degree of freedom, a uniformly distributed load, responding through bending. The derivation is shown in Appendix A, and can be modified for other member cross-sections or end conditions.

$$U_{all} = \frac{2 f_{dy,b}{}^{2} \cdot I \cdot l}{5bh^{2}E \cdot l'} \tag{34}$$

where U_{SE} is the strain energy required to develop within the member to counteract the kinetic energy from the pressure wave, $f_{dy,b}$ is the dynamic yield stress in bending, I is the moment of inertia of the member, b is the member height or width, h is the member depth, E is the modulus of elasticity, l is the member length, and l' is unit length ($1m$). The moment of inertia for a rectangular member ($I = bh^3/12$) was used in Equation 32 to provide an example of damage potential, and to create Equation 35,

$$U_{SE} = U_{all} = \frac{f_{dy,b}^{2} h \cdot l}{30E \cdot l'} \tag{35}$$

Setting $U_{SE} = U_{all}$ implies that all energy flux is converted into elastic strain energy within the structure. This approximation further implies that the strain energy is equally distributed, such that there are no localized plastic deformations, and it implies that no energy flux is reflected by the structure. Equation 35 was substituted into Equation 24 to determine the minimum radial distance for various charge weights and member properties.

$$\frac{U_{SE}}{W^{1/3}} = 94.3\left(\frac{R}{W^{1/3}}\right)^{-2.08} \tag{36}$$

which is rewritten as,

$$R = W^{1/3}\left[\frac{\frac{U_{SE}}{W^{1/3}}}{94.3}\right]^{\frac{1}{-2.08}} \tag{37}$$

Equation 37 was used to plot minimum radial distances for ASTM A36 steel for various member depths, and for $E = 200GPa$, see Figure 3.12. Unscaled charge weight was used for Figure 3.12(A) to provide easy comprehension, and scaled charge weight was used for Figure 3.12(B) for ready data acquisition. This figure indicated that minimum radial distance increased with increasing charge weight at a decreasing rate which eventually became approximately linear. The charge weight at which linearization occurred was greater for smaller member depths. Furthermore, the minimum radial distance increased exponentially as member depth decreased. For member depths of 0.25-1.00m the depth increments were equal but the minimum radial distance was disproportionately larger the smaller the depth. This indicated that member stiffness was also the most significant property for damage resistance to energy flux.

Figure 3.13 depicts a sensitivity analysis for Equation 35. For the two plots presented, the member thickness was held constant as $h = 0.05m$ in (A), and the dynamic yield stress was held constant as $f_{dy,b} = 374MPa$ in (B). Figure 3.13(A) shows the exponential effect of $f_{dy,b}$ on U_{SE}. However, since $f_{dy,b} = 374MPa$ is in the upper extreme of $f_{dy,b}$, a higher strength steel would be required to significantly increase U_{SE} without changing the member thickness. A linear increase in U_{SE} for increasing *h* was seen in Figure 3.13(B). By inspection, increasing *h* has more influence on U_{SE} than $f_{dy,b}$ for lower strength steels, while increasing $f_{dy,b}$ has more influence than *h* for higher strength steels. The significance of determining that adjustment in $f_{dy,b}$ may be more effective than increase thickness, is that it may prompt a more precise determination of DIFs, and specifically the strain-rates used to determine DIFs. The recommended strain rates presented in UFC 3-340-02 (2008)

were noted to be conservative, thus calculating more exact strain rates for the member in question, may increase the DIF, and subsequently increase $f_{dy,b}$ and U_{SE}.

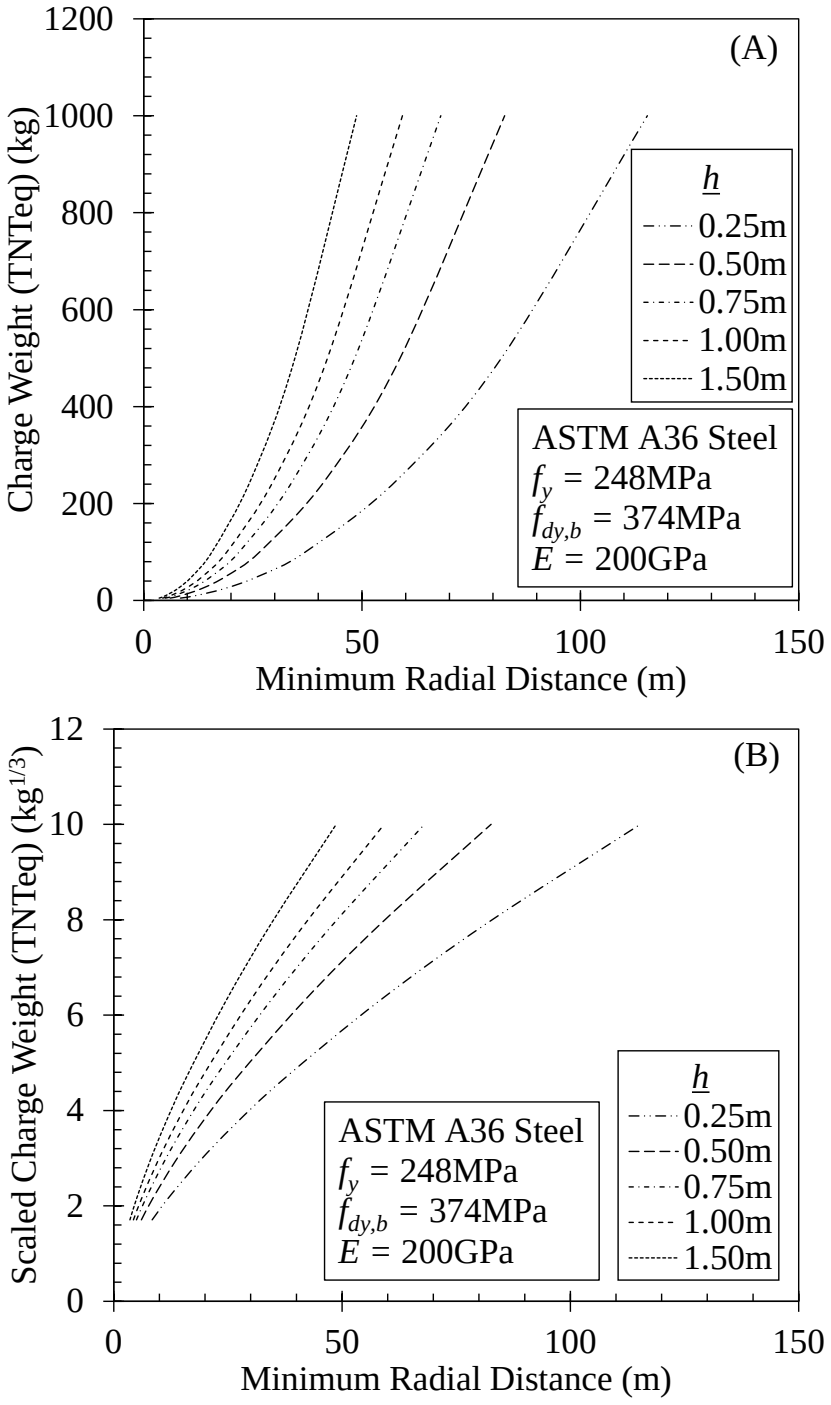

Figure 3.12 (A) Minimum Radial Distance versus Charge Weight for Various Member Depths, (B) Minimum Radial Distance versus Scaled Charge Weight for Various Member Depths.

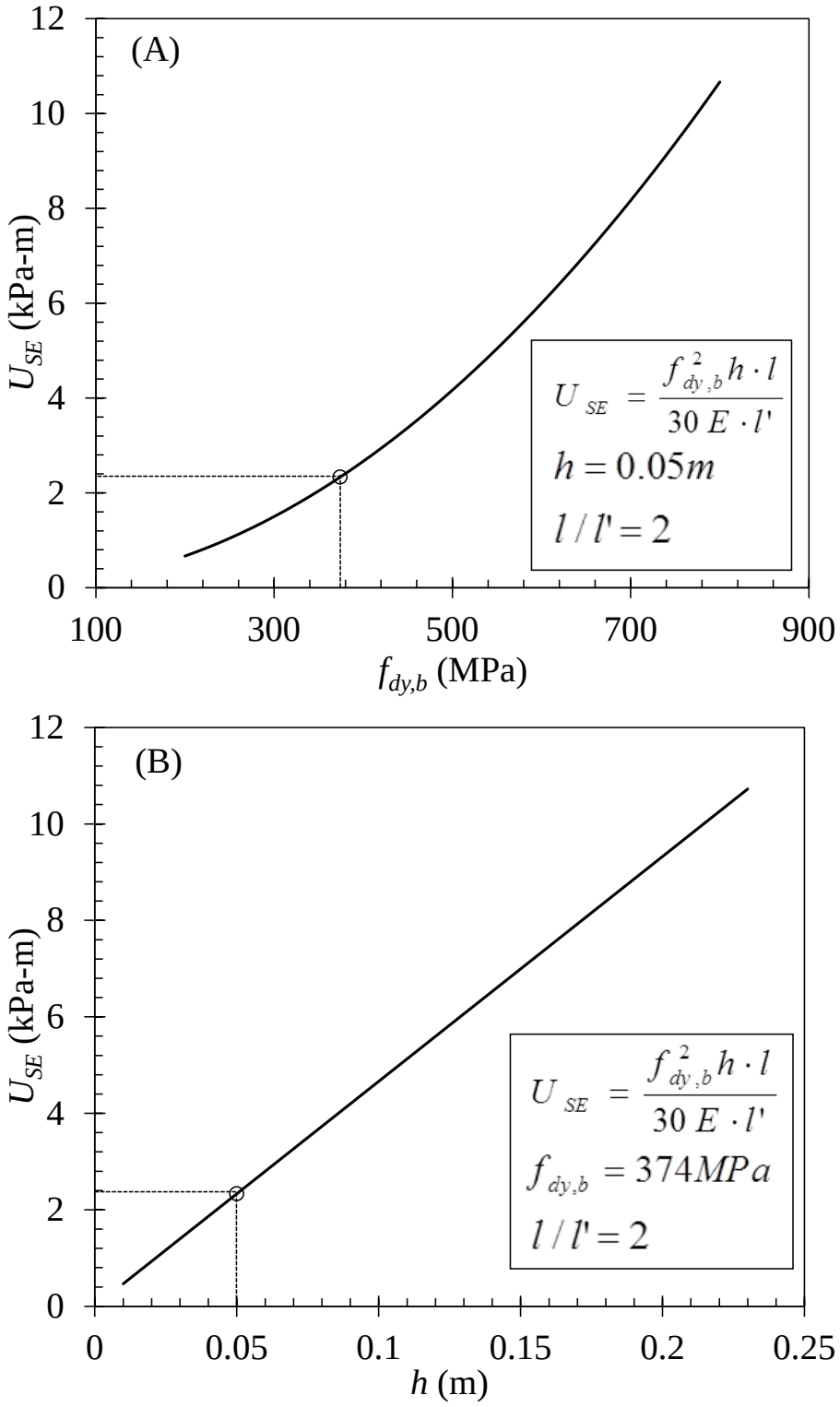

Figure 3.13 Sensitivity Analysis for Equation 35. (A) h made constant; (B) $f_{dy,b}$ made constant.

3.3 Bubble Screen Performance

The data from USACE (1961) was analyzed to determine the effect of airflow from the bubble curtain and gauge depth on pressure wave pressure and energy flux reduction. One of the primary benefits of this study was that it provided a large number of data points from which an analysis could be performed. To simplify the analysis, only the data with a radial standoff distance of 1.83m was utilized. The concession of limiting distance was deemed acceptable because the primary interest of this analysis was the attenuation of peak pressure and energy flux regardless of radial distance to the screen. From these data, the points deemed most appropriate to assess the protection provided to structures were the points immediately behind the bubble screen, as it was assumed that bubble screens will generally be located adjacent to the structure being protected. The average pressure and scaled energy flux measurements from these gauges (at each depth) were normalized over the pressure and scaled energy flux measurements for the same gauges in the free-water condition, to determine the attenuation ratio, see Equation 36. Additionally, the pressure wave impulse measurements from this study agreed with data from Rude and Lee (2007) and Hempen (1993b), which demonstrated bubble screens may not significantly decrease, and sometimes increase, pressure wave impulse. Therefore, impulse was not included in the analysis.

$$\alpha(P) = \frac{P_{m,r}}{P_{m,fw}},\ \alpha(U) = \frac{U_r}{U_{fw}} \tag{38}$$

where α is attenuation, subscripts r and fw represent the reduced and free-water peak pressures or scaled energy flux, respectively. The attenuation was plotted versus the airflow, A_f, for each gauge depth, refer to Figure 3.14.

The attenuation equations presented in USACE (1961), and previously in Section 2.4.4.1, were simplified for the conditions present in the study and multiplied by a coefficient, β_i, to account for gauge depth.

$$A_f\left(P_m\right) = 0.0467\left(v \cdot 10^5\right)\left[\left(\frac{P_{m,r}}{P_{m,fw}}\right)^{-1} - 1\right]\beta_P \tag{39}$$

$$A_f(U) = 0.0233\left(v \cdot 10^5\right)\left[\left(\frac{U_r}{U_{fw}}\right)^{-1} - 1\right]\beta_U \tag{40}$$

where, v is the kinematic viscosity of water in m^2/s, the standoff distance between the charge and front of the bubble screen was made constant at 1.83m, and air content and screen thickness were combined to form the airflow term, A_f.

The β_i coefficients were optimized through an iterative process to determine the appropriate value at each gauge depth to best match the data presented in USACE (1961), defined by highest respective R^2 value, see Figure 3.14(A) for peak pressure and Figure 3.14(B) for energy flux. Table 3.3 displays the gage depths, the depth ratios based on the charge depth of 2.74m, the respective β_i coefficients, and the R^2 values for Equation 39 and Equation 40 compared to the data, as seen in Figure 3.14.

Table 3.3 Depth Ratios used in Corrected Attenuation Equations with R^2 Values

Gauge Depth, z_g (m)	Depth Ratio, z_g/z	R^2 (Equation 39)	R^2 (Equation 40)	β_P	β_U
0.076m	0.028	0.947	0.942	0.13	0.040
1.37m	0.5	1.000	0.997	0.54	0.31
2.74m	1.0	0.922	0.980	0.99	1.16

In the plots within Figure 3.14, the equation matches the data well until it reaches an airflow of $0.00039 m^3/s/m$, which acts as the limit of minimum airflow for attenuation. As the limit is approached, the attenuation ratio represented by the data rapidly approaches unity, or negligible attenuation, especially for peak pressure. Therefore, for airflows less than this limit, attenuation is assumed to be negligible. In Figure 3.14(B), attenuation ratios at this limit for the gauge depth of 0.076m is still relatively high, however, the equation fails to represent the data at the limit, confirming this limit for the equations.

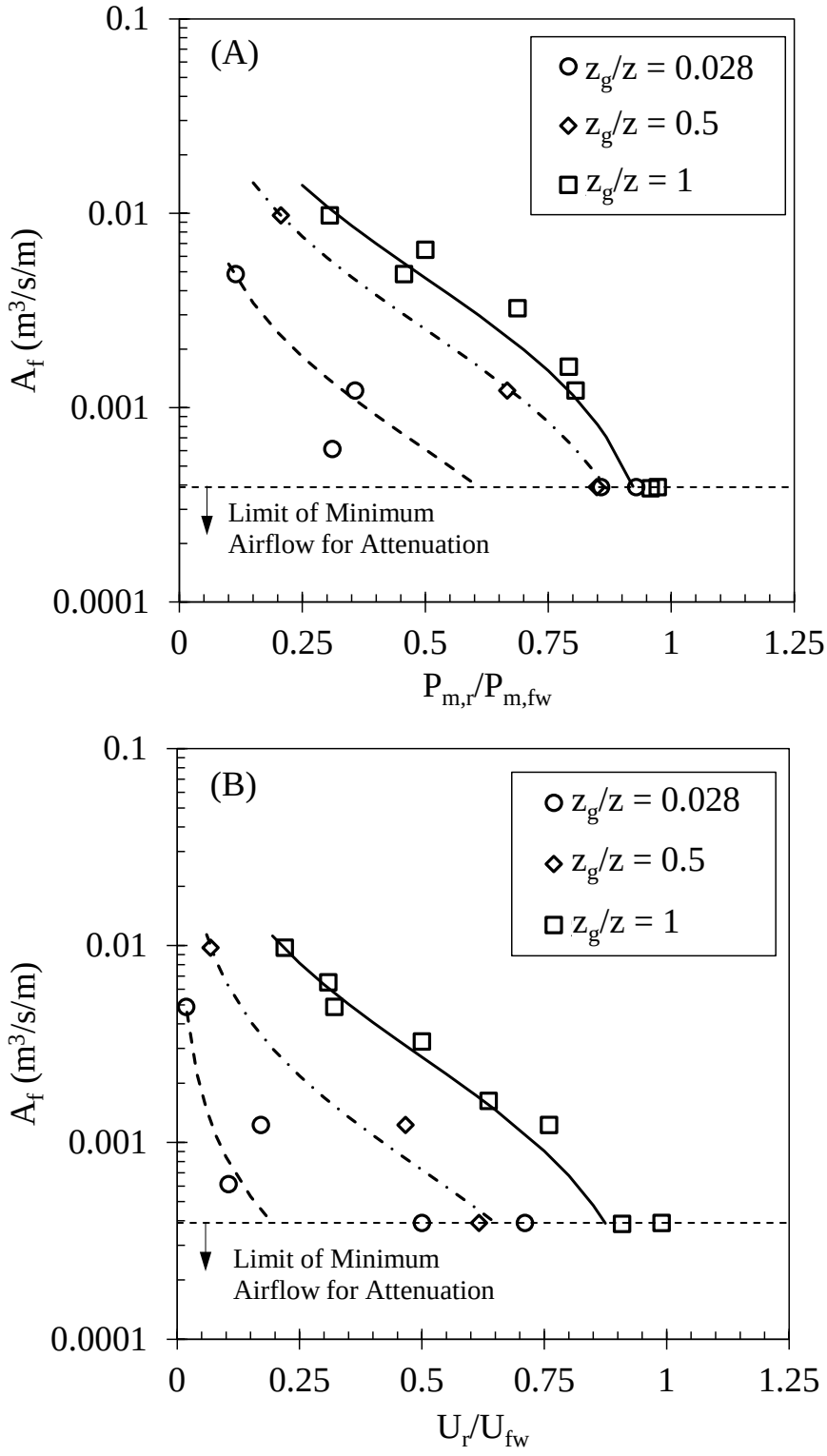

Figure 3.14 (A) Peak Pressure Attenuation versus Airflow for Various Gauge Depths; (B) Energy Flux Attenuation versus Airflow for Various Gauge Depths.

The β_i coefficients for each gauge depth, were determined for peak pressure and energy flux, see Table 3.3. These values were plotted against the normalized gauge depth, z_g / z, to develop general equations with respect to depth, see Figure 3.15.

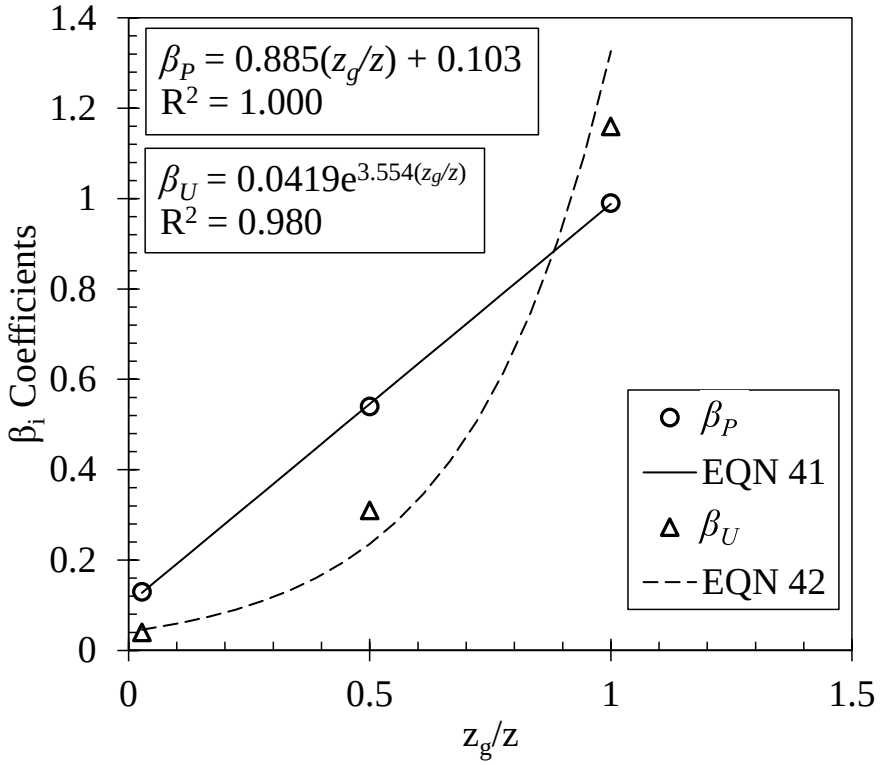

Figure 3.15 β_i Coefficients for Attenuation Relationships.

From Figure 3.15, a linear function was developed for β_P, see Equation 41, and an exponential function was developed for β_U, see Equation 42. The results of these equations provides values for at intermediate gauge depths.

$$\beta_P = 0.885\left(\frac{z_g}{z}\right) + 0.103 \tag{41}$$

$$\beta_U = 0.0419 \cdot e^{\left[3.455\left(\frac{z_g}{z}\right)\right]} \tag{42}$$

The data in Figure 3.14 indicated that there was greater attenuation at the shallower depths. However, due to the geometry of the test, the pressure wave propagated at an angle from perpendicular, which increased the total distance the pressure wave travelled through the

bubble screen. Thus, while part of the increase in attenuation was likely due to increasing bubble radius, the increased distance through the bubble screen effectively increased the airflow as well.

3.3.1 Air Content vs. Attenuation

In the study by Domenico (1982a), the acoustic velocity was determined to be a factor in attenuation. Furthermore, acoustic velocity is a function of the compressibility and density of the water-air mixture. The relatively small volume of air in a bubble screen minimally reduces the density of the mixture, though compressibility changes significantly.

In the study performed by the USACE (1961), the performance of bubble screens with varying air contents and thicknesses, was investigated to determine the effects of air content and screen thickness. Furthermore, the proportions of each were planned such that the air flow (the product of air content and screen thickness) was approximately equal for different screen thickness. Table 2.6 previously presented in Chapter 2, lists the different screen thickness, the air content supplied, and the air flow produced.

The results of the USACE (1961) study determined that screen thickness is significant to the rate of attenuation when the air content (airflow per unit area, $m^3/sec/m^2$) was equal for each screen thickness. However, it also determined that when the airflow per unit length ($m^3/sec/m$) of bubble screen was made equal regardless of screen thickness, the variation in the rate of attenuation was minimal. Since airflow is primarily a factor of the compressor at the surface, there is not a substantial benefit to increasing the screen thickness.

3.3.2 Effect of Depth on Bubble Screen Performance

One of the primary in-situ factors related to the performance of a bubble screen is the depth of water at the location the bubble screen was contacted by the pressure wave. Geometrically speaking, the greater the difference between the charge depth and depth of pressure wave contact, or target depth, the greater the distance the pressure wave will travel, both through the water and then through the bubble screen. Furthermore, as the air bubbles rise, the hydrostatic pressure decreases causing the volume of the bubbles to increase. As discussed previously in Section 2.4.2.1, resonant frequency of the bubble, which is a function of the bubble radius, may significantly affect the attenuating properties

of the bubble screen. It was concluded that bubbles with radius, $r \leq 3mm$, are most likely to provide the expected pressure wave attenuation. However, because bubbles increase in size as they ascend to the surface, it is necessary to ensure the radius does not increase beyond the maximum intended radius during the ascent.

The increase in bubble radius and fractional air content can be determined through the Ideal Gas Law, shown below,

$$P_1 \cdot V_1 = P_2 \cdot V_2 \tag{43}$$

$$V_2 = \frac{P_1 \cdot V_1}{P_2} \tag{44}$$

$$P_i = \gamma_w (z_o + z_i) \tag{45}$$

$$V_i = \frac{4}{3}\pi \cdot r_i^3 \tag{46}$$

$$\frac{V_2}{V_1} = \frac{z_o + z_1}{z_o + z_2} \tag{47}$$

where P is hydrostatic pressure, V is air (or bubble) volume, z_o is the depth equivalent to the piezometric head of ambient pressure, and subscripts 1 and 2 denote the depths, pressures, and bubble volumes at 1) the bubble screen manifold depth and 2) the depth in question respectively.

The change in bubble screen airflow due to change in bubble radius can be determined with Equation 48,

$$A_{f_2} = A_{f_1} \cdot \frac{V_2}{V_1} \cdot \frac{P_1}{P_2} \tag{48}$$

Combining and reducing Equation 46 and Equation 47 produces an equation to determine the change in bubble radius with depth,

$$\frac{r_2}{r_1} = \left(\frac{z_o + z_1}{z_o + z_2} \right)^{1/3} = \left(\frac{V_2}{V_1} \right)^{1/3} \tag{49}$$

$$r_2 = r_1 \cdot \left(\frac{z_o + z_1}{z_o + z_2} \right)^{1/3} \tag{50}$$

Using Equation 48 and Equation 50, and using the bubble screen data presented in USACE (1961) as an example, the approximate increase in airflow and bubble radius can be determined. The average bubble radius was approximately 3mm, the depth of the manifold was 5.49m, the assumed z_o is 10.34m. Assuming the bubbles all maintain terminal velocity at these points (Ditmars and Cederwall 1974), and for an initial airflow of 0.00975m^3/s/m, The approximate change in airflow (similar to fractional air content) and bubble radius at mid-depth is as follows:

$$\frac{A_{f,2.74m}}{A_{f,5.49m}} = \frac{10.34m + 5.49m}{10.34m + 2.74m} = 1.21$$

$$A_{f,2.74m} = 1.21 \cdot 0.00975 \frac{\frac{m^3}{s}}{m} = 0.0118 \frac{\frac{m^3}{s}}{m}$$

$$\frac{r_{2.74m}}{r_{5.49m}} = (1.21)^{1/3} = 1.07$$

$$r_{2.74m} = 1.07 \cdot 3mm = 3.21mm$$

Table 3.4 provides a summary of the predicted increases in airflow and bubble radius for the three gauge depths used in USACE (1961) and the manifold depth.

Table 3.4 Summary of Bubble Screen Airflow and Bubble Radius with Depth

Depth (m)	$\frac{A_{f2}}{A_{f1}}$	A_{f2} (m^3/s/m)	$\frac{r_2}{r_1}$	r_2 (mm)
5.49	1.00	0.03	1.00	3.00
2.74	1.21	0.0363	1.07	3.21
1.37	1.35	0.0405	1.11	3.33
0.076	1.52	0.0456	1.15	3.45

While the bubble radius was determined to increase above 3mm at shallower depths, Figure 3.14 indicates the attenuation rates increase at shallower depths. This is explained as a function of increased airflow due to increasing bubble radius, and because the pressure

waves must travel further through the bubble screen to reach the shallower gauges, effectively increasing the airflow at those locations.

In the USACE (1961) study, it was determined that the bubble screen profile changed with depth. By approximate measurements taken during the experiment, it was determined that that the width of the bubble screen initially decreased above the manifold, and then increased as it approached the surface, see Figure 3.16.

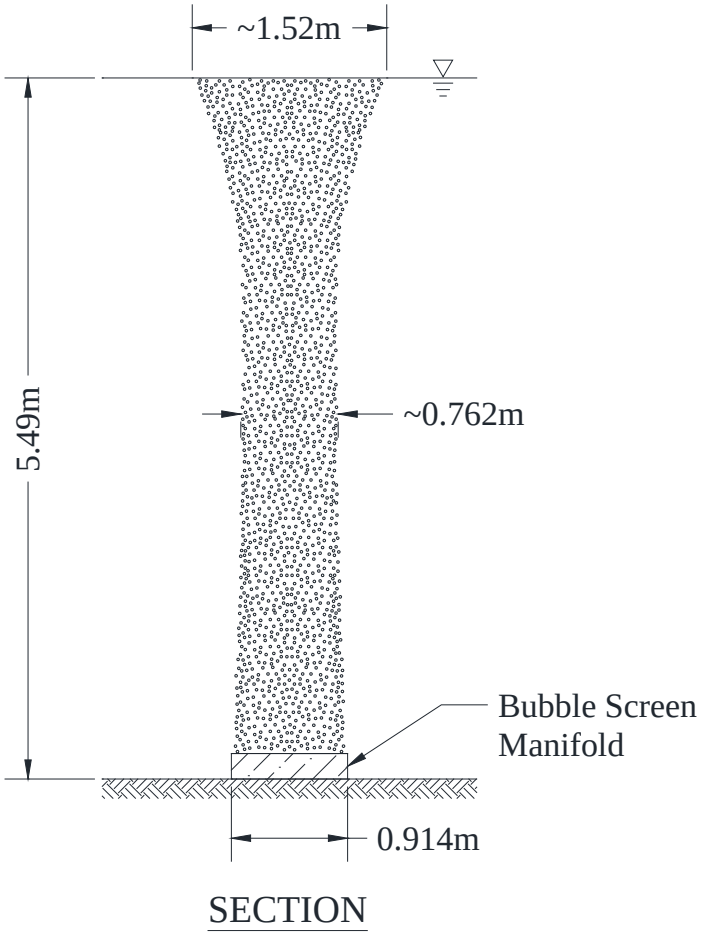

Figure 3.16 Bubble Screen Profile for a 0.914m manifold (USACE 1961)

Therefore, the pressure wave not only travelled through the bubble screen at an angle to reach the shallower gauges, it also travelled through a thicker screen (higher airflow) compared to the perpendicular measurement. Table 3.5 provides an estimate of the bubble screen thickness at each gauge depth and the effective bubble screen thickness based on the incident angle, for a standoff distance of 1.83m from the front of the bubble screen. As

seen in Table 3.5 the effective bubble screen thickness was dramatically greater for the gauge near the surface which explains the significantly better attenuation ratio shown in Figure 14 for that depth ratio. Therefore, the depth factor included in the β_i coefficients should be only be used when the expected geometry of the charge-bubble screen-structure scenario is significantly similar to the geometry used in USACE (1961). If the geometry is different, the depth ratio $z_g / z = 1.0$ may be used in Equation 41 and Equation 42.

Table 3.5 Effective Bubble Screen Thickness due to Incident Angle

Gauge Depth (m)	Gauge Radial Distance from Charge (m)	Bubble Screen Thickness[1] (m)	Effective Bubble Screen Thickness[2] (m)
2.74	2.82	0.76	0.76
1.37	3.14	0.91	1.01
0.076	3.88	1.4	3.35

[1] Estimated bubble screen thickness based on Figure 3.16
[2] Bubble screen thickness accounting for the incident angle

The predicted attenuation rate of bubble screens was investigated using data from USACE (1961). Equations developed in that study were modified to include a coefficient, β_i, that is function of target depth. However, through further analysis, it was determined that the depth ratio included in the β_i coefficient is only accurate for settings with similar geometry to the experimental setting used in USACE (1961). Therefore, for settings with geometries which are different that the experimental geometry, the depth ratio can be set to unity, which allows β_i to be applied conservatively. Additionally, the effect of bubble radius and airflow increase with bubble ascent was investigated to determine the extent these parameters might change. The bubble radius increase from 3mm to 3.45mm over approximately 5.4m, which did not appear significant, but it demonstrated the need to ensure bubble radius remains acceptably small for deeper bubble screen systems. The bubble screen airflow was shown to increase somewhat significantly at shallower depths, but the effect was indeterminate due to the dramatic effective bubble screen thickness that was also present at shallower depths. Therefore effect of increased airflow at shallower depths could be confidently included in the attenuation equations. As a result of the bubble

screen performance analysis, the improved attenuation equations were determined to be acceptable for the following design procedures, but with a caveat concerning the use of the depth ratios.

3.3.3 Verification

In an effort to verify the accuracy of Equation 39, the measured attenuation data from Table 2.5 was used with Equation 39 or Figure 3.14(A) to estimate the required airflow. The results were compared with the actual airflow used in each respective study. The relevant data from Table 2.5, additional parameters, and the results are presented in Table 3.6.

Table 3.6 Summary of Verification Data and Results

Source	Explosive Type	Airflow $\left(m^3/s/m\right)$	Peak Pressure Attenuation $\left(P_{m,r}/P_{m,fw}\right)$	Estimated[2] $A_f(P)$ $\left(m^3/s/m\right)$
Rude and Lee (2007)	C-4	0.0167	0.41	0.00667
Hempen (1993b)	Tovex 700	0.0136[1]	0.31	0.0103
USACE (1961)	TNT	0.00974	0.26	0.0132
		0.00122	0.81	0.00109
		0.000389	0.92	0.000403
Inputs: $z_g/z=1 \Rightarrow \beta_P=0.988$				

[1] Estimated based on compressor capacity

[2] Estimated using Equation 39 or Figure 3.14(A)

The estimated airflow required to attain the attenuation rates observed in the study were plotted versus the actual airflow used in the studies, see Figure 3.17. It was observed that the predicted airflow for the three USACE (1961) cases was approximately equal to the actual or conservative. This was expected since Equation 39 was developed from USACE (1961) data. Figure 3.17 also shows that Equation 39 underestimates the airflow for Rude and Lee (2007) and Hempen (1993). The cause for this discrepancy is unknown, but several possible reasons exist. First, these two studies used explosives other than TNT, which should not affect the attenuation of the pressure waves, but may be a source of variance. Secondly, both studies detonated the charges at or near the bottom of the water, which may

have allowed a bottom-transmitted wave to bypass the bubble screen and effect the attenuated peak pressure measurement. Thirdly, all three studies used different bubble screen manifolds which may demonstrate the effectiveness of one design over another.

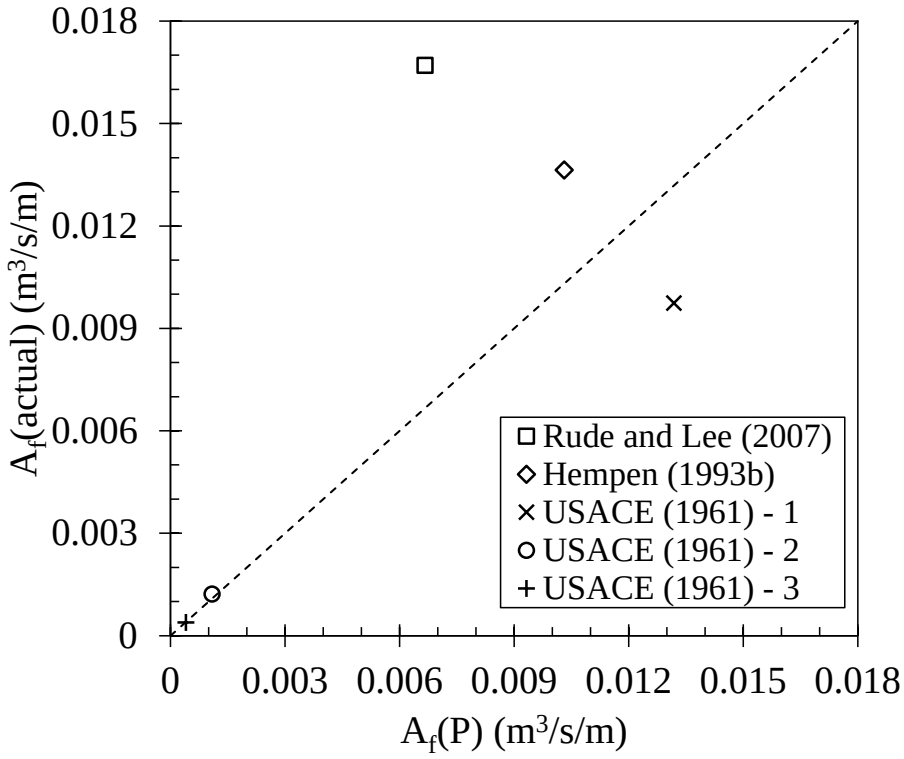

Figure 3.17 Actual versus Predicted Airflow per Equation 39

4 Design Procedures

The primary purpose of this study was to develop a comprehensive procedure to design a bubble screen system that will adequately reduce underwater explosion peak pressure and energy flux for structures. The earlier sections discussing underwater explosion characteristics and bubble screen attenuation rates were all towards this ultimate goal. There are two design procedures presented in this section. The first approaches the design of the bubble screen system as the desired outcome, based on assumptions of charge size, location, and the structural material properties. The second approach is based on known bubble screen design and structural material properties, which are then used to determine the minimum allowable radial standoff distance and/or maximum charge size. Following these approaches for bubble screen implementation, additional recommendations concerning construction and operation are presented. Finally, examples of these design procedures are presented.

Due to the intricacies of individual structures and the limited data available for the development of the figures and equations used in these procedures, the range of applicability is somewhat limited. The conditions for which the respective design aids are valid are presented with each step.

4.1 Design Procedure #1

Purpose: to determine the required airflow of a bubble screen.

Step 1: Define the following known and/or assumed parameters: charge weight, radial standoff distance, charge depth, target depth (point of interest), material strength, and controlling member response (bending, shear, etc.).

These parameters are necessary for the following steps, however, in the event some of them are unknown for the site, it may be acceptable to assume values. For example, if the target depth is unknown, assuming it is the same depth as the charge produces the lowest attenuation rate, and thus is conservative, see Figure 3.14. For charge size and radial standoff distance which may be difficult to predict, a range of each may be used to

determine the respective range of bubble screen airflows required for the resulting combinations.

Step 2: Determine the predicted peak pressure, $P_{m,fw}$, and energy flux density, U_{fw}, for the free-water scenario.

The maximum peak pressure can be predicted using Equation 26, and the maximum energy flux density can be predicted using Equation 24. Since these are empirical equations, their validity is limited to the conditions present in the experimental studies. The charge depth should be between 2.74m and 12.19m. The scaled radial distance should be between 0.79m/kg$^{1/3}$ and 50m/kg$^{1/3}$, with a minimum radial distance greater than the gas bubble radius. The explosive type must be TNT.

Since it is reasonable to expect other explosives might be used, the use of TNT equivalencies discussed in Section 2.2.2.1 may be used to estimate the effects of other high explosives, but the accuracy within Equation 24 and Equation 26 is unknown. Peak pressure and energy flux determined using equations not presented in this study may be used here, but the valid conditions should be determined.

Step 3: Determine DIF and a.

The DIF value for the compressive strength of concrete can be determined using Figure 3.6. This figure is valid for f'$_c$ values between 17.34MPa and 34.47 MPa. Also, UFC 3-340-02 (2008), which first presented Figure 3.6 recommends using a strain rate of 0.3mm/mm/s, though other strain rates may be used. The DIF values for some higher compressive strengths beyond the range mentioned above are available in UFC 3-340-02 (2008).

The DIF values for reinforcing steel are presented in Figure 3.7 and the same strain rate of 0.3mm/mm/s is recommended. Three common reinforcing steel grades are presented, both for yield strength and ultimate strength. The appropriate selection should be made depending on subsequent design calculations.

Finally, the DIF values for structural steel are presented in Figure 3.8. The two steels presented are ASTM A36 and ASTM A514. For the structural steel DIF values, UFC 3-340-02 (2008) recommends different strain rates based on the response type (bending,

shear, etc.). For bending the recommended strain rate remains 0.3mm/mm/s, but for tension and compression members, it is reduced to 0.05mm/mm/s. Additionally, for structural steels with $f_y \leq 345MPa$, an average strength increase factor, $a = 1.1$, may be applied for a further increase in design strength; for other values of f_y, $a = 1.0$.

The origination of the strain rates presented above was discussed at greater length in Section 2.3.1. While precise strain rates may be calculated following equations presented in UFC 3-340-02 (2008), a strain rate of 0.3mm/mm/s is recommended for near-range design, as presented above, and a strain rate of 0.1mm/mm/s is recommended for far-range design.

Step 4: Determine the dynamic design strength

The dynamic material strength is determined using the DIF values and equations applicable for each material type. Equation 29 is used to calculated the dynamic compressive strength of concrete. Equation 30 is used to calculated the dynamic yield strength of the reinforcing steel (f_u can be substituted for f_y in Equation 30 to calculate dynamic ultimate strength). Equation 31 is used to calculate the dynamic yield strength of structural steel. An alternative to using the dynamic design strengths is to use the nominal design strengths and have a conservative design.

Step 5: Determine the DLF.

The DLF can be determined using Figure 2.9 when the pressure wave duration (period) and the natural period of the structure are known. Biggs (1964) describes the process of determining the natural period at length.

Step 6: Determine the allowable peak pressure, $P_{m,all}$, and energy flux, U_{all}.

$P_{m,all}$ is determined by either setting the dynamic strength equal to $P_{m,all}$, or by determining the peak pressure that causes the dynamic strength to be reached in the member through static loading. It was assumed that setting $P_{m,all}$ equal to the design strength is only applicable to concrete which is more likely than steel to sustain surface damage. Equation 33 was developed to determine $P_{m,all}$ for a rectangular structural steel member with fixed-

fixed end conditions. The intent of Equation 33 was to model a member resembling a plate, and to set an example for the development of equations for other members. Thus $P_{m,all}$ for structural steel members is essentially equal to the maximum allowable uniformly distributed load. Finally, value determined for $P_{m,all}$ is divided by the DLF.

U_{all} is determined by calculating the maximum strain energy, U_{SE}, the member or structure can create. In this study, it was assumed that all the strain energy was contained in elastic strain, meaning there were no permanent deformations. Equation 34 was developed to model a single-degree-of-freedom structural steel member, in elastic strain, with fixed-fixed end conditions. Equation 35 was developed from Equation 34 for a rectangular member, such as a plate. Similar Equation 33 for peak pressure, these equations are merely intended to serve as examples for the development of member specific equations, though they are applicable within the constraints mentioned above. Additionally, a thorough analysis including determining allowable elasto-plastic strain energy may be used to increase U_{all}.

Step 7: Determine the attenuation ratio required to adequately reduce the free-water pressure wave characteristics to the allowable levels.

Use Equation 38 to determine the required attenuation ratios for peak pressure and energy flux.

Step 8: Determine the minimum bubble screen airflow to attain the required attenuation ratios.

Use Equation 41 and Equation 42 to determine the bubble screen airflow necessary to attenuate the free-water pressure wave to the allowable levels for peak pressure and energy flux, respectively. Both equations were developed based on data and equations presented by USACE (1961), and thus the same constraints apply, which include: $R/W^{1/3} < 3$, the ratio of the length of the screen versus the thickness must be greater than 12, and the quantity, $\left(A_f \cdot R\right)/\left(v \cdot 10^5\right)$ must be between, 0.0305m and 0.305m. Additionally, the β_i coefficients is constrained to depths between 0.076m and 2.74m deep. For instances in which $z_g \neq z$, the ratio z_g / z should be approximately equal to those presented in Figure

3.14. Setting $z_g / z = 1$ provides the most conservative airflow requirement, but the other ratios are valid when the scenario resembles the setting in USACE (1961).

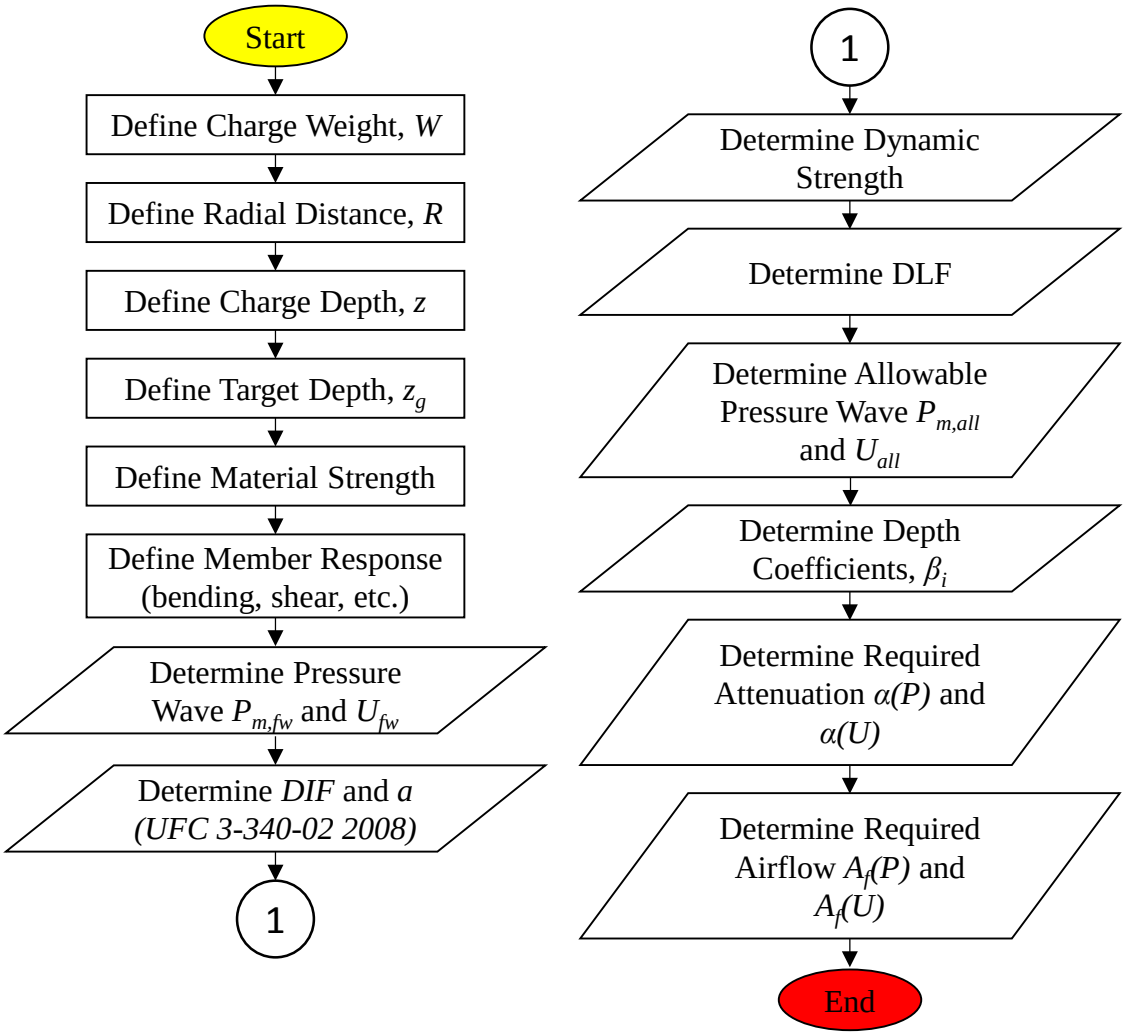

Figure 4.1 Flowchart for Design Procedure #1

4.2 Design Procedure #2

Step 1: Define the nominal material strength and the member response (bending, shear, etc.)

The material strength may be known based on the design specifications, but for concrete in particular, current testing will provide more accurate strengths and damage potential. Similar to Design Procedure #1, multiple member responses may need to be considered individually for a specific structural element, in which case this procedure may be repeated, simply modifying the member response and affected parameters in later steps.

Step 2: Determine DIF and a.

The DIF and average increase factor are determined using the figures and equations presented in UFC 3-340-02 (2008), some of which were presented previously in this study. Specifically, Figure 3.6 may be used to determine the DIF for the compressive strength of concrete with f'_c values between 17.34MPa and 34.47MPa; Figure 3.7 may be referenced for the DIF values for reinforcing steel; and Figure 3.8 may be used for the DIF values for structural steel. For structural steels with $f_y \le 345MPa$, an average strength increase factor, $a = 1.1$, may be applied for a further increase in design strength; for other values of f_y, $a = 1.0$.

Additional commentary on this step is made in Step 3 of Design Procedure #1.

Step 3: Determine the dynamic strength of the materials

The dynamic material strength is determined using the DIF values and equations applicable for each material type. Equation 29 is used to calculated the dynamic compressive strength of concrete. Equation 30 is used to calculated the dynamic yield strength of the reinforcing steel (f_u can be substituted for f_y in Equation 30 to calculate dynamic ultimate strength). Equation 31 is used to calculate the dynamic yield strength of structural steel. An alternative to using the dynamic design strengths is to use the nominal design strengths and have a conservative design.

Step 4: Determine the DLF.

The DLF can be determined using Figure 2.9 when the pressure wave duration (period) and the natural period of the structure are known. Biggs (1964) describes the process of determining the natural period at length.

Step 5: Determine the allowable peak pressure, $P_{m,all}$, and energy flux, U_{all}.

$P_{m,all}$ is determined by either setting the dynamic strength equal to $P_{m,all}$, or by determining the peak pressure that causes the dynamic strength to be reached in the member through static loading. It was assumed that setting $P_{m,all}$ equal to the design strength is only applicable to concrete which is more likely than steel to sustain surface damage. Equation 33 was developed to determine $P_{m,all}$ for a rectangular structural steel member with fixed-fixed end conditions. The intent of Equation 33 was to model a member resembling a plate, and to set an example for the development of equations for other members. Thus $P_{m,all}$ for structural steel members is essentially equal to the maximum allowable uniformly distributed load. Finally, divide the value for $P_{m,all}$ by the DLF.

U_{all} is determined by calculating the maximum strain energy, U_{SE}, the member or structure can create. In this study, it was assumed that all the strain energy was contained in elastic strain, meaning there were no permanent deformations. Equation 33 was developed to model a single-degree-of-freedom structural steel member, in elastic strain, with fixed-fixed end conditions. Equation 35 was developed from Equation 33 for a rectangular member, such as a plate. Similar Equation 33 for peak pressure, these equations are merely intended to serve as examples for the development of member specific equations, though they are applicable within the constraints mentioned above. Additionally, a thorough analysis including determining allowable elasto-plastic strain energy may be used to increase U_{all}.

Step 5: Define the bubble screen airflow, charge depth, target depth, and the minimum standoff distance or the maximum charge weight.

For this design procedure the bubble screen airflow, A_f, should be known, or may be determined through in-place testing. The predicted charge depth and target depth may be generally known or assumed, setting the target depth equal to the charge depth yield the most conservative attenuation estimation. Either the minimum standoff distance or the maximum charge weight should be defined as well, the parameter not defined will be determined in subsequent steps. Multiple iterations varying the standoff distance or charge weight may be desired to compare the relationship of these two parameters for the specific conditions present at the site.

Step 6: Determine Attenuation Ratios $\alpha(P) = P_{m,r} / P_{m,fw}$ *and* $\alpha(U) = U_{all} / U_{fw}$.

Use Figure 3.14(A) or Equation 39 to determine $\alpha(P) = P_{m,r} / P_{m,fw}$. Use Figure 3.14(B) or Equation 40 to determine $\alpha(U) = U_{all} / U_{fw}$. If the geometry of the charge location to target (point of interest) is significantly different than the setting described previously in Section 2.4.4.1, use a depth ratio $z_g / z = 1$ to provide a conservative estimate.

Step 7: Determine $P_{m,fw}$ *and* U_{fw}.

Use Equation 38 (a and b) to solve for $P_{m,fw}$ and U_{fw}, respectively. At this point the reduced peak pressure and energy flux are made equal to the allowable peak pressure and energy flux such that,

$$\alpha(P) = \frac{P_{m,r}}{P_{m,fw}} = \frac{P_{m,all}}{P_{m,fw}} \quad \text{and} \quad \alpha(U) = \frac{U_r}{U_{fw}} = \frac{U_{all}}{U_{fw}}$$

Step 8: Determine minimum standoff distance, R*, or maximum charge weight,* W.

Implementing the previously defined and determine parameters, use Equation 32 to solve for either *R* or *W*, as appropriate.

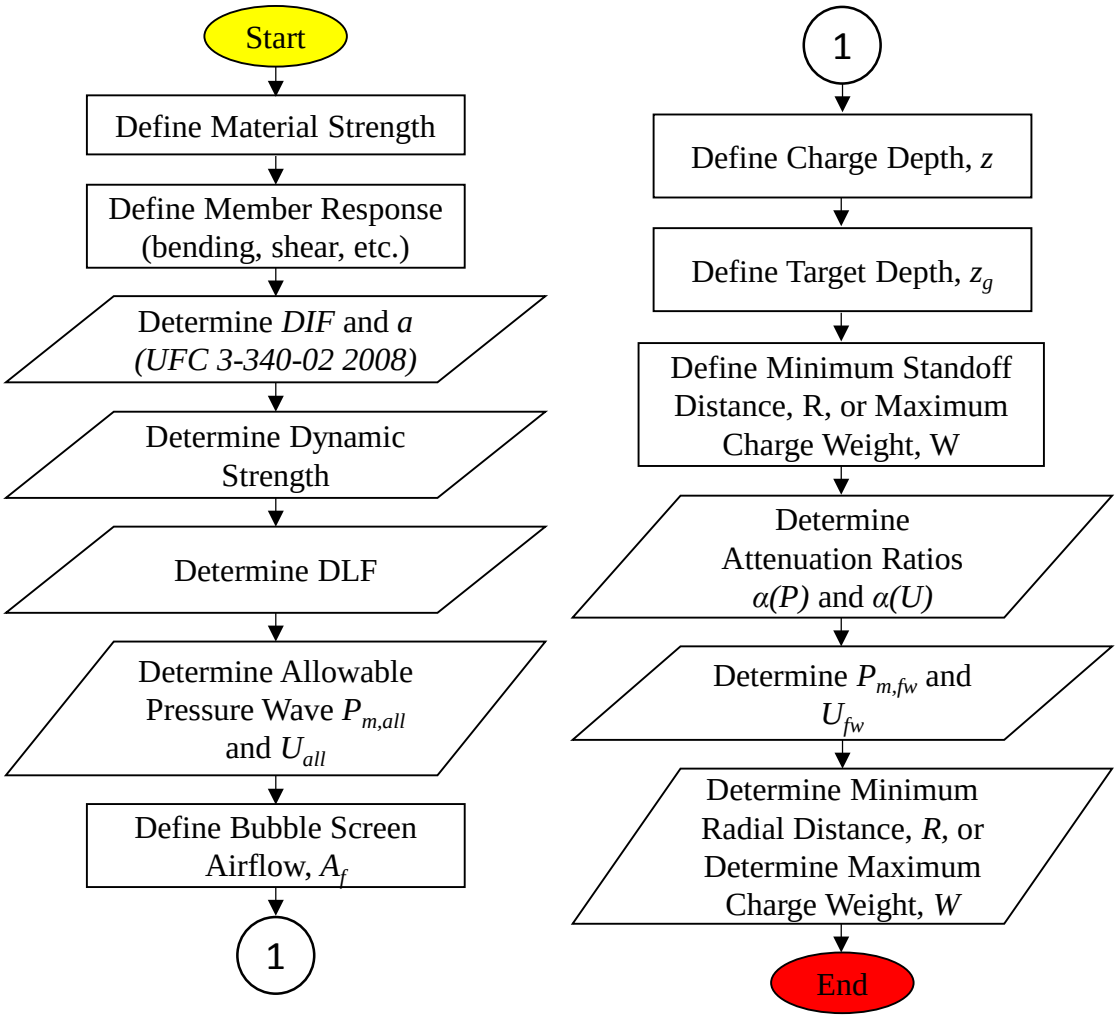

Figure 4.2 Flowchart for Design Procedure #2

4.3 Design Examples

The following two design examples use Design Procedures #1 and #2 respectively to demonstrate the procedures and the effectiveness of the bubble screens. Both examples are fictitious, but attempt to model realistic scenarios.

4.3.1 Design Example #1

A steel plate acts as a sluice gate on a mass concrete dam. The dam itself is assumed to be relatively resistant to underwater explosions, and surface damage such as spalling is acceptable. However, plastic deformation of the ASTM A36 steel plate is to be avoided.

The plate is 2m long, 30mm thick, and has fixed-fixed end conditions. The average water temperature is 20ºC. The perceived threat is assumed to be a single diver.

Step 1: Define known and/or assumed parameters.

Charge Weight, $W = 50kg$

Charge Depth, $z = 10m$

Target Depth, $z_g = 10m$

Radial Standoff Distance, $R = 30m$

Material Strength, $f_y = 248MPa$

Material Response = Bending

Step 2: Determine the predicted peak pressure, $P_{m,fw}$, and energy flux density, U_{fw}, for the free-water scenario.

Peak Pressure:

$$\frac{P_m}{P_z} = A\left(\frac{R}{W^{1/3}}\right)^B \tag{26}$$

$$A = 4510.1(z)^{-0.927} \tag{27}$$

$$A = 4510.1(10m)^{-0.927} = 533.6$$

$$B = -1.1 \tag{28}$$

Equation 24 rewritten:

$$P_m = A\left(\frac{R}{W^{1/3}}\right)^B \cdot \gamma_w z$$

$$P_m = 533.6\left(\frac{30m}{(50kg)^{1/3}}\right)^{-1.1} \cdot \left(9810\frac{N}{m^3} \cdot 10m\right) = 0.521MPa$$

Energy Flux:

$$U = 94.3W^{1/3}\left(\frac{R}{W^{1/3}}\right)^{-2.08} \tag{24}$$

$$U = 94.3(50kg)^{1/3}\left(\frac{30m}{(50kg)^{1/3}}\right)^{-2.08} = 4.43kPa - m$$

Step 3: Determine DIF and average increase factor, a.

Average increase factor:

$$f_y = 248MPa \le 345MPa$$

$$a = 1.1$$

DIF:

Determine strain rate for bending and assume near-range design,

$\varepsilon' = 0.3mm/mm/s$, per UFC 3-340-02 (2008)

Use Figure 4.3 (see Figure 3.8) to determine DIF,

$$DIF = 1.37$$

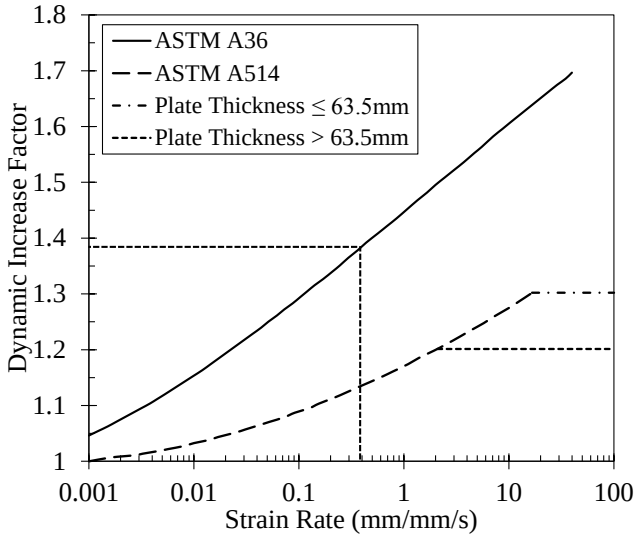

Figure 4.3 Dynamic Increase Factors for Yield Stresses of ASTM A36 and A514 Steels (after UFC 3-340-02 2008)

Step 4: Determine the dynamic design strength

$$f_{dy} = DIF \cdot a \cdot f_y \tag{31}$$

$$f_{dy,b} = 1.37 \cdot 1.1 \cdot 248MPa = 374MPa$$

Step 5: Determine the DLF.

$$DLF = 1.0 \text{ (assumed)}$$

Step 6: Determine the allowable peak pressure, $P_{m,all}$, and energy flux, U_{all}.

Peak Pressure:

$$P_{m,all} = \frac{2 f_{dy,b} h^2}{l^2} \tag{33}$$

$$h = 30mm = 0.03m$$

$$l = 2m$$

$$P_{m,all} = \frac{2(374MPa)(0.03m)^2}{(2m)^2} = 0.168MPa$$

Energy Flux:

For solid rectangular member,

$$U_{SE} = U_{all} = \frac{f_{dy,b}^2 h \cdot l}{30E \cdot l'} \tag{35}$$

$$E = 200{,}000MPa$$

$$U_{all} = U_{SE} = \frac{(374MPa)^2 \cdot 0.03m \cdot 2m}{30 \cdot 200{,}000MPa \cdot 1m} = 1.40kPa - m$$

Step 7: Determine the attenuation ratio required to adequately reduce the free-water pressure wave characteristics to the allowable levels.

$$\alpha(P) = \frac{P_{m,all}}{P_{m,\,fw}} \tag{38a}$$

$$\alpha(P) = \frac{0.168MPa}{0.521MPa} = 0.322$$

$$\alpha(U) = \frac{U_{all}}{U_{fw}} \tag{38b}$$

$$\alpha(U) = \frac{1.40kPa - m}{4.43kPa - m} = 0.316$$

Step 8: Determine the minimum bubble screen airflow to attain the required attenuation ratios.

β_i coefficients,

$$\beta_P = 0.885\left(\frac{z_g}{z}\right) + 0.103 \tag{39}$$

$$\beta_P = 0.885\left(\frac{10m}{10m}\right) + 0.103 = 0.988$$

$$\beta_U = 0.0419e^{\left[3.455\left(\frac{z_g}{z}\right)\right]} \tag{40}$$

$$\beta_U = 0.0419e^{\left[3.455\left(\frac{10m}{10m}\right)\right]} = 1.326$$

Required bubble screen airflow,

Kinematic viscosity $v = 1.004 \cdot 10^{-6}\frac{m^2}{s}$ at 20ºC

$$A_f\left(P_m\right) = 0.0467\left(v \cdot 10^5\right)\left[\left(\frac{P_{m,r}}{P_{m,fw}}\right)^{-1} - 1\right]\beta_P \tag{37}$$

$$A_f\left(P_m\right) = 0.0467\left(1.004 \cdot 10^{-6}\frac{m^2}{s} \cdot 10^5\right)\left[(0.322)^{-1} - 1\right](0.988) = 0.00975\frac{\frac{m^3}{s}}{m}$$

$$A_f(U) = 0.0233(v \cdot 10^5)\left[\left(\frac{U_r}{U_{fw}}\right)^{-1} - 1\right]\beta_U \tag{38}$$

$$A_f(U) = 0.0233\left(1.004 \cdot 10^{-6}\,\frac{m^2}{s} \cdot 10^5\right)\left[(0.316)^{-1} - 1\right](1.326) = 0.00500\,\frac{\frac{m^3}{s}}{m}$$

Design Summary:

$$A_f(P) > A_f(U) \therefore A_f \geq 0.00975\,\frac{\frac{m^3}{s}}{m}$$

4.3.2 Design Example #2

The operators of a large concrete dam have acquired a proprietary bubble screen manifold with an anticipated airflow of *0.005m³/s/m.* The primary concern from underwater explosions is surface damage, which is assumed to occur if the peak pressure exceeds the dynamic compressive strength of the structure. Due to the existing site conditions, the maximum charge weight is assumed to be 200kg, and the ability to create a large standoff distance is impractical.

Step 1: Define material strength and member response.

Material Strength, $f_c' = 20MPa$

Member Response = compression

Step 2: Determine DIF and average increase factor, a.

Average increase factor:

Not applicable for concrete

DIF:

Determine strain rate, assumed near-range design,

$\varepsilon' = 0.3mm/mm/s$, per UFC 3-340-02 (2008)

Use Figure 4.4 (see Figure 3.6) to determine DIF,

$$DIF \approx 1.25$$

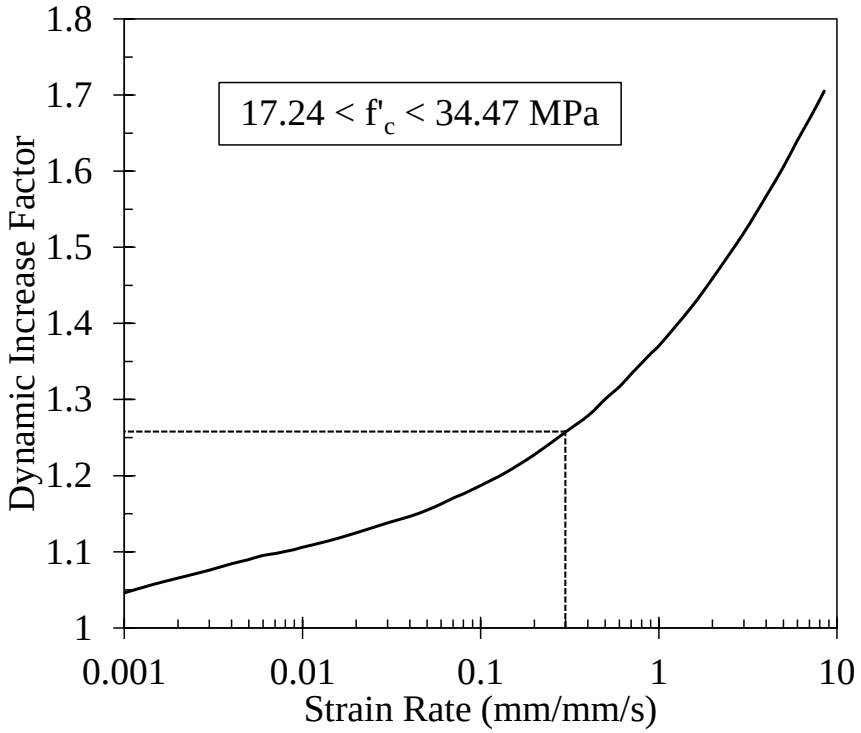

Figure 4.4 Design Curve for DIF for ultimate Compressive Strength of Concrete with 17.24 < f'_c < 34.47 MPa, (after UFC 3-340-02 2008)

Step 3: Determine the dynamic design strength

$$f'_{dc} = DIF \cdot f'_c \tag{29}$$

$$f'_{dc} = 1.25 \cdot 20MPa = 25MPa$$

Step 4: Determine the DLF.

$$DLF = 1.0 \text{ (assumed)}$$

Step 5: Determine the allowable peak pressure, $P_{m,all}$, and energy flux, U_{all}.

Peak Pressure:

$$P_{m,all} = f'_{dc}$$

$$P_{m,all} = 25MPa$$

Energy Flux:

Not applicable.

Step 6: Define bubble screen airflow, charge depth, target depth, and minimum standoff distance or maximum charge weight.

Bubble screen airflow, $A_f = 0.005 \frac{\frac{m^3}{s}}{m}$

Charge depth, $z = 2.5m$

Target depth, $z_g = 2.5m$

Charge weight, $W = 200kg$

Step 7: Determine Attenuation Ratios $\alpha(P) = P_{m,r} / P_{m,fw}$ *and* $\alpha(U) = U_{all} / U_{fw}$.

Peak Pressure:

Use Figure 4.5 (see Figure 3.14(A)) to determine $\alpha(P) = P_{m,r} / P_{m,fw}$ for $A_f = 0.005 m^3 / s / m$.

$$\alpha(P) = \frac{P_{m,r}}{P_{m,fw}} \approx 0.48$$

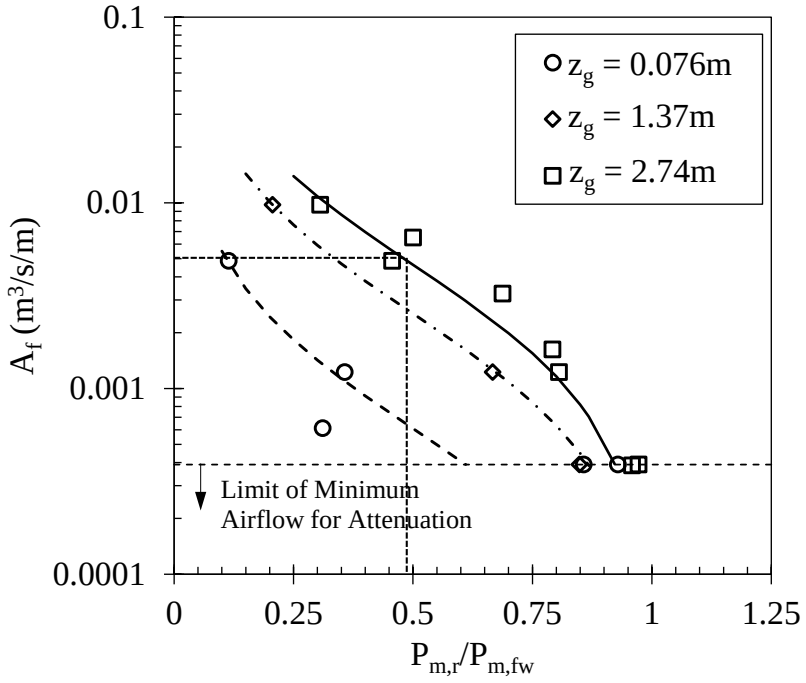

Figure 4.5 Peak Pressure Attenuation versus Airflow for Various Gauge Depths

Energy Flux:

Not applicable.

Step 8: Determine $P_{m,fw}$ *and* U_{fw}.

Peak Pressure:

$$P_{m,fw} = \frac{P_{m,all}}{\alpha(P)} \tag{38a}$$

$$P_{m,fw} = \frac{25MPa}{0.48} = 52.1MPa$$

Energy Flux:

Not applicable.

Step 9: Determine minimum standoff distance, R*, or maximum charge weight,* W.

W is known, therefore use Equation 32 to solve for R.

$$R = \left(\frac{P_{m,fw}}{P_z A} \right)^{1/B} W^{1/3}(m) \tag{32}$$

$$A = 4510.1(z)^{-0.927} \tag{27}$$

$$A = 4510.1(2.5m)^{-0.927} = 1929$$

$$B = -1.1 \tag{28}$$

$$P_z = \gamma_w \cdot z$$

$$P_z = 9810 \frac{N}{m^3} \cdot 2.5m = 0.0245MPa$$

$$R = \left(\frac{52.1MPa}{0.0245MPa \cdot 1929} \right)^{1/-1.1} (200)^{1/3} = 5.35m$$

Design Summary:

$$R = 5.35m$$

4.4 Additional Recommendations

While the previous design procedures provide information regarding the required bubble screen parameters and/or the effect of a bubble screen to reduce pressure wave characteristics, there are many other practical considerations when implementing a bubble screen. Some of the following recommendations were generated from previous studies, and others address potential challenges raised in this study.

Due to the complexity of airflow distributions, especially considering output at hydrostatic pressure, it is recommended to have an engineer design the bubble screen manifold and compressor and/or conduct tests to determine the actual airflow of the system. Ceasing or reducing airflow may reduce operational costs during low threat conditions. However if reduced airflow causes the air pressure in the manifold to drop below hydrostatic pressure, water and particulates may enter the manifold and block the orifices (Rude and Lee 2007). Therefore it is recommended that the design include specifications for low airflow

situations, and that the manifold be removed from the water if not in use, unless otherwise designed.

Small bubbles provide greater acoustic impedance than larger bubbles and thus increased attenuation. Thus small bubbles are preferable (Rude and Lee 2007, Domenico 1982a).

In turbulent or high-flow settings, multi-stage or multi-level manifolds were shown to produce more consistent bubble screens in CALTRAN (2009). Also, if the bubble screen is sufficiently deep, multiple screens may need to be implemented in levels to ensure small bubble exist throughout the screen. See Section 3.3.1 about bubble radius increase with rise.

Manifold robustness versus flexibility is another consideration, particularly considering a multiple explosion event (preliminary explosions may even be specifically planned to damage the manifold, leaving the structure unprotected for subsequent explosions). Robust manifolds provide a durable design that can withstand high blast pressures, however these are expensive to construct and damage to the manifold may be difficult to repair. Flexible manifolds (e.g. EPDM) are typically less expensive to construct and may deflect without incurring debilitating damage. If damage is incurred, it is likely to be significant, though relatively inexpensive and simple to repair. It might be advantageous to attach flexible manifolds to a rigid frame with lift cables to facilitate repairs and/or maintenance.

A redundant design may offer several benefits. Increased bubble screen attenuation may be realized by implementing multiple (up to four) parallel bubble screens (Domenico 1982b). Furthermore, if one screen is damaged from the first of multiple explosions, the remaining operational screen(s) will still attenuate the following explosions to some degree.

5 Conclusions

The purpose of this research was to develop a comprehensive procedure to design a bubble screen to attenuate pressure waves produced by underwater explosions. Previous research and literature was reviewed to determine the current methods available. Data was compiled from multiple sources to provide a means to investigate the accuracy of existing equations, and to develop improvements that better represent the data. Using the data, new similitude equations were developed to predict peak pressure and energy flux density, and the peak pressure equation was further modified to include the effects of depth. To accurately represent the strength of materials under the high strain rates imposed by blast loads, dynamic increase factors were determined and applied to model the dynamic strength of materials. The dynamic strengths were then used in conjunction with loading equations to determine the allowable peak pressure and energy flux. Using the allowable loads and the free-water loads determined with the similitude equations, the required attenuation rates for a bubble screen were calculated. The attenuation performance from bubble screens tested in USACE (1961) was analyzed and the attenuation equations in that study were modified to include a coefficient that incorporates depth. These results were then compiled to form two bubble screen design procedures and examples, one for customized bubble screens systems, and another for existing bubble screen systems.

The attenuation equations with the addition of the coefficient correspond well with the data. However, it was determined that the test geometry caused the pressure wave to travel a much greater distance through the bubble screen to reach the gauges at shallower depths. Therefore, the coefficient does not represent depth so much as it represents the angle the pressure wave traveled from perpendicular. Therefore it remains valid for the data, and is expected to perform well for situations where the target is at a similar angle as in the experiment, but it should not be used based on depth alone. In situations where the geometry is different the coefficients can still be used by setting the depth ratio equal to unity.

Limitations to this research stem primarily from lack of additional data to validate the equations developed and modified, particularly regarding the attenuation properties of bubble screens which was solely based on USACE (1961). Several documents provide design recommendations or partial procedures for bubble screen design, but are either classified or lack data for comparison (Hempen 1993b, Langefors and Kihlstrom 1978, and USACE 1961).

Recommendations for future research include: physical testing of the equations and procedures presented in this study, extensive testing at various depths to better determine the effect of depth on bubble screen attenuation performance, and full-size or scale tests of structural/material response when exposed to underwater explosions.

Appendix A

Figures and Equation Derivations

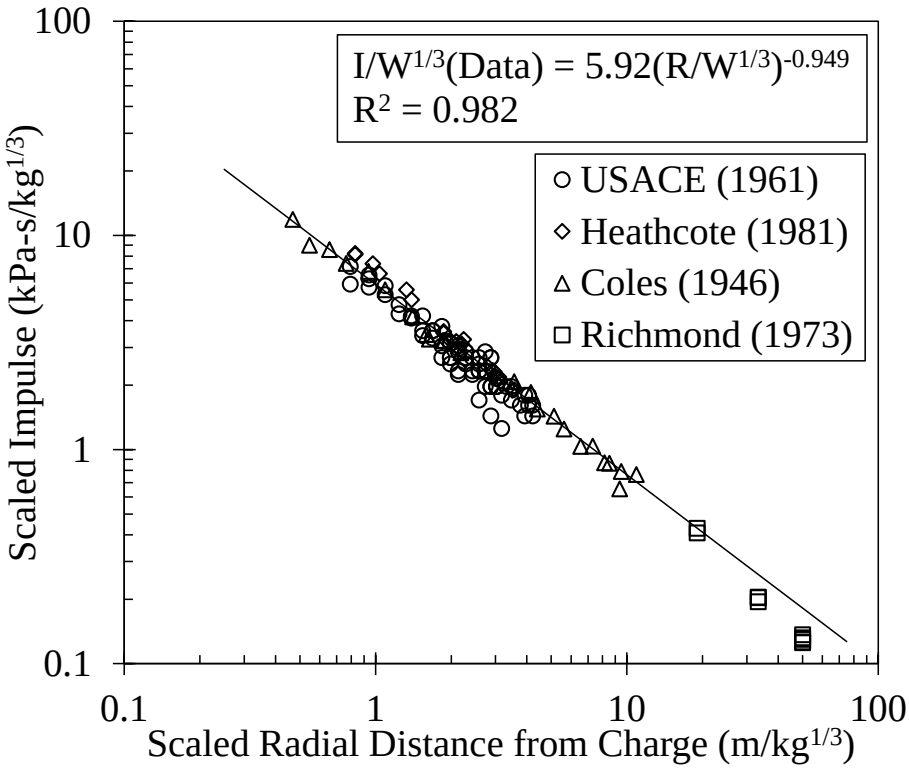

Figure A.1 Scaled Measured Impulse Data with New Equation

$$\frac{I}{W^{1/3}}(Data) = 5.92\left(\frac{R}{W^{1/3}}\right)^{-0.949} \qquad R^2 = 0.982 \qquad (51)$$

$$\frac{I}{W^{1/3}}(Swisdak,1978) = 5.75\left(\frac{R}{W^{1/3}}\right)^{-0.89} \qquad R^2 = 0.962 \qquad (52)$$

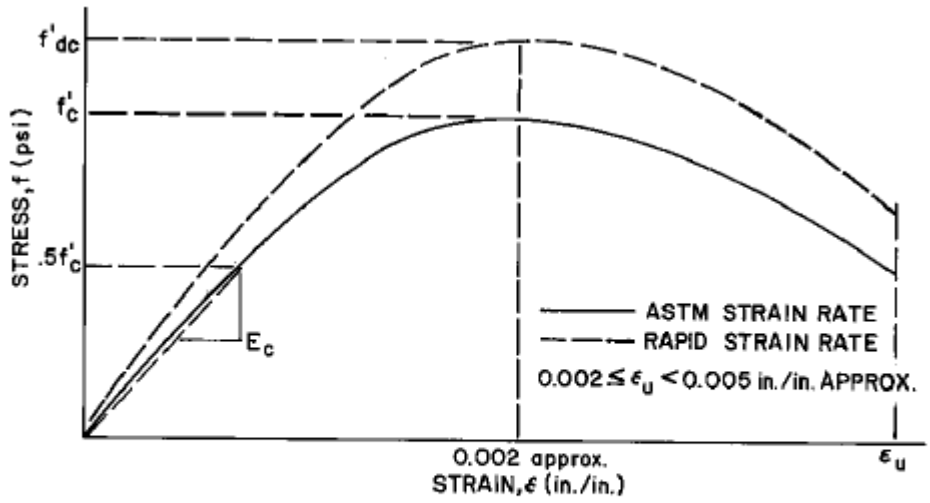

(a) STRESS-STRAIN CURVE FOR CONCRETE

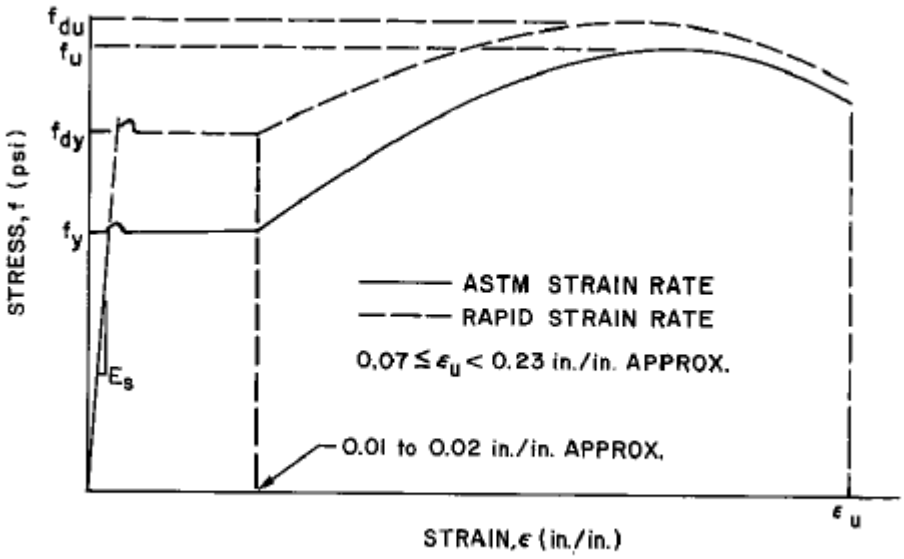

(b) STRESS-STRAIN CURVE FOR STEEL

Figure A.2 Typical Stress-Strain Curves for Concrete and Reinforcing Steel

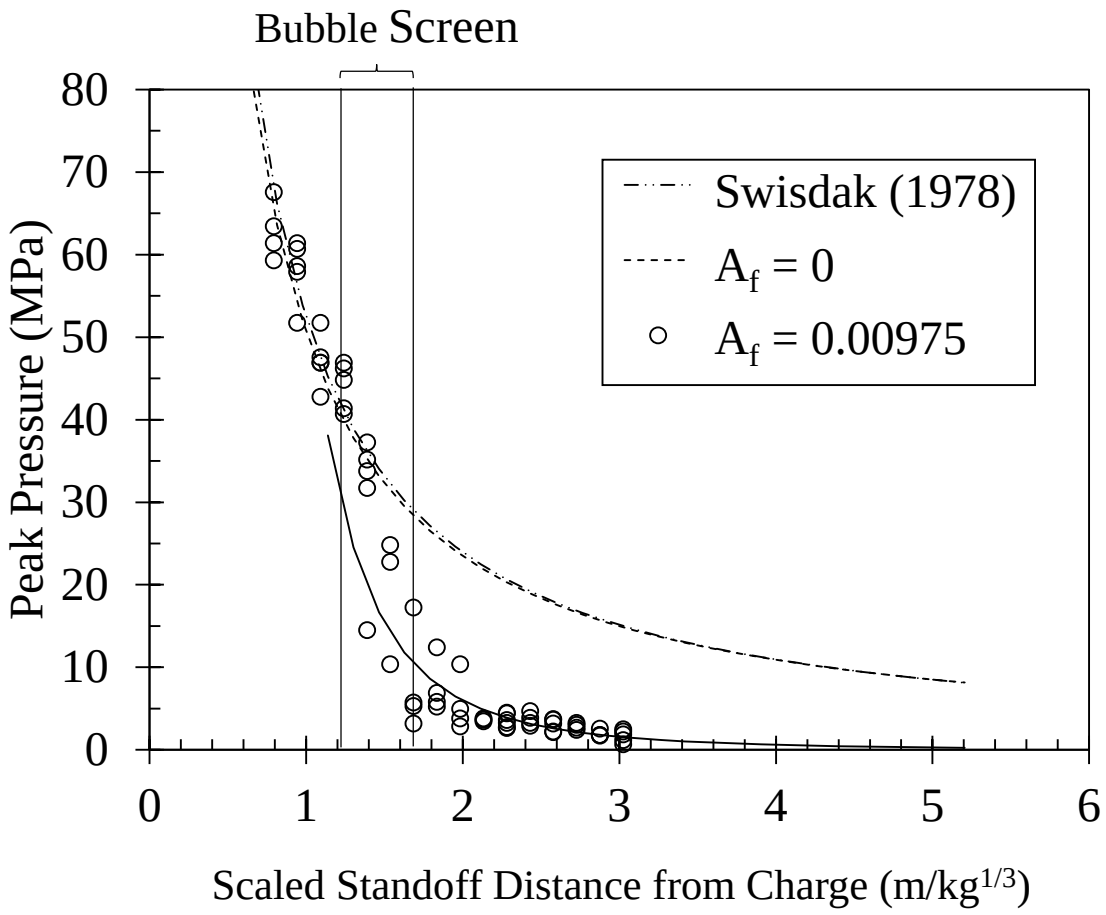

Figure A.3 Bubble Screen Attenuation for A_f = 0.00975m^3/s/m and 0.914m Thickness (USACE 1961).

Allowable Peak Pressure Equation Derivation, Equation 33

Moment	M
Linear distributed load	w
Member length	l
Peak pressure (not point load)	P_m
Member height or width	b
Dynamic yield stress in bending	$f_{dy,b}$
Member centroid	c
Member moment of inertia	I
Member depth	h
Allowable load to not exceed yield stress	*all* (subscript)
Max moment for fixed-fixed member with uniform linear load (AISC 2011):	$M = \frac{w \cdot l^2}{12}$
Uniform linear load equivalent:	$w = P_m \cdot b$
Allowable dynamic bending stress in member:	$f_{dy,b} = \frac{M_{all} \cdot c}{I}$
Member centroid:	$c = \frac{h}{2}$
Member moment of inertia:	$I = \frac{1}{12} b \cdot h^3$
Substituting for allowable bending stress:	$f_{dy,b} = \frac{\frac{(P_m \cdot b) \cdot l^2}{12} \cdot \frac{h}{2}}{\frac{1}{12} b \cdot h^3}$
Reduced allowable dynamic bending stress:	$f_{dy,b} = \frac{P_m \cdot l^2}{2 \cdot h^2}$
Allowable peak pressure (maximum):	$P_{m,all} = \frac{2 \cdot f_{dy,b} \cdot h^2}{l^2}$

Allowable Energy Flux Equation Derivation, Equation 34 (2 pages)

Strain energy in bending	U_m	Member segment length	x
Normal stress	σ_x	Linear distributed load	w
Modulus of elasticity	E	Member length	l
Member volume	V	Dynamic yield stress in bending	$f_{dy,b}$
Moment	M	Member depth	h
Member centroid	c	Member height or width	b
Member moment of inertia	I	Allowable energy flux density	U_{all}
Member cross-sectional area	A		

Strain energy in bending.	$U_m = \int \frac{\sigma_x^{\,2}}{2E} dV$
Normal stress equivalent.	$\sigma_x = \frac{M \cdot c}{I}$
Substituting.	$U_m = \int \frac{M^2 \cdot c^2}{2EI^2} dV$
*dV e*quivalent.	$dV = dAdx$
Substituting. Only *c* is a function of *A*.	$U_m = \int \frac{M^2}{2EI^2} \left(\int c^2 dA \right) dx$
Moment of inertia equivalent.	$I = \int c^2 dA$
Substituting and reducing.	$U_m = \int \frac{M^2}{2EI} dx$
Moment equation for a single-degree-of-freedom beam with fixed-fixed end conditions. Length equivalent.	$M = \frac{w \cdot l^2}{12},\ l = x$
Substituting.	$U_m = \int_0^l \frac{w^2 \cdot x^4}{288EI} dx$
Solving.	$U_m = \frac{w^2 \cdot l^5}{1440EI}$
Moment and yield stress equivalent. Continue using moment equation for fixed-fixed beam.	$M = \frac{f_{dy,b} \cdot I}{c} = \frac{w \cdot l^2}{12}$

Allowable Energy Flux Equation Derivation, Equation 34 (continued)

Substituting and reducing.	$U_m = \frac{f_{dy,b}{}^2 \cdot I \cdot l}{10c^2 E}$
Centroid equation for a rectangular section.	$c = \frac{h}{2}$
Substituting and reducing.	$U_m = \frac{2 f_{dy,b}{}^2 \cdot I \cdot l}{5h^2 E}$
Allowable energy flux density equivalent, $l' =$ unit length.	$U_{all} = \frac{U_m}{b \cdot l'}$
Substituting and reducing. Allowable energy flux density equation.	$U_{all} = \frac{2 f_{dy,b}{}^2 \cdot I \cdot l}{5bh^2 E \cdot l'}$

Appendix B

Data Tables

Table B.1 Pressure Wave Data (Coles 1946)

Coles (1946)

Depth, z = 12.19m

Charge Weight, W = 21.79kg

R (m)	$R/W^{1/3}$ ($m/kg^{1/3}$)	P_m (Mpa)	I (kPa-s)	U (kPa-m)	θ (ms)	$I/W^{1/3}$ ($kPa\text{-}s/kg^{1/3}$)	$U/W^{1/3}$ ($kPa\text{-}m/kg^{1/3}$)
1.52	0.546	96.5	25.2	735	0.230	9.01	263
2.13	0.764	68.3	20.7	399	0.240	7.41	143
3.05	1.09	45.5	15.6	201	0.280	5.58	72.1
4.57	1.64	26.2	9.17	69.1	0.280	3.28	24.7
5.18	1.86	23.7	9.03	58.5	0.280	3.23	20.9
6.10	2.18	22.2	7.93	44.6	0.290	2.84	16.0
11.6	4.15	11.0	5.17	13.7	0.390	1.85	4.90
14.3	5.13	8.21	4.00	8.61	0.340	1.43	3.08
18.3	6.55	6.36	2.90	4.67	0.340	1.04	1.67
23.8	8.51	4.83	2.41	3.01	0.390	0.864	1.08
26.5	9.49	4.16	2.21	2.29	0.390	0.790	0.821
30.5	10.9	3.34	2.14	1.86	0.420	0.765	0.664

Depth, z = 12.19m

Charge Weight, W = 34.50kg

R (m)	$R/W^{1/3}$ ($m/kg^{1/3}$)	P_m (Mpa)	I (kPa-s)	U (kPa-m)	θ (ms)	$I/W^{1/3}$ ($kPa\text{-}s/kg^{1/3}$)	$U/W^{1/3}$ ($kPa\text{-}m/kg^{1/3}$)
1.52	0.47	131	38.7	1425	0.260	11.9	438
2.13	0.66	85.5	28.0	695	0.270	8.60	213
3.05	0.94	56.4	22.1	362	0.300	6.80	111
4.57	1.40	31.2	13.6	128	0.350	4.17	39.4
5.18	1.59	29.1	11.2	94.5	0.290	3.45	29.0
6.10	1.87	25.9	10.5	71.6	0.320	3.22	22.0
11.6	3.56	14.6	6.76	23.8	0.350	2.08	7.31
14.3	4.40	11.0	5.03	13.6	0.370	1.55	4.18
18.3	5.62	7.35	4.07	7.72	0.440	1.25	2.37
23.8	7.30	5.61	3.38	5.01	0.430	1.04	1.54
26.5	8.15	5.24	2.83	3.76	0.440	0.868	1.16
30.5	9.36	3.98	2.14	2.54	0.480	0.657	0.779

Notes:

- Charges were suspended 12.19m below the surface in at least 24.38m of water
- TNT loading density ≈ 1.52
- Gauges suspended at same level as charge
- Impulse and energy flux time of integration is 6.7θ

Table B.2 Pressure Wave Data (USACE 1961)

USACE - Freewater Data (1961)

Depth, z = 2.743m

Charge Weight, W = 3.63kg

R (m)	$R/W^{1/3}$ ($m/kg^{1/3}$)	P_m (MPa)	I (kPa-s)	U (kPa-m)	$I/W^{1/3}$ ($kPa\text{-}s/kg^{1/3}$)	$U/W^{1/3}$ ($kPa\text{-}m/kg^{1/3}$)
1.22	0.793	67.6	9.10	203	5.92	132
1.22	0.793	62.1	11.0	252	7.18	164
1.45	0.942	60.7	9.65	217	6.28	141
1.45	0.942	55.8	10.1	228	6.55	148
1.45	0.942	57.9	8.83	147	5.74	95.7
1.68	1.09	51.0	8.14	147	5.29	95.7
1.68	1.09	49.6	8.96	151	5.83	98.0
1.91	1.24	33.8	6.62	80.6	4.31	52.4
1.91	1.24	38.6	7.31	94.6	4.76	61.5
2.13	1.39	34.5	6.34	84.1	4.13	54.7
2.13	1.39	31.0	6.48	77.1	4.22	50.1
2.13	1.39	33.1	6.34	70.1	4.13	45.6
2.36	1.54	31.7	6.48	80.6	4.22	52.4
2.36	1.54	32.4	5.52	63.0	3.59	41.0
2.36	1.54	31.0	5.24	56.0	3.41	36.5
2.59	1.69	24.8	5.10	49.0	3.32	31.9
2.59	1.69	31.7	5.52	49.0	3.59	31.9
2.59	1.69	33.1	5.52	59.5	3.59	38.7
2.82	1.83	24.8	4.69	35.0	3.05	22.8
2.82	1.83	24.8	4.14	29.8	2.69	19.4
2.82	1.83	24.8	5.79	45.5	3.77	29.6
3.05	1.98	22.1	4.14	28.0	2.69	18.2
3.05	1.98	26.9	4.14	31.5	2.69	20.5
3.05	1.98	24.8	3.86	31.5	2.51	20.5
3.05	1.98	24.8	4.83	42.0	3.14	27.3
3.05	1.98	23.4	4.83	31.5	3.14	20.5
3.28	2.13	22.8	4.55	29.8	2.96	19.4
3.28	2.13	19.3	3.45	22.8	2.24	14.8
3.28	2.13	22.8	3.59	24.5	2.33	16.0
3.28	2.13	22.8	4.41	26.3	2.87	17.1
3.28	2.13	20.0	4.69	35.0	3.05	22.8
3.51	2.28	22.1	4.41	35.0	2.87	22.8
3.51	2.28	18.6	3.86	26.3	2.51	17.1
3.51	2.28	22.1	4.41	31.5	2.87	20.5
3.51	2.28	17.9	4.14	24.5	2.69	16.0

Table B.2 Pressure Wave Data (USACE 1961) cont.

R (m)	$R/W^{1/3}$ ($m/kg^{1/3}$)	P_m (MPa)	I (kPa-s)	U (kPa-m)	$I/W^{1/3}$ ($kPa\text{-}s/kg^{1/3}$)	$U/W^{1/3}$ ($kPa\text{-}m/kg^{1/3}$)
3.73	2.43	20.0	4.14	33.3	2.69	21.7
3.73	2.43	20.0	3.45	24.5	2.24	16.0
3.73	2.43	17.9	3.59	19.3	2.33	12.5
3.96	2.58	17.9	3.59	19.3	2.33	12.5
3.96	2.58	17.9	3.59	21.0	2.33	13.7
3.96	2.58	18.6	3.86	24.5	2.51	16.0
3.96	2.58	14.5	2.62	17.5	1.70	11.4
3.96	2.58	15.9	4.14	17.2	2.69	11.2
4.19	2.73	17.2	3.59	21.0	2.33	13.7
4.19	2.73	17.2	3.59	19.3	2.33	12.5
4.19	2.73	16.5	3.03	15.1	1.97	9.80
4.19	2.73	17.9	4.41	29.8	2.87	19.4
4.19	2.73	16.5	3.59	21.0	2.33	13.7
4.42	2.88	15.2	3.03	17.2	1.97	11.2
4.42	2.88	13.8	2.21	9.46	1.44	6.15
4.42	2.88	15.2	3.03	14.0	1.97	9.12
4.42	2.88	17.9	4.14	15.1	2.69	9.80
4.42	2.88	16.5	4.14	24.5	2.69	16.0
4.65	3.02	14.5	3.03	15.4	1.97	10.0
4.65	3.02	15.2	3.31	15.8	2.15	10.3
4.65	3.02	14.5	3.03	14.0	1.97	9.12
4.65	3.02	15.2	3.31	16.8	2.15	10.9
4.65	3.02	11.7	3.03	13.3	1.97	8.66
4.88	3.17	13.1	1.93	9.46	1.26	6.15
4.88	3.17	14.5	2.76	13.0	1.79	8.43
5.11	3.32	13.8	3.03	11.6	1.97	7.52
5.33	3.47	11.7	2.62	8.41	1.70	5.47
5.33	3.47	13.8	3.03	14.4	1.97	9.34
5.79	3.77	11.7	2.48	8.76	1.62	5.70
6.02	3.92	11.0	2.21	7.71	1.44	5.01
6.02	3.92	11.0	2.76	12.6	1.79	8.20
6.25	4.07	13.1	2.48	8.06	1.62	5.24
6.25	4.07	11.7	2.76	14.0	1.79	9.12
6.48	4.21	11.0	2.21	7.01	1.44	4.56
6.48	4.21	10.3	2.48	8.76	1.62	5.70

Notes:
- Charges were suspended at mid-depth in 5.486m of water
- TNT loading density - not specified
- Gauges suspended at same level as charge
- Impulse and energy flux time of integration is 6.7θ

Table B.3 Pressure Wave Data (Richmond 1973)

Richmond (1973)

Depth, z = 3.048m
Charge Weight, W = 0.227kg

R (m)	$R/W^{1/3}$ ($m/kg^{1/3}$)	P_m (Mpa)	$I/W^{1/3}$ (kPa-s)	$U/W^{1/3}$ (kPa-m)	θ (ms)	$I/W^{1/3}$ ($kPa-s/kg^{1/3}$)	$U/W^{1/3}$ ($kPa-m/kg^{1/3}$)
30.48	50.0	0.641	0.0834	0.0175	0.111	0.137	0.0287
30.48	50.0	0.765	0.0807	0.0210	0.096	0.132	0.0344
30.48	50.0	0.634	0.0793	0.0175	0.112	0.130	0.0287
30.48	50.0	0.669	0.0772	0.0175	0.095	0.127	0.0287
30.48	50.0	0.655	0.0765	0.0175	0.092	0.125	0.0287

Depth, z = 3.048m
Charge Weight, W = 0.454kg

R (m)	$R/W^{1/3}$ ($m/kg^{1/3}$)	P_m (Mpa)	$I/W^{1/3}$ (kPa-s)	$U/W^{1/3}$ (kPa-m)	θ (ms)	$I/W^{1/3}$ ($kPa-s/kg^{1/3}$)	$U/W^{1/3}$ ($kPa-m/kg^{1/3}$)
14.6	19.0	1.85	0.314	0.170	0.128	0.408	0.221
14.6	19.0	1.88	0.330	0.175	0.128	0.429	0.228
25.6	33.3	1.05	0.157	0.0508	0.115	0.205	0.0660
25.6	33.3	1.08	0.157	0.0525	0.120	0.204	0.0683
25.6	33.3	1.14	0.150	0.0560	0.120	0.195	0.0729

Notes:
- Charges were suspended 3.048m below the surface in 9.144m of water
- TNT loading density - not specified
- Gauges suspended at same level as charge
- Impulse and energy flux time of integration - not specified

Table B.4 Pressure Wave Data (Heathcote 1981)

Heathcote (1981)

Depth, z = 10.67m

Charge Weight, W = 3.18kg

R (m)	$R/W^{1/3}$ ($m/kg^{1/3}$)	P_m (Mpa)	I (kPa-s)	U (kPa-m)	$I/W^{1/3}$ ($kPa\text{-}s/kg^{1/3}$)	$U/W^{1/3}$ ($kPa\text{-}m/kg^{1/3}$)
1.52	1.04	53.2	9.77	136	6.64	92.2
1.43	0.974	60.7	10.9	166	7.40	113
1.22	0.829	72.1	12.1	223	8.24	152
1.22	0.829	70.5	12.0	217	8.15	148
1.95	1.33	35.2	8.21	91.4	5.58	62.1
2.04	1.39	29.5	7.38	69.8	5.02	47.5
3.29	2.24	17.6	4.81	28.9	3.27	19.6
4.30	2.92	12.2	---	---	---	---
4.60	3.13	11.0	3.04	11.9	2.07	8.09
2.93	1.99	26.2	4.73	29.8	3.22	20.2
2.80	1.91	25.4	4.76	30.3	3.24	20.6
2.74	1.87	26.6	5.15	35.4	3.50	24.0
2.74	1.87	28.7	5.23	37.1	3.56	25.2
3.08	2.09	24.1	4.70	29.2	3.20	19.9
3.23	2.20	23.4	4.59	27.7	3.12	18.8
5.15	3.50	12.0	2.79	9.63	1.89	6.55
4.39	2.99	17.8	3.25	13.5	2.21	9.16
4.36	2.96	15.9	3.41	14.4	2.32	9.76
4.30	2.92	16.6	3.45	14.7	2.34	10.0
4.54	3.09	15.7	3.21	13.1	2.18	8.93
5.24	3.57	12.1	2.80	9.63	1.90	6.55
4.11	2.80	15.3	3.58	15.8	2.43	10.7

Notes:

- Charges were suspended at mid-depth in m of water 21.34m
- TNT loading density ≈ 1.61 (g/cc)
- Gauges suspended at various depths
- Impulse and energy flux time of integration is 1.0ms

Table B.5 Attenuated Pressure Wave Data (USACE 1961)

USACE (1961) - Attenuated (Bubble Screen) Data

Depth, z = 2.743m
Charge Weight, W = 3.63kg

z_g	R	$R/W^{1/3}$	T	A_c	A_f	P_{fw}	U_{fw}	P_r	U_r
m	m	$m/kg^{1/3}$	m	$m^3/s/m^2$	$m^3/s/m$	MPa	$kPa\text{-}m/kN^{1/3}$	MPa	$kPa\text{-}m/kN^{1/3}$
2.74	1.83	1.19	0.914	4.27E-04	3.90E-04	24.8	107	24.1	105.4
2.74	1.83	1.19	0.914	1.34E-03	1.23E-03	24.8	107	20.0	80.9
2.74	1.83	1.19	0.914	1.07E-02	9.75E-03	24.8	107	7.58	23.4
2.74	3.66	2.38	0.914	4.27E-04	3.90E-04	14.5	45.8	13.1	36.2
2.74	3.66	2.38	0.914	1.34E-03	1.23E-03	14.5	45.8	7.58	21.3
2.74	3.66	2.38	0.914	1.07E-02	9.75E-03	14.5	45.8	2.69	7.56
1.37	2.29	1.49	0.914	4.27E-04	3.90E-04	22.8	128	19.3	78.8
1.37	2.29	1.49	0.914	1.34E-03	1.23E-03	22.8	128	15.2	59.6
1.37	2.29	1.49	0.914	1.07E-02	9.75E-03	22.8	128	4.69	8.73
1.37	3.91	2.54	0.914	4.27E-04	3.90E-04	13.8	44.7	15.2	38.3
1.37	3.91	2.54	0.914	1.34E-03	1.23E-03	13.8	44.7	4.90	12.8
1.37	3.91	2.54	0.914	1.07E-02	9.75E-03	13.8	44.7	1.93	2.13
0.08	3.23	2.10	0.914	4.27E-04	3.90E-04	19.3	40.5	16.5	20.2
0.08	3.23	2.10	0.914	1.34E-03	1.23E-03	19.3	40.5	6.90	6.92
0.08	4.53	2.95	0.914	4.27E-04	3.90E-04	13.8	11.7	4.00	4.37
0.08	4.53	2.95	0.914	1.34E-03	1.23E-03	13.8	11.7	2.90	2.13
0.08	4.53	2.95	0.914	1.07E-02	9.75E-03	13.8	11.7	0.407	0.107
2.74	1.83	1.19	0.457	8.53E-04	3.90E-04	31.7	202	33.8	149
2.74	1.83	1.19	0.457	1.34E-03	6.13E-04	31.7	202	33.1	170.4
2.74	1.83	1.19	0.457	1.07E-02	4.88E-03	31.7	202	14.5	65.0
2.74	1.83	1.19	0.457	2.10E-02	9.62E-03	31.7	202	6.21	34.1
2.74	3.66	2.38	0.457	8.53E-04	3.90E-04	17.2	65.0	16.5	37.3
2.74	3.66	2.38	0.457	1.34E-03	6.13E-04	17.2	65.0	17.2	42.6
2.74	3.66	2.38	0.457	1.07E-02	4.88E-03	17.2	65.0	4.41	14.9
2.74	3.66	2.38	0.457	2.10E-02	9.62E-03	15.9	49.0	6.76	16.0
0.08	3.23	2.10	0.457	8.53E-04	3.90E-04	19.3	40.5	17.9	28.8
0.08	3.23	2.10	0.457	1.34E-03	6.13E-04	19.3	40.5	6.00	4.26
0.08	3.23	2.10	0.457	1.07E-02	4.88E-03	19.3	40.5	2.21	0.746
2.74	1.83	1.19	0.152	2.53E-03	3.86E-04	33.1	234	31.7	213.0
2.74	1.83	1.19	0.152	1.07E-02	1.63E-03	33.1	234	26.2	149.1
2.74	1.83	1.19	0.152	2.13E-02	3.25E-03	33.1	234	22.8	117.2
2.74	1.83	1.19	0.152	4.27E-02	6.50E-03	33.1	234	16.5	72.4

z_g = gauge depth, R = radial standoff distance, T = thickness, A_c = air content, A_f = air flow, P_{fw} = peak pressure (free-water), U_{fw} = energy flux (free-water), P_r = peak pressure (attenuated), U_r = energy flux (attenuated)

Bibliography

American Institute of Steel Construction. (2011). *Steel Construction Manual*, 14th Ed., American Institute of Steel Construction, Chicago.

American Institute of Steel Construction. (2010). *Specification for Structural Steel Buildings,* American Institute of Steel Construction, Chicago.

Beers, F. P., Johnston Jr, E. R., DeWolf, J. T., Mazurek, D. F. (2009). *Mechanics of Materials*, 5th Ed., McGraw-Hill, New York.

Biggs, J. M. (1964). *Introduction to Structural Dynamics*, McGraw-Hill, New York.

Bischoff, P. H., and Perry, S. H. (1991). "Compressive Behaviour of Concrete at High Strain Rates." *Materials and Structures*, 24, 425-450.

CALTRAN. (2009) *Technical Guidance for Assessment and Mitigation of the Hydroacoustic Effects of Pile Driving on Fish*, California Department of Transportation, Sacramento, California.

Chapman, N. R. (1985). "Measurement of the Waveform Parameters of Shallow Explosive Charges." *Journal of the Acoustical Society of America*, 78(2), 672-681.

Cole, R. H. (1948). *Underwater Explosions*, Princeton University Press, Princeton, New Jersey.

Coles, J. S., Christian, E. A., Slifko, J. P., Niffenegger, C. R., and Rogers M. A. (1946). *Shock-Wave Parameters from Spherical TNT Charges Detonated Underwater*. Underwater Explosives Research Lab., Woods Hole Oceanographic Institute, Massachusetts.

Cooper, P. W. (1996). *Engineering Explosives*, VCH Publishers, New York.

Cormie, D., Mays, M., and Smith, P. (2009) *Blast Effects of Buildings,* 2nd Ed., Thomas Telford Ltd., London.

Ditmars, J. D., and Cederwall, K. (1974). "Analysis of Bubble Plumes." *Coastal Engineering*, 2209-2226.

Domenico, S. N. (1982a). "Acoustic Wave Propagation in Air-Bubble Curtains in Water –Part I: History and Theory." *Geophysics*, 47(3), 345-353.

Domenico, S. N. (1982b). "Acoustic Wave Propagation in Air-Bubble Curtains in Water – Part II: Field Experiment." *Geophysics*, 47(3), 354-375.

Dowding, C. H. (1985). *Blast Vibration Monitoring and Control*, Prentice-Hall, New York.

Fessenden, R. A. (1920). (To Submarine Signal Company). "Method and Apparatus for Sound Insulation," U.S. Patent 1,348,828, August 3, 1920.

Gibson, F. W. (1970). “Measurement of the Effect of Air Bubbles on the Speed of Sound in Water.” *The Journal of the Acoustical Society of America*, 48(2), 1195-1197.

Grant, F. S., and West, G. F. (1965). *Interpretation Theory in Applied Geophysics*, McGraw-Hill, New York.

Grogan, A. (2005). “Design and Testing of a Bubble Curtain at Whirl Bay, B.C.” *Proceedings of the Thirty-first Annual Conference on Explosives and Blasting Technique*, Orlando, FL, International Society of Explosive Engineers, Cleveland, OH, Vol. 1, 113-124.

Heathcote, T. B. (1981). *An Experimental Program to Determine the Environmental Impact of Explosive Removal of Oil Wellheads*. Progress Report, Naval Surface Weapons Center, White Oak Lab., Silver Spring, Maryland.

Hempen, G. L. (1993a). “Reducing Underwater Blast damage with Air-Screens.” *Proceedings, Nineteenth Annual Conference of Explosives and Blasting Technique*, Austin, TX, International Society of Explosives Engineers, Cleveland, OH, 337-346.

Hempen, G. L. (1993b). *Air-Screen Reduction of Water-Borne Energy from Underwater Blasting*, PhD Dissertation, University of Missouri-Rolla, Department of Geological Engineering, Rolla, Missouri.

Keevin, T. M., and Hempen, G. L. (1997). *The Environmental Effects of Underwater Explosions with Methods to Mitigate Impacts*, U.S. Army Corps of Engineers, St. Louis, Missouri.

Kinsler, L. E., and Frey, A. R. (1950). *Fundamentals of Acoustics*, Wiley & Sons, New York.

Langefors, U., and Kihlstrom, B. (1978). *The Modern Technique of Rock Blasting*, 3rd Ed., Halsted Press, New York.

Lee, J., and Rude, G. (2007). *Performance Evaluation of the Roach Cove Bubble Screen Apparatus*, Defence R&D Canada – Suffield, Medicine Hat, Alberta, Canada.

Locking, P. M. (2011). “The Trouble with TNT Equivalence.” *26th International Symposium on Ballistics*, International Ballistics Society, Paper 11770, 1-25.

Misovec, A. P. (1976). *Explosion Phenomena*, David W. Taylor Naval Ship R&D Center, Bethesda, Maryland.

Mohorovic, C., Harris, D. W., and Dolen, T. P. (1999). *Dynamic Properties of Mass Concrete Obtained from Dam Cores, DSO-98-15*, Bureau of Reclamation, U.S. Department of Interior, Washington, DC.

Richmond, D. R. (1973). *Far-Field Underwater Blast Injuries Produced by Small Charges*, Lovelace Foundation for Medical Education and Research, Albuquerque, New Mexico.

Swisdak Jr., M. M. (1978). *Explosion Effects and Properties: Part II – Explosion Effects in Water*, Naval Surface Weapons Center, White Oak Lab., Silver Spring, Maryland.

Sulfredge, D. C., Morris, R. H., and Sanders, R. L. (2005). *Calculating the Effect of Surface or Underwater Explosions on Submerged Equipment and Structures*, Oak Ridge National Laboratory, Oak Ridge, Tennessee.

USACE. (1961). *Shock-Wave Attenuation Properties of a Bubble Screen*, U.S. Army Engineer Waterways Experiment Station, Vicksburg, Mississippi.

USACE. (1991). *Underwater Blast Monitoring*, U.S. Army Corps of Engineers, Washington, DC.

Wright, D. G., and Hopky, G. E. (1998). *Guidelines for the Use of Explosives In or Near Canadian Fisheries Waters*. Canadian Technical Report of Fisheries and Aquatic Sciences 2107. Minister of Public Works and Government Services Canada. Ottawa, Ontario, Canada.

VITA

Paul Raymond Smith was born in Athens, Georgia. He attended Asbury College (now Asbury University) where he received a Bachelor's of Arts degree in Engineering Mathematics. He then attended the University of Kentucky where he received a Bachelor's of Science degree in Civil Engineering. Paul worked at Mason and Hanger, Inc. in Lexington, Kentucky as a structural engineer, and later moved to Kampala, Uganda to work with Engineering Ministries International as a structural engineering intern. In the year before beginning graduate studies, Paul taught engineering related high school classes at the Jessamine County Career and Technical Center, in Nicholasville, KY. At Asbury College, Paul received the Presidential Scholarship and graduated Cum Laude. In his undergraduate studies at the University of Kentucky, he received the Michael C. Garver Scholarship and again graduated Cum Laude. During his graduate studies at the University of Kentucky, Paul received a Deep Foundations Institute Educational Trust At-Large Scholarship and the ADSC Ohio Valley Chapter Thomas Buzek Scholarship.